Ablation of gold irradiated by femtosecond laser pulse: Experiment and modeling

S I Ashitkov[1], P S Komarov[1], V V Zhakhovsky[2,3,1], Yu V Petrov[3], V A Khokhlov[3], A A Yurkevich[1], D K Ilnitsky[2,3], N A Inogamov[3] and M B Agranat[1]

[1] Joint Institute for High Temperatures of the Russian Academy of Sciences, Izhorskaya 13 Bldg 2, Moscow 125412, Russia
[2] Dukhov Research Institute of Automatics (VNIIA), Sushchevskaya 22, Moscow 127055, Russia
[3] Landau Institute for Theoretical Physics of the Russian Academy of Scienses, Akademika Semenova 1a, Chernogolovka, Moscow Region 142432, Russia

E-mail: ashitkov11@yandex.ru

Abstract. We report on the ablation phenomena in gold sample irradiated by femtosecond laser pulses of moderate intensity. Dynamics of optical constants and expansion of a heated surface layer was investigated in a range from picosecond up to subnanosecond using ultrafast interferometry. Also morphology of the ablation craters and value of an ablation threshold (for absorbed fluence) were measured. The experimental data are compared with simulations of mass flows obtained by two-temperature hydrodynamics and molecular dynamics methods. Simulation shows evolution of a thin surface layer pressurized by a laser pulse. Unloading of the pressurized layer proceeds together with electron-ion thermalization, melting, cavitation and spallation of a part of surface liquid layer. The experimental and simulation results on two-temperature physics and on a fracture, surface morphology and strength of liquid gold at a strain rate $\sim 10^9$ s^{-1} are discussed.

1. Introduction

The ultrashort laser–matter interaction with a pulse duration of the order $\sim 10^{-13}$ s and incident fluence ~ 1 J/cm^2 is important for studying fundamental physics of ultrafast non-equilibrium processes and nanoscale phenomena in condensed matter. These processes begin with absorption of light and with a two-temperature (2T) stage [1,2]. Two-temperature approximately isochoric heating of metal target by femtosecond laser pulse (FLP) later in time results in formation of a thermo-mechanically stressed state [3–5]. Unloading of this state may cause frontal cavitation and ablation of subsurface molten layer if tensile stress overcomes material strength (the frontal side is the irradiated boundary of a target). The subsequent process of surface nano-structuring is composed from a sequence of processes starting from void nucleation in a stretched melt, which is followed by rapid cavitation and expansion of foam-like melt, breaking of foam, and subsequent conductive recrystallization of surface and freezing of foam remnants keeping its conductive links to a surface [6–10]. Recrystallization of remnants *losing* their conductive contact with a bulk region of a target is a much slower process in comparison with recrystallization a remnants

remaining in mechanical and thermal connection with a target. Freezing of the separated droplets proceeds thanks to the radiative loses from surface of the droplets [11, 12].

Duration of a laser pulse $\tau_L \sim 10^{-13}$ s is much less than electron-ion equilibration time $\tau_{ei} \sim$ 1–10 ps. Therefore absorption of laser energy by electrons causes transition of metal into non-equilibrium 2T state. At moderate incident intensities $\sim 10^{12}$–10^{13} W/cm^2 the electron temperature T_e may be 1–2 orders of magnitude above ion temperatures T_i and exceeds $T_e > 10^4$ K [13, 14]. Time of equilibration τ_{ei} depends on type of metal.

For metals with a fast electron-phonon relaxation, such as Al, Fe, Ni et al., at moderate laser intensity the hydrodynamic time scale $t_s = d_T/c =$ 20–30 ps is greater than the time scale for heating of a lattice $\tau_{ei} =$ 1–2 ps through the electron-phonon energy exchange; here d_T is thickness of the heated surface layer of a bulk target, c is a speed of sound. For these metals the 2T and the hydrodynamic stages have different time scales and therefore can be considered relatively independent from each other. But if electron-ion heating of a lattice is slow (as, for example, in the case of noble metals Au or Ag), then the hydrodynamic expansion begins already during 2T stage [15] and it is impossible clearly separate the 2T heating stage and the hydrodynamic stage. Below we consider gold, metal with the slowest electron-ion energy exchange. Thus theoretical description given below includes full 2T physics:

(i) *Absorption of a pump pulse.* Absorption coefficient $A = 1 - R$ changes during a pump pulse for our level of intensities and pulse durations, i.e., we are in the regime of non-linear absorption $F_{\rm abs} = A(F_{\rm inc})F_{\rm inc}$, here R is reflection coefficient, while $A(F_{\rm inc})$ is a value averaged along a pulse. Therefore a refraction index for room temperature gold can not be used for calculation of absorption [16, 17]; for room temperature gold the linear coefficient A changes from 0.8% to 4.7% in the photon energy interval $1 < E < 2$ eV [18] for normal incidence. In the non-linear regime $I_{\rm abs}(t) = A(t)\, I_{\rm inc}(t)$ absorption $A(t')$ depends on behavior of intensity $I_{\rm inc}(t)$ at previous stages $t < t'$. Durations of pump pulses used in experiments presented below are $\tau_L =$ 40–100 fs. They are very short in comparison with the time scales τ_{ei} and t_s. Therefore variation of absorption $A(t)$ during a pulse is of small importance, we use a value $A(F_{\rm inc})$ averaged along a pulse. For our calculations the value of integral energy $F_{\rm abs}$ absorbed during a pulse is necessary. It is experimentally measured in our experiments: $A \approx 13\%$ for the near ablation threshold fluences for wavelength $\lambda = 620$ nm.

(ii) *2T electron-ion relaxation, thermal and dynamics effects.* The first paper [1] where the 2T model has been introduced includes two thermal equations. Up to now the model with a pair of electron and ion energy equations is in wide use. It is simple and valid for fluences below ablation threshold when expansion dynamics is rather insignificant. 2T hydrodynamics code is used below. It combines thermal equations from [1] with dynamic ones. This allow us to consider the active hydrodynamic cases above an ablation threshold and for a long time interval covering a nucleation stage. Wide-range equation of state [19, 20] with 2T additions [21–23] is employed in simulations. The model describes (*) melting of gold in 2T state [13] and (*) transition from 2T to 1T states. Below it is shown experimentally and theoretically how the vacuum boundary of gold decelerates due to material resistance to stretching. Above ablation threshold the stretching overcomes material strength, then nucleation develops and spallation of a surface layer takes place.

Below experimental data are presented first. After that theoretical explanations are given. Experimental data are obtained thanks to ultrafast pump-probe technique measuring evolution of optical properties of a target irradiated by pump. This is complicated field of research. Up to now there are inaccuracies in measuring of dielectric permittivity even for room temperature gold [18]. Obviously it is more difficult to obtain optical information for liquid gold. Molten gold not far from melting temperature has $\epsilon(\lambda = 620\,{\rm nm}) = -10 + 6{\rm i}$ according to [24] while

$\epsilon(\lambda = 633\,\mathrm{nm}) = -9.6 + 8.2\mathrm{i}$ according to [25]. For longer wavelength the data for liquid phase are: $\epsilon(\lambda = 1064\,\mathrm{nm}) = -35 + 14.3\mathrm{i}$ [25] and $\epsilon(\lambda = 1060\,\mathrm{nm}) = -43 + 19\mathrm{i}$ [26]. Much more complicated is the situation with 2T gold. Scientists equipped with the most recent technique attack the problem of the 2T warm dense gold. Mainly pump-probe measurements following evolution of current values of a dielectric function [13, 27–36] are used to shed light upon 2T physics. In papers [29–31, 33–36] pump-probe frequency domain interferometer technique is used. In paper [37] pump-probe x-ray absorption near-edge structure (XANES) method has been used to define electron temperature in Cu after fs heating, see simulation of this experiment in paper [38]. Ultrashort x-ray probe has been used for probing of the x-ray absorption near a spectral edge [37].

In important other works the ultrashort x-ray or electron beam pulse serves for x-ray [39, 40] or electron diffraction [41]. People study melting by fs pulse. In this case a device with short probe delay time (few ps) is employed. In other experiments the acoustic oscillations of nanofilms or nanoparticles is studied. Then longer delays (tens or hundreds ps) between pump and probe are used. Probe may be optical, x-ray, or electron ultrashort pulse.

In paper below experimental pump-probe observations and physical model are presented. They cover the short 2T stage and the long stage of hydrodynamic expansion both.

2. Experiment

The investigations are performed using femtosecond interferometric microscopy [42] with Fourier processing of interference patterns. This pump-probe technique makes it possible to detect the dynamics of amplitude and phase changes of a probe wave reflected from the interaction area with high temporal and spatial resolution.

The sample was a gold film 0.5 μm thick thermally deposited onto polished glass substrate. The targets were mounted at computer controlled three-axis translation stage. After each pump shot the target was moved to a new area.

The source of radiation was the high power femtosecond Cr:F laser system [43]. The p-polarized pump pulse with duration 80 fs at a wavelength $\lambda_1 = 1240$ nm was focused onto the sample at an angle of incidence of 45 degree. The spatial distribution of pump radiation in a focal spot was Gaussian with a radius of 25 μm at a level e^{-1}. The probe pulse at a second harmonic wavelength $\lambda_2 = 620$ nm with the duration of 80 fs illuminated the target surface at a normal incidence with a varying time delay. For experimental study of optical properties of the excited area of a target the Michelson interferometer with imagine configuration was used. The image of target surface was transferred to the matrix of a CCD camera by means of a micro-objective with a numerical aperture of NA = 0.2;. The probe object beam reflected from the sample interfered with the reference beam and formed interference fringes in the matrix of CCD camera. The algorithm of 2D Fourier processing of interference patterns was described previously in [44]. The accuracy of the measurements of amplitude and phase was better than 1% and $\pi/200$ correspondingly. The temporal resolution was of the order of $\sim 10^{-13}$ s.

The ablation threshold on incident fluence F_a determined from the dependence of the lateral dimension of crater from the energy of FLP [45] was equal to 1.3 J/cm^2. The measured reflection coefficient of the pump near the ablation threshold was approximately 0.92. So the absorbed laser fluence of the pump pulse near threshold F_a in this case was equal to $F_a^{\mathrm{abs}} = (1 - R)F_a \approx 0.1$ J/cm^2.

Figure 1 shows the cross section of the ablation crater obtained from the interferometric measurements for $F/F_a \approx 1.2$.

Figure 2 shows the temporal dependences of the normalized reflectivity $R_N(t) = R(t)/R(t = -\infty)$ and phase difference $\Delta\varphi(t) = \varphi(t) - \varphi(t = -\infty)$ for laser fluence F/F_a=1.2 in the temporal range 0–20 ps. Here transient normalized reflectivity on intensity is defined as $R_N(t) = |r_N(t)|^2$, where $|r_N|$ is normalized reflectivity on electromagnetic wave amplitude. Both dependences

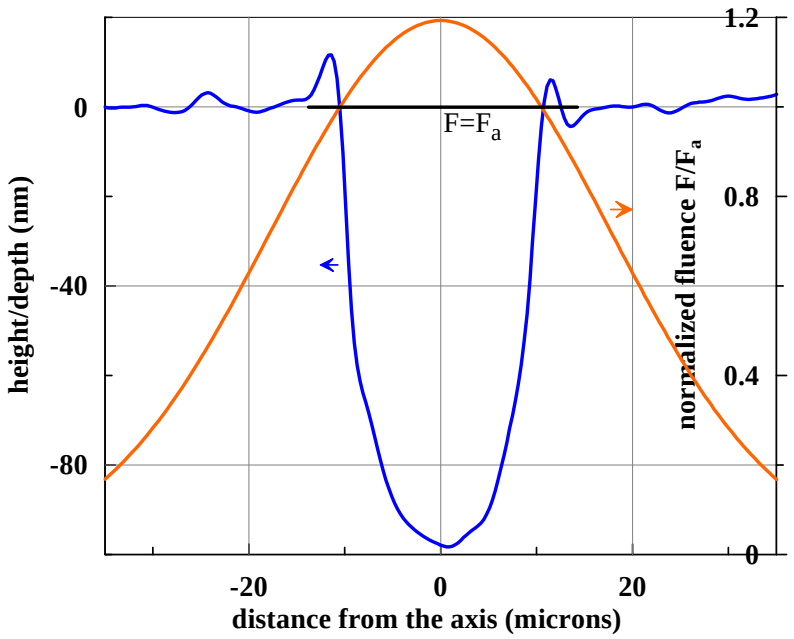

Figure 1. Profile of the ablation crater on the gold target at $F_0/F_a \approx 1.2$ (blue curve, left axis) and the normalized distribution of fluence across a focal spot (red curve, right axis) are shown. The horizontal straight line emphasizes the threshold value of fluence.

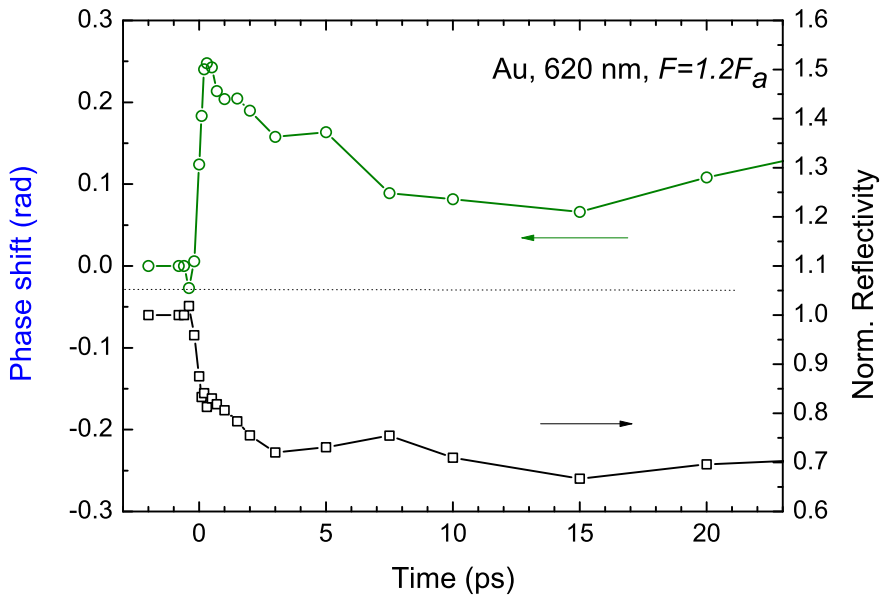

Figure 2. The temporal dependences of normalized reflectivity (black curve) and phase changes (green curve) of the reflected probe wave at 620 nm for laser fluence F/F_a=1.2.

exhibit fast jump of R_N and $\Delta\varphi$ on a subpicosecond scale. Next, we see a relatively slow change within 10 to 15 ps. This behavior R_N and $\Delta\varphi$ obviously linked to the relaxation of T_e and

T_i at two-temperature (2T) stage. Let us draw attention to presence of the plateaus on these dependences in the range from about 3 to 6 ps after laser heating. As it can be seen from the calculations below, this feature may be due to melting of gold lattice. The subsequent growth $\Delta\varphi$ after 15 ps is obviously connected with the beginning of hydrodynamic motion of the sample surface. The dynamics of ablation process in the range of 20–500 ps will be described below.

Let us now consider the behavior of optical constants during 2T stage using complex reflectivity dynamics shown in figure 2. Whereas the amplitude depends only on a complex refractive index, the phase depends on a complex refractive index and also on surface displacement z. We will consider now temporal range 0.2–10 ps. Temperature profiles $T_e(x)$ and $T_i(x)$ within this range vary slightly at a scale of penetration depth of a probe pulse (~ 10 nm) and the boundary of target is sharp (see sections below). So we can apply Fresnel equations in the form:

$$r\mathrm{e}^{\mathrm{i}\varphi} = \left(\frac{1-\tilde{n}}{1+\tilde{n}}\right) \tag{1}$$

to calculate complex refractive index $\tilde{n} = n + \mathrm{i}k$. For unexcited gold at the probe wavelength 620 nm corresponding values are $n_0 = 0.2101$ and $k_0 = 3.126$ [46].

Figure 3 represents the behavior of the real ε_1 and imaginary ε_2 parts of complex dielectric function, which are connected with optical constants as:

$$\varepsilon_1 = n^2 - k^2; \quad \varepsilon_2 = 2nk. \tag{2}$$

The real and imaginary parts of permittivity of an unexcited gold before exposure at 620 nm, calculated according to the expressions (2), are equal to $\varepsilon_1^0 = -9.73$ and $\varepsilon_2^0 = 1.31$. Thick lines in figure 3 show the values of dielectric permittivity of liquid gold $\varepsilon_1^{\mathrm{liq}} = -9.58$ and $\varepsilon_2^{\mathrm{liq}} = 8.2$, obtained in [25] for stationary conditions at wavelength of 633 nm for the temperature 1.4 kK.

At the beginning of two-temperature stage at 0.3 ps delay after the pump laser exposure the complex dielectric permittivity changes abruptly to its maximal transient value $\varepsilon = \varepsilon_1 + \mathrm{i}\varepsilon_2 \approx -19 + 17\mathrm{i}$. Further, after 8–10 ps the transient permittivity $\varepsilon(t)$ smoothly approaches the stationary value of liquid gold. Small deviations at the right side in figure 3 are due to a beginning of the hydrodynamic motion, which affects on the phase of the reflected probe wave.

Figure 4 represents the dynamics of surface expansion in the range 15–500 ps.

The surface displacement (points) was calculated directly from the phase shift measured in experiment using expression:

$$z = \Delta\varphi\, \lambda_2/4\pi, \tag{3}$$

where λ_2 is wavelength of a probe wave. The surface velocity profile $u(t)$ was obtained via differentiation of the smoothed displacement profile $z(t)$.

Velocity $u(t)$ sharply increases during two-temperature stage and achieves its maximum value 0.34 km/s. After that due to resistance of condensed matter to stretching the dependence $u(t)$ decreases and nucleation starts in stretched molten gold with subsequent removal of a part of melt in the form of thin liquid plate (thermomechanical ablation). The tensile strength value of liquid gold σ can be roughly estimated using the acoustic relation [7, 47]:

$$\sigma = \rho c \Delta u/2. \tag{4}$$

For the experimentally determined value $\Delta u = 0.28 \pm 0.3$ km/s (see figure 4) and taking for liquid gold density and sound velocity $\rho \approx 16$ g/cm^3, $c \approx 2.3$ km/s [19–23], we obtain an estimate $\sigma \approx 5 \pm 1$ GPa at the strain rate of $\sim 10^9$ s^{-1}.

These tensile stresses initiate the nucleation of vapor bubbles in the molten gold. The growth and consolidation of the cavitation bubbles creates a foaming melt. After several tens or hundreds picoseconds inside the surface layer forms a thin liquid ablative plate, separated from the main material of target by foamed melt [10]. The observed on figure 4 deceleration of the ablation layer in the range of 100–500 ps is obviously caused by resistance of foam to stretching.

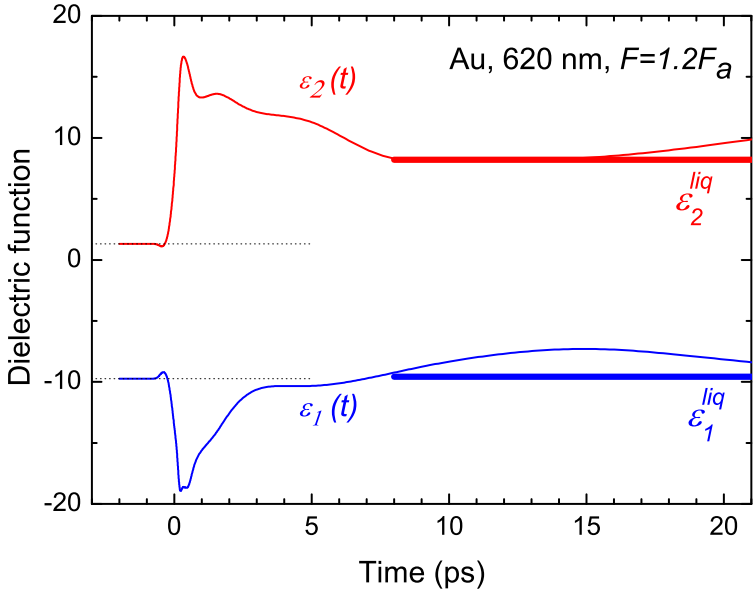

Figure 3. Temporal evolution of the real (thin blue line) and imaginary (thin red line) parts of dielectric function. Thick lines—the value of dielectric function of liquid gold at stationary conditions [25].

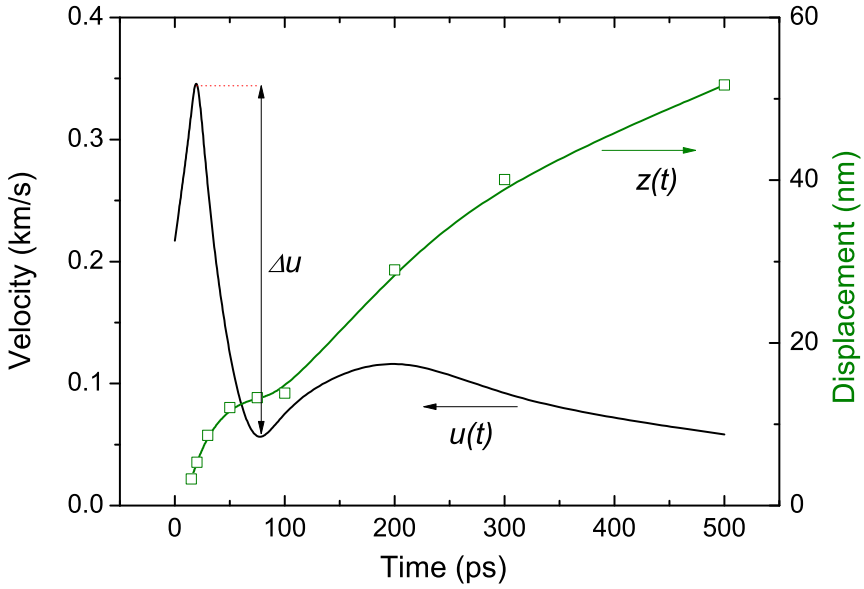

Figure 4. Displacement (green) and velocity (black) histories of gold surface movement at normalized laser fluence $F/F_a \approx 1.2$.

3. Theory and modeling

Computer simulations of ablation of gold by FLP was considered in papers [4, 15]. Here we consider frontal ablation of a bulk targets because thickness of a film $d_f = 500$ nm used in the presented above experiments is significantly larger than thickness $d_T \approx 100 - 150$ nm of a heat affected layer in bulk gold. General picture is well understood. There is a thermomechanical ablation threshold F_a. If absorbed fluence $F^{\rm abs}$ overcomes the threshold $F_a^{\rm abs}$ then a crater appears and a piece of a surface layer (spallation plate) runs away. This is a general picture. But interesting details remains unknown. Here we discuss (i) the initial stage covering few first picoseconds, (ii) deceleration of a spallation shell at the late (subnanosecond) stages; at very late stage this is a result of deceleration by a foam stretching [6, 10]; foam covers space between a spallation plate and bottom of a future crater [6, 10], (iii) posibility to observe the spallation oscillations; these oscillations are well known for the larger spatial scales: submillimeter–centimeter range of thicknesses [47, 48], and (iv) strength of liquid gold as a function of temperature.

4. Thermodynamics and hydrodynamics of two-temperature stage

System of two-temperature (2T) hydrodynamics (2T-HD) equations was developed in papers [42, 49–54]. 2T-HD equations are

$$\rho(x^0,t)\frac{\partial x(x^0,t)}{\partial x^0} = \rho^0, \tag{5}$$

$$\rho^0\frac{\partial u}{\partial t} = -\frac{\partial P(x^0,t)}{\partial x^0}, \tag{6}$$

$$\frac{\partial x(x^0,t)}{\partial t} = u(x^0,t), \tag{7}$$

$$\rho^0\,\frac{\partial (E_e/\rho)}{\partial t} = -\frac{\partial q}{\partial x^0} - \dot{E}_{ei} + \frac{\rho^0}{\rho}\,Q - P_e\frac{\partial u}{\partial x^0}, \tag{8}$$

$$\dot{E}_{ei} = \frac{\rho^0}{\rho}\alpha(T_e - T_i), \quad q = -\frac{\rho\kappa}{\rho^0}\,\frac{\partial T_e}{\partial x^0}, \tag{9}$$

$$\rho^0\,\frac{\partial (E_i/\rho)}{\partial t} = \dot{E}_{ei} - P_i\frac{\partial u}{\partial x^0}, \tag{10}$$

$$Q = \frac{F_{\rm abs}}{\sqrt{\pi}\,\tau_L\,\delta}\exp\left(-\frac{t^2}{\tau_L^2}\right)\exp\left(-\frac{x}{\delta}\right)\theta(x). \tag{11}$$

We use 2T-HD and molecular dynamics (MD) codes to describe ablation. The system of the 2T equations used in 2T-HD code given above is taken in a form written in [23]. It consists of kinematics, dynamics, and two thermal equations. One of the thermal equations corresponds to an electron subsystem, while another—for an ion subsystem. Above equation (5) is mass conservation $\rho\,\partial x = \rho^0\,\partial x^0$, where $x(x^0,t)$ is trajectory of a Lagrangian particle with Lagrangian coordinate x^0, $x(x^0, t = -\infty) = x^0$, ρ^0 is initial density; (6) is a momentum equation, $u(x^0,t)$ is velocity of Lagrangian particle; (7) is a kinematic condition; (8) is an energy balance for electron subsystem [1, 55]; definitions of electron-ion energy exchange power and electron heat conduction flux are given in (9); (10) is an energy balance for ion subsystem [1, 55]; (11) is a laser power source per unit volume in a skin layer δ, and τ_L is duration of a pulse.

Data concerning 2T-equation-of-state $E(\rho, T_e, T_i)$, $p(\rho, T_e, T_i)$, electron-ion (e-i) coupling parameter $\alpha(\rho, T_e)$, and electron heat conduction $\kappa(\rho, T_e, T_i)$ are necessary to integrate the 2T system. They are presented in appendices A, B, and C below. To compare with experimental results, a model of dielectric permittivity described in appendix D is used.

Solution of 2T-HD system for $F_{\rm abs} = 100$ mJ/cm^2, bulk target, and two different values of coupling parameter, see appendix B, are shown in figures. Figures 5 and 6 show evolution of

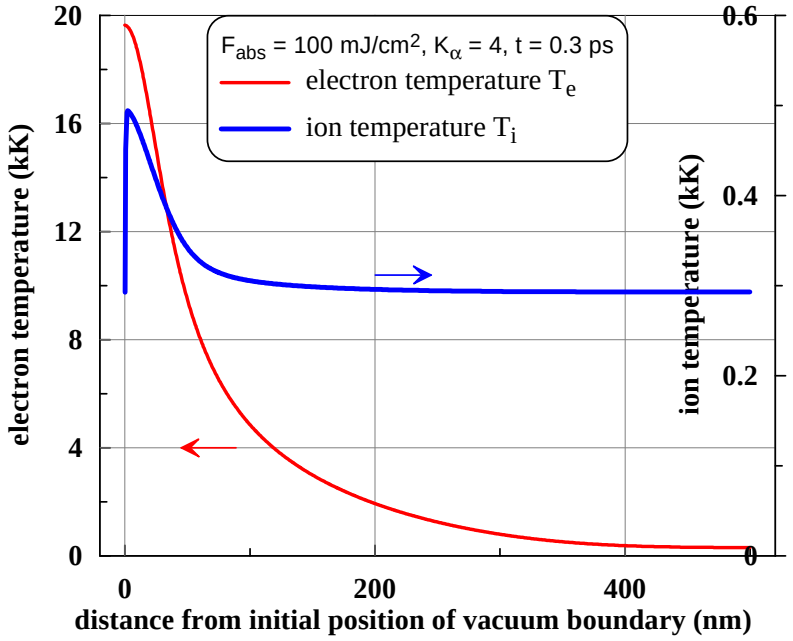

Figure 5. Instant electron and ion temperature profiles at the initial 2T stage. Far from a skin layer temperatures return to the room temperature value 0.3 kK. The case with slow electron-ion energy transfer $K_\alpha = 4$ (see appendix B) is shown.

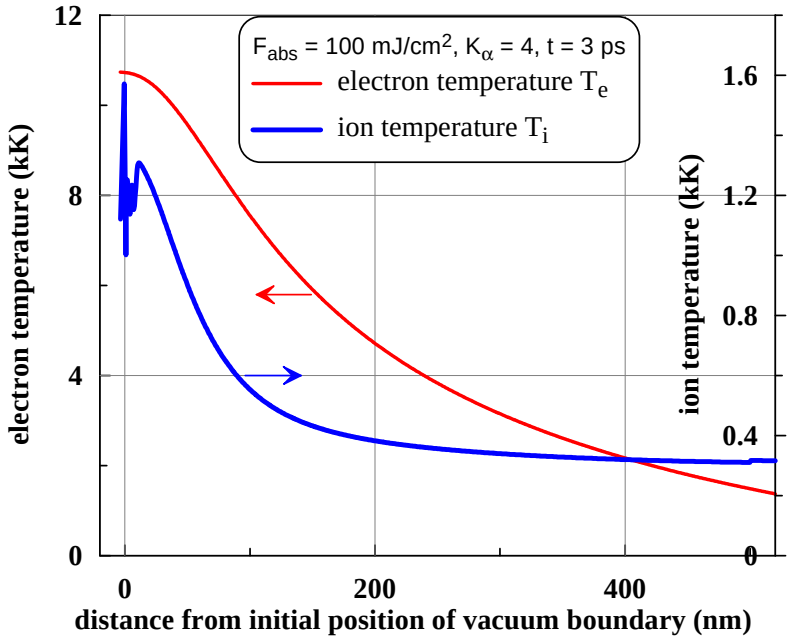

Figure 6. Decrease of T_e (comp. with figure 5) as a result of electron energy transport into bulk and e-i coupling and increase of T_i due to local e-i heating of ions by hot electrons. Lattice is close to melting near the left edge.

the spatial distributions of electron and ion temperatures for the case of slow e-i coupling. Gold is near beginning of melting at $t = 3$ ps for the decreased coupling α (appendix B) in figure 6.

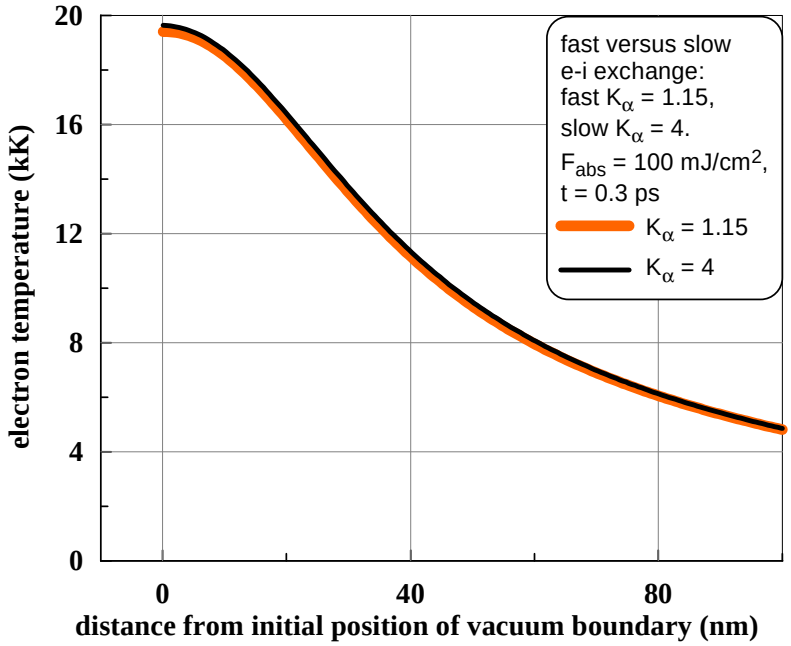

Figure 7. At an early stage an influence of coupling on electron temperature is negligible. While an influence on T_i is significant from early stage, see below.

In 2T-HD code we use equilibrium equation-of-state. In the spirit of separation of free energy of electron and ion subsystems (see appendix A), it is supposed that melting depends on only ion temperature and that melting curve is approximately the same as in the one-temperature (1T) case. Molecular dynamics (MD) is necessary to consider kinetics of melting. Comparison of melting in 2T-HD and MD has been studied in [13]. The conclusion from [13] was: 2T-HD melting and MD melting are quantitatively approximately similar.

Equation-of-state and conductivity are more or less established in the 2T physical model. But there are doubts concerning e-i coupling, see appendix B and papers cited therein; also see abstract in paper [35] where it was supposed that weaker coupling better explains measurements. Thus we run two cases with different α to estimate an influence of coupling. These two values of α are presented in appendix B.

Figures 7–10 help to understand a role of a coupling parameter α.

Analyzing figures 7 and 8 we see that electron heat conduction is more significant for cooling of electrons near surface than the e-i energy transfer; conduction transports electron internal energy through the electron subsystem from surface into bulk. Significance of conduction versus coupling is true for the bulk targets. In thin gold films (where thickness $d_f < d_T$ is small) the conduction is less significant for electron cooling than the e-i transfer. Therefore the rate of electron cooling is smaller. In thin gold films $d_f \approx d_T$ the two substages of electron cooling are distinguishable: the short first one is related to conductive homogenization of T_e across thickness of a film. The second longer substage is due to coupling. Its duration is defined by electron-ion temperature equilibration time.

Figures 9 and 10 illustrate importance of coupling α for heating and melting of lattice. There is a molten layer in figure 10 in the case with fast coupling, while in the case with slower ion heating a crystal still exists everywhere at the same instant $t = 3$ ps. Crystal is under significant pressure created not by compression but by fast (supersonic) heating. Pressure p increases melting temperature $T_m(p) > T_m(0) = 1337$ K. Pressure p is in the 15–20 GPa interval across the mixture zone at the time instant $t = 3$ ps shown in figure 11. At the instant $t = 3$ ps

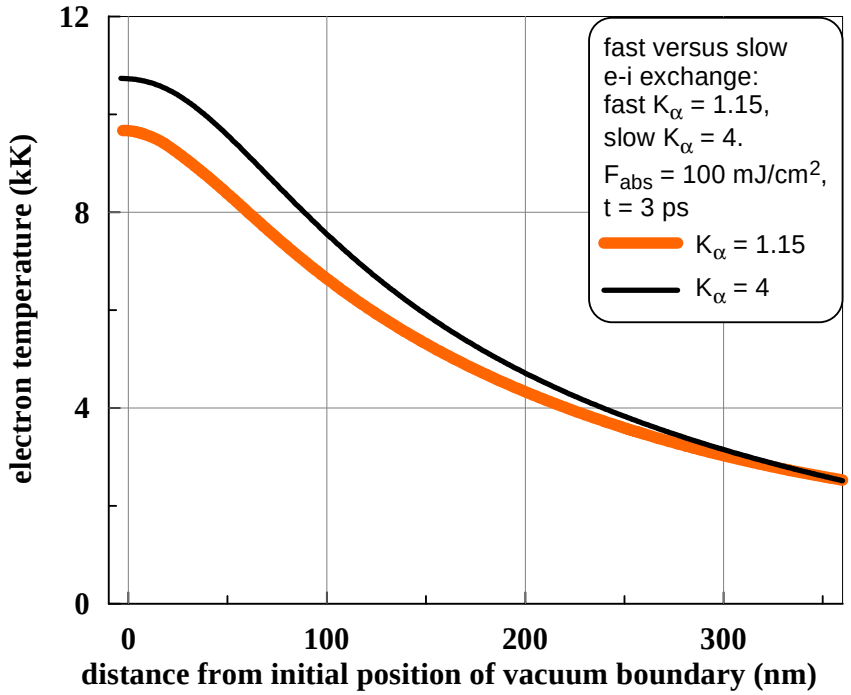

Figure 8. An influence of coupling on T_e becomes appreciable in the middle of a 2T stage.

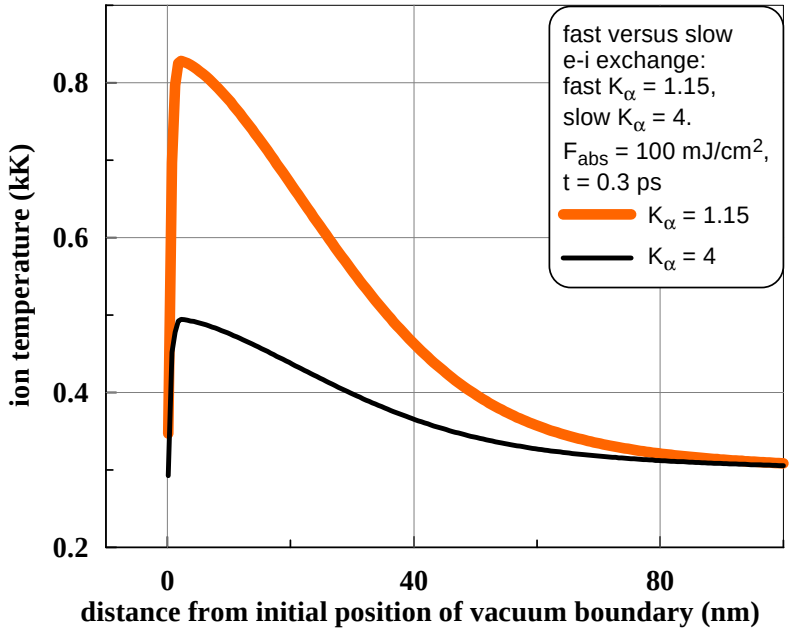

Figure 9. Increase of coupling is significant for ion temperatures–faster coupling increases T_i.

presented in figure 11 the sound wave c_s did not achieve the mixture zone. The wave c_s decreasing pressure is triggered by the pump laser pulse.

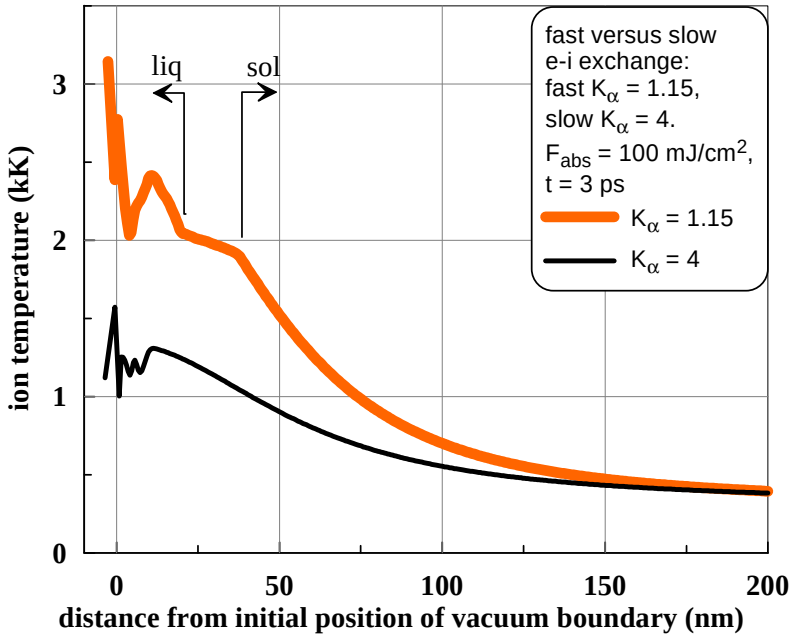

Figure 10. Gold near surface melts much earlier in the case with enhanced coupling parameter α. Arrows show molten and solid regions. The layer in between the arrows is filled with a two-phase mixture of crystal and liquid—comp. with process of melting described by MD simulation in [13]. In MD the mixture layer is wider.

5. Coupling and final ion temperatures and velocities

We see above (section 4) that value of a coupling parameter is very significant for ion heating. Electron conduction spreads absorbed heat during 2T stage in a wider surface layer in the case with a weaker coupling. Thus the heated layer d_T is thicker while ion temperature is smaller for weak coupling. This increases an ablation threshold (if, of course, all other parameters are fixed) and thickness of a spallation layer slightly above threshold. This thickness defines depth of a crater near ablation threshold, see figure 1. Decrease of ion temperature with decrease of coupling is clear in figure 12.

Positions of the solid–liquid separation planes and position of the sound wave are presented in figure 13. Mixture zone is located between the blue and red straights in this figure. Analyzing the ion temperature and pressure profiles for the two cases (weak versus strong coupling) we see that T_i and pressure are lower for weak coupling. Thus expansion velocity is smaller for smaller α. Propagation of the melting front is sharply decelerated at the end of the 2T stage.

Electrons faster cool down in the case with higher α. Therefore this case is more close to the end of the 2T stage, see figure 14. Electrons continue to heat ions (due to temperature difference T_e and T_i) at the instant shown in figure 14. But this additional heating of ions is small after the instant shown in figure 14. Indeed, at the electron temperatures shown the electrons return to the highly degenerate state thus strongly decreasing their heat capacity.

Thickness of the molten layer is smaller in the weak coupling case–compare positions of the blue/red straights in figure 13. By the time instant shown in figure 13 the rarefaction c_s runs ahead the melting layer in the weak coupling case, while for the strong coupling case the situation is opposite. Drop of pressure thanks to expansion decreases melting temperature $T_m(p)$. This helps to melt gold in the case with small α.

Absorbed energy $F_{\rm abs} = 100$ mJ/cm^2 is rather small. In this case the vacuum boundary of heated gold is very sharp, density drops down in an atomically thin transition layer between

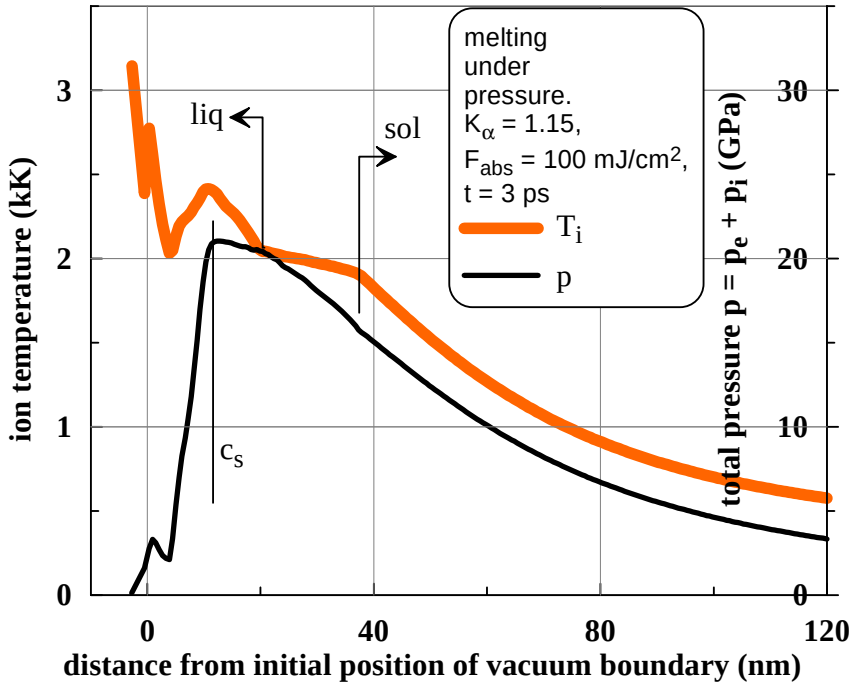

Figure 11. Pressure distribution across liquid gold, solid–liquid mixture layer and crystal is shown. Matter is under pressure therefore melting temperature is shifted up relative to the triple point. Position of a sound wave running from a vacuum boundary is shown by the vertical straight c_s.

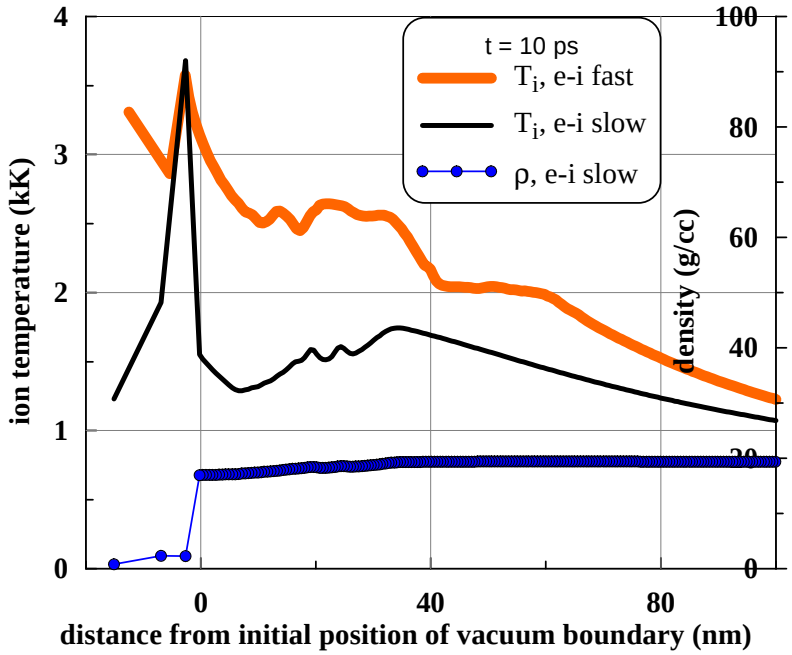

Figure 12. Slow increase of T_i and slow melting in the case with small α. The case with absorbed energy $F_{\rm abs} = 100$ mJ/cm^2 is shown.

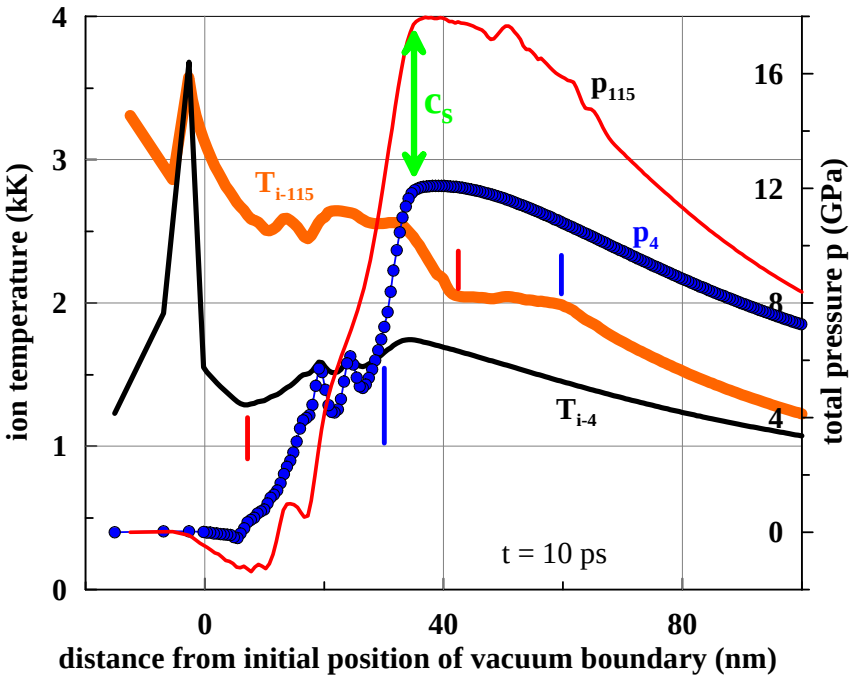

Figure 13. Relative positions of the melting and rarefaction fronts are shown for the cases with fast and slow coupling. The two blue vertical straights separate mixture from the left and solid from the right side. The two red straights separate molten gold from mixture. The green straight c_s is the head of the rarefaction wave triggered by a pump pulse. Speed of sound weakly depends on coupling and the time interval elapsed after a pump is relatively small. Therefore the positions c_s are almost the same for weak and strong coupling. Sharp drop of pressure begins behind the rarefaction front. Pressure is lower in the case of weak coupling because T_i is lower, while electron pressure decreases to small values near the end of the 2T stage. $F_{\text{abs}} = 100$ mJ/cm^2, $t = 10$ ps. This instant is near the end of the 2T stage. The indexes 115 and 4 correspond to $K_\alpha = 1.15$ (strong coupling) and $K_\alpha = 4$ (weak coupling) respectively.

vapor and condensed gold. Density profile with a jump is presented in figure 12. 2T-HD is Lagrangian code, see 2T system (5–11). A bulk gold target is divided into small spatial steps– this is our Lagrangian "particles". 2T-HD is a finite-difference code–to present smooth profiles small steps are necessary. There are numerical errors connected with finite-differences near the sharp jumps. These errors cause the nonphysical increase of T_i in the narrow vapor zone in figure 12. But this zone contains only the last two Lagrangian steps and thus may be neglected.

Again, the stronger coupling then the faster transfer of absorbed pump energy into ions, therefore thickness of a heated zone d_T is smaller, final (here this means after 2T stage) temperatures and pressures are larger, and consequently expansion velocities are larger at the same value of absorbed energy. Distributions of velocity are shown in figure 15. The vapor-liquid boundary (where the density jump is) expands with velocity given near the boundary at the right side of the jump. At the instant $t = 30$ ps presented in figure 15 these velocities equal ≈ 200 m/s.

6. Kinematics of a surface layer. Early stages

Process initiated by a pump pulse consists from several stages. For the bulk target these stages are:

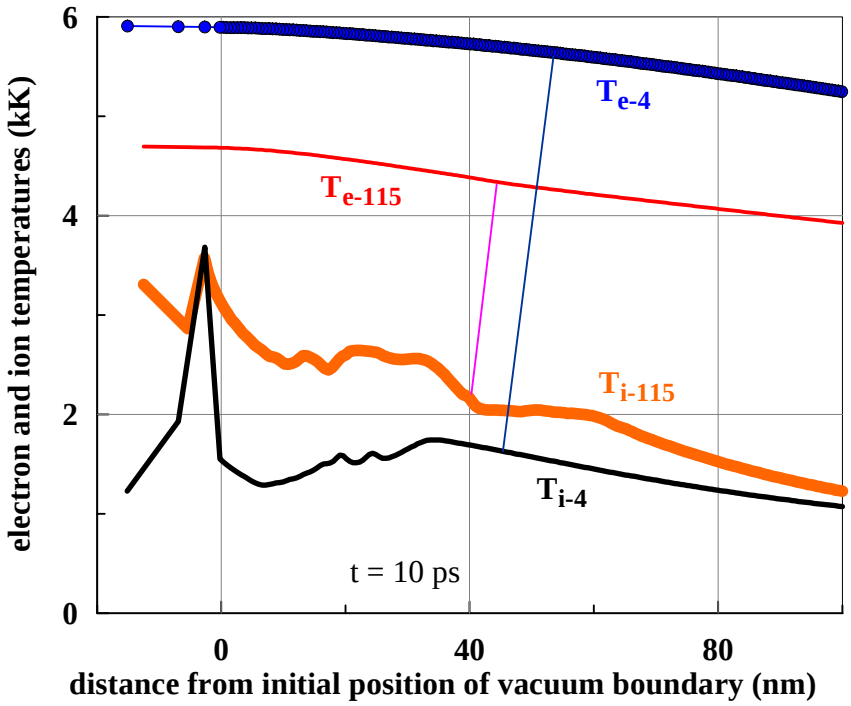

Figure 14. Electron and ion temperature profiles near the end of the 2T stage. For the case of strong coupling the T_e and T_i are more close to each other. Therefore gold will leave the 2T case earlier in the strong coupling case.

(i) Duration τ_L of an ultrashort pulse; we restrict ourself to $\tau_L \sim 0.1$ ps in intensity variation $\propto \exp(-t^2/\tau_L^2)$. Thus this is the shortest temporal scale in the hierarchy.

(ii) Cooling of a skin by a *high* electron 2T heat conduction κ of gold; this is the stage when electron pressure p_e and κ (taking away from a skin the electron internal energy E_e) dominate, while electron-ion coupling α is less significant. Taking-away of E_e by a fast thermal transport sharply decreases p_e. Cooling of electron subsystem by the α term (8) is weaker relative to the thermal transport at this particular stage. Also heating of ions by the α term (9) and corresponding thermal increase of ion pressure is smaller than *temporal* variation of electron pressure. Duration of thus stage depends on particular values of functions $\kappa(\rho, T_e, T_i)$ and $\alpha(\rho, T_e, T_i)$. But if the stage (ii) is marked out then it is shorter than the subsequent stage of electron-ion temperature relaxation.

(iii) The electron-ion temperature relaxation stage. Electron and ion temperatures equilibrate during this stage. An estimate of its duration (following from ion thermal equation (9)) is

$$t_{\rm eq} \sim \frac{c_i}{\alpha}\frac{T_i|_{\max}}{T_e|_{\max}} = \frac{25}{\alpha_1}\frac{T_i|_{\max}}{T_e|_{\max}}\ \text{ps}, \quad \alpha_1 = \alpha \times 10^{-17}\ \text{W}^{-1}\text{m}^3\text{K},$$

where $c_i = 3nk_B$, $n = 5.9 \times 10^{22}$ cm^{-3}. Here $T_i|_{\max}$ and $T_e|_{\max}$ are the maximum values. Typically for our range of absorbed fluences $\sim 50 - 150$ mJ/cm^2 and a bulk target the corresponding values are $T_i|_{\max} \sim 1.5$–3 kK, $T_e|_{\max} \sim 15$–25 kK.

(iv) Transition from 2T to 1T states.

(v) The stage up to nucleation. Nucleation takes place if $F_{\rm abs}$ is higher than the threshold of thermomechanical ablation.

(vi) Nucleation of voids in stretched liquid gold.

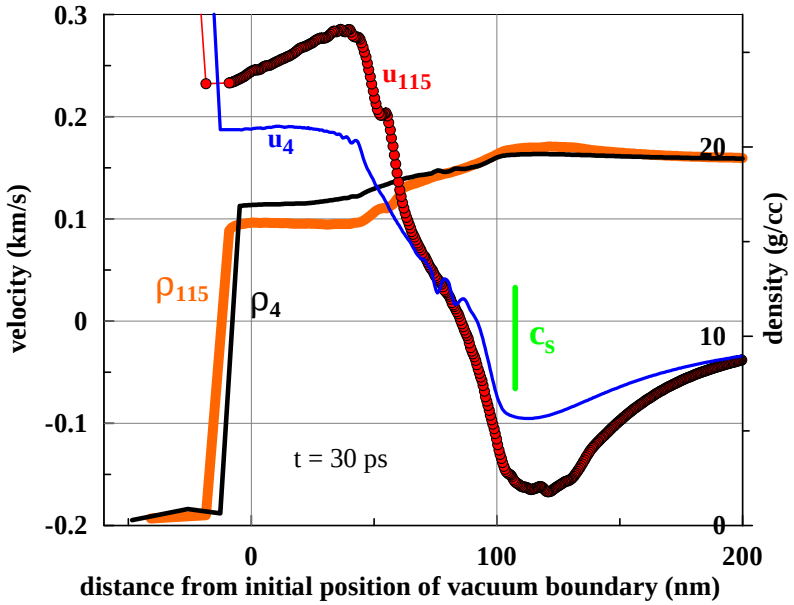

Figure 15. Velocity and density profiles for the case $F_{\rm abs} = 100$ mJ/cm^2, $t = 30$ ps. The indexes 115 and 4 correspond to $K_\alpha = 1.15$ (strong coupling) and $K_\alpha = 4$ (weak coupling) respectively. We see that difference in coupling rather weakly affect expansion velocity of the vacuum boundary. This is the boundary where the probe pulses are reflected. The boundary is sharp and gradients near boundary in condensed gold are small. Therefore Fresnel formula for reflection is accurate enough.

(vii) Forced expansion of foam. Foam locates between a spallation shell and bottom of the future crater.

Extraction of the stage (ii) is new, all other stages are known.

For thin films (their thickness d_f is of the order of or less than thickness d_T of a heat affected zone) the stage (ii) is different, because the conductive cooling of a skin and the corresponding electron temperature decrease become less significant. These changes (conductive cooling and T_e drop) are large especially in the ultrathin limit $d_f \ll d_T$.

In section 6 we consider the first four stages. They are the shortest stages lasting ~ 0.1–10 ps.

Let us consider the complex interplay of (i) dynamical consequences of 2T relaxation together with (ii) solid–liquid phase transition and (iii) hydrodynamics of expansion. Here, we are dealing with a 2T rarefaction wave expanding a substance where melting proceeds.

Example with a thin gold film $d_f = 30$ nm is presented first. The spatial step equal to $\Delta x^0 = 0.01$ nm is extremely small in this case. This is the step in the numerical Lagrangian scheme of integration of 2T hydrodynamics equations (5)–(9). Sound runs the spatial step during the time interval $\Delta x^0/c_s = 3$ fs. Smallness of these intervals allows smoothly simulate absorption of a femtosecond pulse.

6.1. Kinks and melting

Gold film 30 nm thick was used in the breakthrough experiments based on a chirped pulse probe technique [29–31, 33–35]. Presented 2T-HD simulations show that this is an instructive example of the 2T phase transformation in expanding gold. Of course, 2T relaxation and melting significantly influence dynamics of expansion. Kinematic characteristics of rarefaction to the left side are shown in figure 16. There are the pronounced three kinks in the velocity dependence

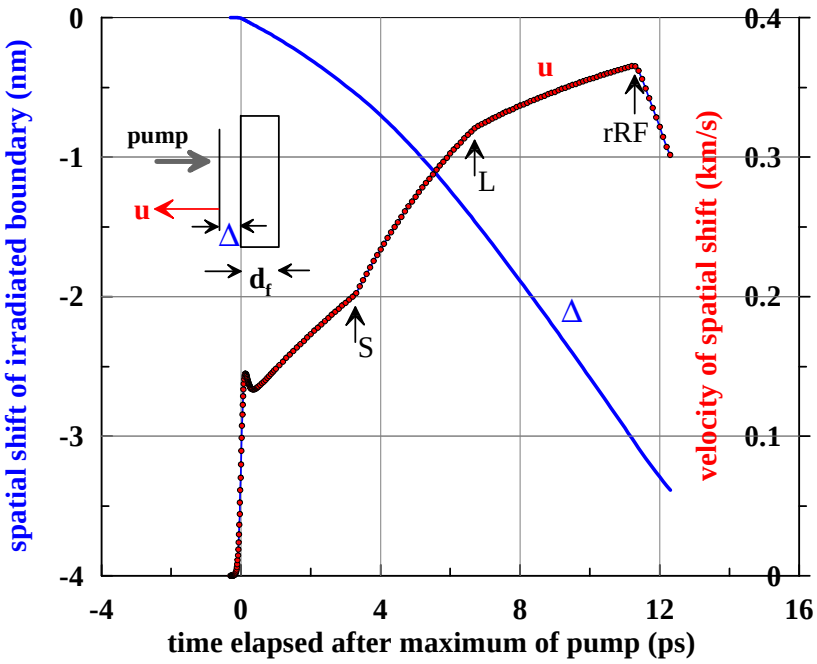

Figure 16. Expansion of a gold film after absorption of a laser pump pulse; absorbed energy 32 mJ/cm^2, duration $\tau_L = 100$ fs, $I \propto \exp(-t^2/\tau_L^2)$, absorbed energy per mass is 0.55 MJ/kg. Simulation has been performed for equation-of-state, conductance, and coupling with $K_\alpha = 4$ given in appendices. The sense of the plotted kinematic parameters (shift Δ and velocity of shift u) is explained in the internal picture showing a film with initial thickness d_f, a shift Δ of boundary of condensed gold, and velocity of shift u. Pump illuminate a film from the left side. We see the definite kinks "S", "L", and "rRF" on the dependance of velocity. They correspond to the beginning "S" and the end "L" of melting, and to arrive of the right rarefaction "rRF" (it is propagating from the right side a film) at the left side. The most important fact shown here is the acceleration (!) of the boundary *after* the end of the energy pumping.

$u(t)$ in figure 16. Figure 17 shows the kinks in the temporal dependence of ion temperature T_i corresponding to the velocity kinks. They relate to changes in compressibility during solid–liquid transformation thus causing the velocity reply.

Figures 16 and 17 present temporal dependencies (trajectory) of parameters at the left boundary (left edge) of a film, see inset in figure 16. Projection of the trajectory on to the plane of a phase diagram is demonstrated in figure 18. The point "rt" presents the equilibrium room temperature state, the point "Pe" corresponds to the rapid decrease of the edge point density as a result of fast increase of electron pressure p_e during a pump pulse. Duration of this density decrease is so short (relative to the electron-ion temperature equilibration time t_eq) that ion temperature remains almost unchanged. The points "S" and "L" present intersections of the trajectory with a strip-like region of a solid–liquid mixture. The strip is bounded from by the curves "sol" (solidus) and "liq" (liquidus). The edge point gradually melts during intersection of the strip.

It should be emphasized that melting near the boundary surface proceeds in stretched gold. Electron pressure expands (or it may be said "inflates") gold to negative ion pressures p_i. Thus negative values p_i compensate positive inflating electron pressure p_e and therefore total pressure $p = p_i + p_e$ equals to zero at the edge surface as it should be at a vacuum boundary. After

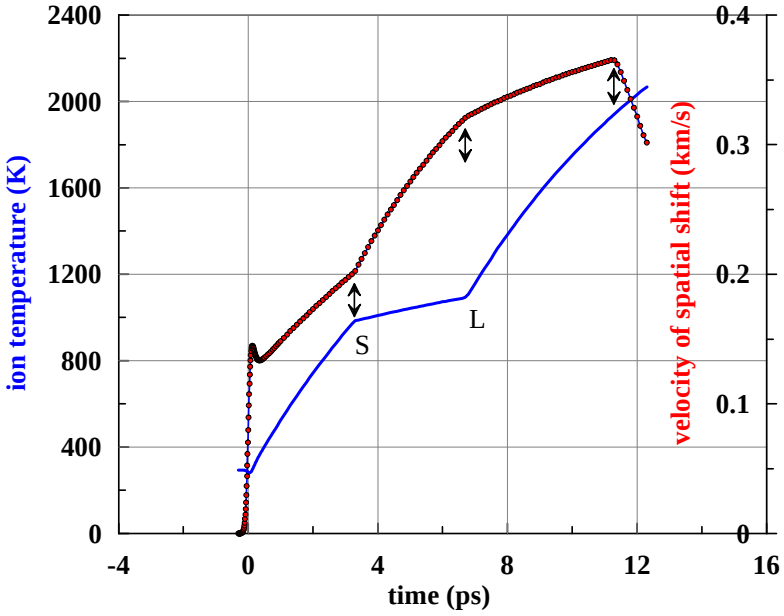

Figure 17. The kinks "S" and "L" limit the temporal interval of existence of a solid–liquid mixture at the left boundary of a film. Corresponding temperatures are below the triple point because this is melting in a stretched condensed matter, see explanations in text and next figure.

2T relaxation when electron temperature T_e drops down (and hence p_e decreases to negligible values) the trajectory returns back (it starts from the point "rt" at the curve "bin") to the binodal curve "bin". This part of the trajectory is not presented in figures 18 and 19. For the thin film the 2T relaxation lasts longer than for the bulk targets because the conductive cooling of electrons is absent. Also, the simulation shown in figures 16-19 has been performed for decreased value of an electron-ion coupling parameter α; $K_\alpha = 4$, see appendix B. Therefore value of T_e is still significantly higher than T_i at the end point "12 ps" of the trajectory shown in figures 16–19.

As it is described in appendix A, in our 2T-HD calculations we approximate 2T equation-of-state by a sum $F = F_i(\rho, T_i) + F_e(\rho, T_e)$ of free energies of electron and ion subsystem. We neglect relatively unimportant influence of electron temperature T_e on melting thus keeping the melting curve in the form $(T_i)_m(p_i)$ taken from the one-temperature (1T) case $T_m(p)$. Wide-range 1T equation-of-state (EoS) [19–21, 23] is employed in the 2T-HD code for the ionic part $F_i(\rho, T_i)$ of EoS. The EoS is written in the form that allows continuation of the melting phase transition into the metastable region located under the binodal "bin" in figure 18 [50, 56–59]. Therefore the curves "sol" and "liq" are continued to the left through the triple point "tr.p." in figure 18. In this approximation the transfer of gold into metastable states by inflating electron pressure p_e and gradual heating of ion subsystem by electron-ion coupling lead to the situation with the intersection of the melting strip under the binodal "bin". Comparison of the model of equilibrium melting used in 2T-HD code and kinetics of melting described by molecular dynamics (MD) code shows that in MD the kinks are smoothed but their positions are approximately the same [13].

As was said, the intersections with a melting strip during the entrance in and exit from the strip cause appearance of the kinks. It is known from previous papers [53, 60–62] that melting influences the shock formation process thus leaving traces on a shock profile. Melting affects

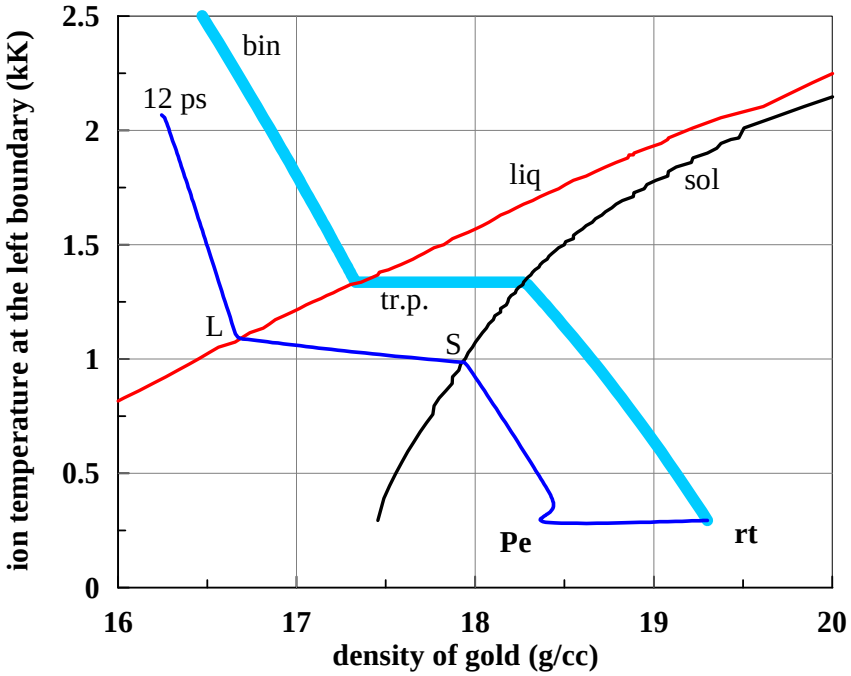

Figure 18. "Trajectory" of the left edge Lagrangian point at the phase diagram of gold. The trajectory connects the points "rt" → "Pe" → "S" → "L" → "12 ps". The sense of these notations is: rt—room temperature, Pe—electron pressure p_e effect, S—sol—solidus, L—liq—liquidus, 12 ps is the end of the computed example. The curve "bin" separates the stable and metastable regions, while "tr.p." is a triple point.

separation of a superelastic shock wave from a heat affected layer d_T. As we will see also in this paper, melting influences the optical reflectivity properties of a gold surface. Therefore it is not surprising that the solid–liquid phase transition (varying compressibility) affects the rarefaction wave. It should be emphasized that this is the 2T rarefaction. Electron to ion energy transfer during 2T stage increases total pressure which drives expansion. This circumstance accelerates expansion and change profile of a rarefaction wave relative to the more well-understood profile of the 1T rarefaction wave.

As we see, there are two ingredients in the game: one is the phase transition in the 2T state, while the another is the accelerated expansion, see figure 16 where velocity increases with time *after* finishing of a pump pulse.

6.2. Melting inside a film

Below we will consider situation inside a film before and after appearance of the first kink in figures 16 and 17. The three kinks appear in the time moments 3.3, 6.7, and 11.3 ps. Evolution of electron temperature in the edge Lagrangian particle contacting with vacuum is shown in figure 20. Evaporation rate depends on ion temperature T_i in our approximate 2T thermodynamics model $F = F_i + F_e$ with separation of electron and ion contributions, see appendix B. Temperature T_i is small and evaporation is negligible in our temporal range, thus the edge point may be called a boundary with vacuum.

Figures 21 and 22 demonstrate how thickness of a film d_f and e-i coupling α influence cooling of electrons. Decrease of thickness d_f relative to d_T sharply decreases duration and importance of conductive spread of heat from a skin. Enhancement of coupling also decreases duration and depth of conductive spread but not importance.

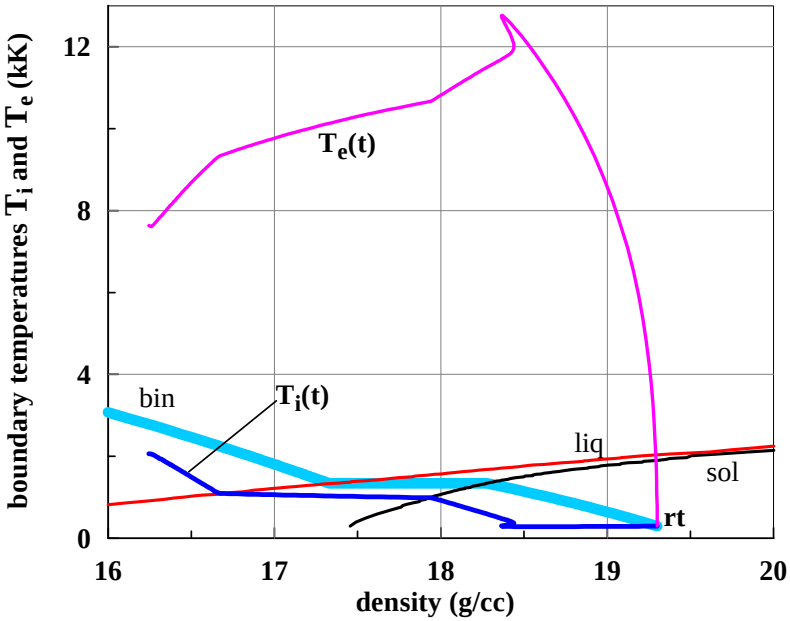

Figure 19. Moving of $T_i(t)$ and $T_e(t)$ with time along a phase plane. The trajectory $T_i(t)$, $T_e(t)$ starts from the 1T room state "rt", it exhibits sharp transition during action of a pump to the 2T state with high T_e and density ρ decreased by an action of p_e which inflates matter. After that $T_i(t)$ and $T_e(t)$ gradually approach each other during rather slow 2T relaxation. Heating of ions melts lattice transferring crystal to liquid through a wide strip of a mixture zone. At this stage the function $T_i(t)$ moves approximately along the isobaric curves $p_i(\rho)$ =const< 0 rather slowly intersecting the isobars and decreasing stretching as it tends to the binodal "bin". Decrease of stretching is caused by decrease of inflating pressure p_e. Finally the functions meet at the binodal in the 1T state. This final state is not shown here.

The role of conduction spread of absorbed heat is illustrated in figures 23–28. We compare the values at the vacuum boundary with values obtained by averaging over a skin-layer. Both the thin and the thick cases are considered. Below we will use the edge and the skin averaged values to calculate a reflection coefficient R and a phase of reflected probe wave φ. Calculations show that the values R, φ are in the first approximation the same. This validates using of Fresnel formula applicable in the case with a sharp jump of properties at the reflecting surface and homogeneous distributions of properties along a skin-layer.

Figure 23 demonstrates how fast electron conduction is, the difference between the vacuum edge value and the skin averaged value is very small. This is the example with a film $d_f = 30$ nm. The same situation with T_e evolution takes place in the case of a bulk target; therefore corresponding picture is not presented. Ion temperatures are slightly different at the vacuum boundary and in a skin, see figure 24. Averaging slightly smears the limits bounding the solid–liquid melting zone where a mixture of phases exists.

Interesting is the situation with ion temperatures at the vacuum edge and in the skin in the case of a bulk target. It is shown in figures 25 and 26. The rise of T_i continues up to $t \approx 25$ ps. This rise is supported by e-i heating from hotter electrons. The surface layer cools down at the later stage $t > 25$ ps thanks to 1T heat conduction transporting heat from surface to the bulk region. Projection of the trajectory shown in figure 25 on to the phase plane is presented in figure 27. We have to use a rather large spatial step 0.5 nm in the case of a thick target. Therefore the numerical solution is not so smooth as it is in the case of a thin film $d_f = 30$ nm where the step is 50-times smaller.

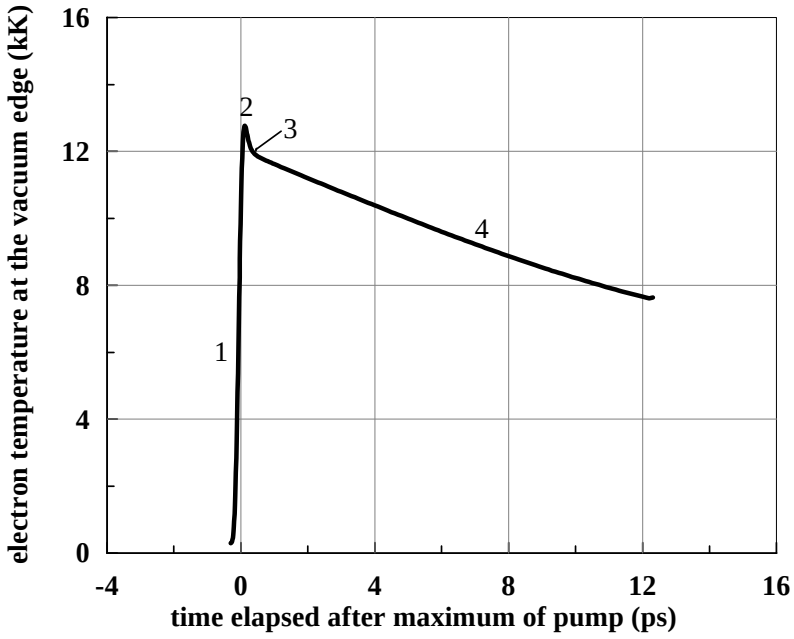

Figure 20. Increase of T_e during absorption of a pump and decrease as a result of cooling of electrons. The rise 1 corresponds to the stage (i) in the list of stages in the beginning of subsection 6.1 "Kinks and melting". The rise finishes in the maximum point 2 at the instant $t_{\max} \approx 100$ fs when the pump $I(t) \propto \exp(-t^2/\tau_L^2)$ ends; $\tau_L = 100$ fs in our simulations. The points $2 \to 3$ ($t \approx 350$ fs) limits the stage (ii) of the mainly conductive cooling of a skin. Thickness $d_f = 30$ nm of a film is comparable to the skin 15 nm, thus the stage (ii) is short and the drop of T_e at this stage is small. T_e is almost homogeneously distributed across thickness of a film after the stage (ii). The part 4 of the dependence presents practically entirely e-i cooling.

From trajectory at a phase diagram in figure 27, we see that the 2T stage finishes at the instant ≈ 25 ps. Then electron pressure becomes negligible, it ceases to inflate gold. Therefore trajectory returns from the metastable region to binodal. After that, obviously, the vacuum point has to belong to the binodal curve. This point evolves along the binodal decreasing temperature thanks to conductive cooling into the bulk side. Continuous cooling finally leads to freezing of a molten layer. Beginning of freezing is shown in figures 27 and 25. Temperature at the vacuum end and in the skin drops down to melting temperature of gold 1.337 kK.

Figure 28 demonstrates evolution of surface density. Trajectories of the edge point and the skin-layer are presented. They are shown for the two cases with thin and bulk targets. The spatial step 0.01 nm for a thin film is 50-times less than the step in the thick case. Rather large spatial step 0.5 nm results in oscillations at the early stage in the case of a bulk target. We see that rapid increase of electron pressure causes rapid drop of density of the vacuum edge particle. But the drop quantitatively is rather small–and it is not seen in the skin averaged trajectories.

As was said, rapid increase of electron pressure during a pump $-\tau_L < t < \tau_L$ causes rapid drop of the vacuum edge density in figure 28. Later this impact-like dynamic action propagates along acoustic characteristics into the internal region. The propagation is shown in figure 29. The digits 1, 2, 3, and 4 in figure 29 correspond to the same designation in figure 20. We will return to this question in subsection 6.3. It is explained their why it seems that the acoustic signal (or trace) 1–2–3 goes up on a pressure profile.

Let us consider the profiles before and after the instant $t = 3.3$ ps of appearance of the first kink at the trajectory shown in figures 16 and 17. The profile before is given in figures 29, 30,

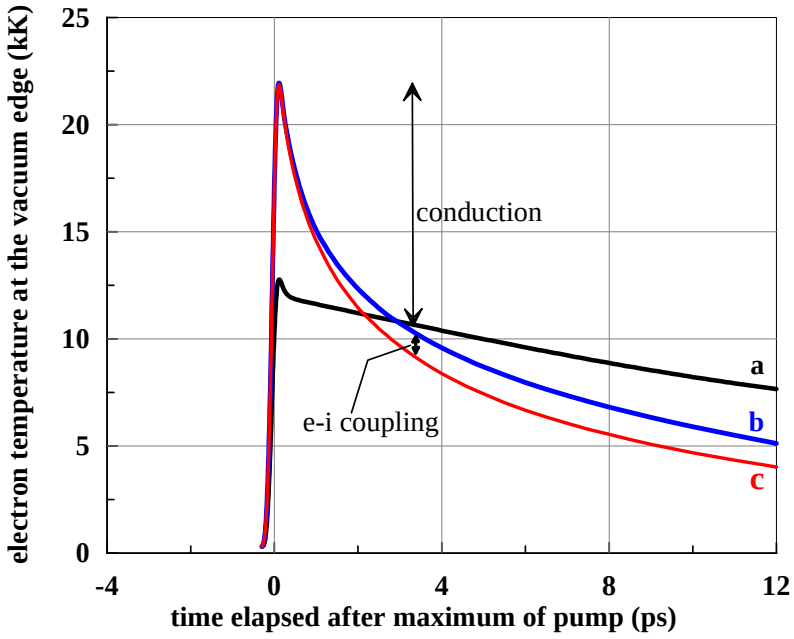

Figure 21. Conductive cooling of a surface layer lasts longer if a film is thicker. In this place, we compare a thin film $d_f = 30$ nm from figure 20 (very short conductive stage 1–2–3 in figure 20, this is the curve "a" here) with a bulk target (the curves "b" and "c"). Thickness of a heat affected zone $d_T \approx 100$–150 nm is significantly larger than $d_f = 30$ nm. Therefore the conductive transport of absorbed heat from a skin takes longer time. The curves "b" ($K_\alpha = 4$) and "c" ($K_\alpha = 1.15$) correspond to different e-i cooling rates, see appendix B. The coupling parameter α is significantly higher in the case of the curve "c". Estimates of relative importance of the conductive cooling and the coupling cooling are emphasized by the arrows "conduction" and "e-i cooling".

and 31. The current position of the point $p_i = 0$ divides the Lagrangian particles in stable and metastable states. The right wing rRF starts slightly later in time relative to lRF. The wave rRF starts when the supersonic electron conduction achieves the rear-side boundary (the right side of a film in figure 29). It takes small but finite time ≈ 350 fs during the stage (ii) when conduction dominates the coupling.

All Lagrangian particles of a film belong to a solid state at the instant 3.2 ps shown in figures 29, 30, and 31. But the both vacuum boundaries are very near to the melting strip, see figure 31. The vacuum boundary of the lRF wave first (slightly before the rRF) touches the strip at the instant $t = 3.3$ ps. The intersection of the solidus curve "sol" by the profile in figure 31 causes appearance of the first kink at the trajectory in figures 16 and 17.

The e-i heating of ions is the main thermal process at the stage (iii) (see the list in the beginning of section 6). This heating brings gold closer to the melting strip. The power of heating per unit of volume or mass (expansion velocities are small relative to sound speed c_s) is approximately homogeneous across a film. Thus a whole layer transfers from the solid state in the solid–liquid mixture state when ions in this layer accumulate some fraction of latent heat of melting. Larger fraction of liquid in a mixture composition relates to a larger portion of latent heat.

The power of heating regulates velocity u_{phase} of the solid–mixture separation surface shown in figure 32. This is a phase velocity, therefore it may be arbitrary high for large powers. Velocity u_{phase} is supersonic with Mach number ≈ 2 in the case shown in figures 32 and 33. In these

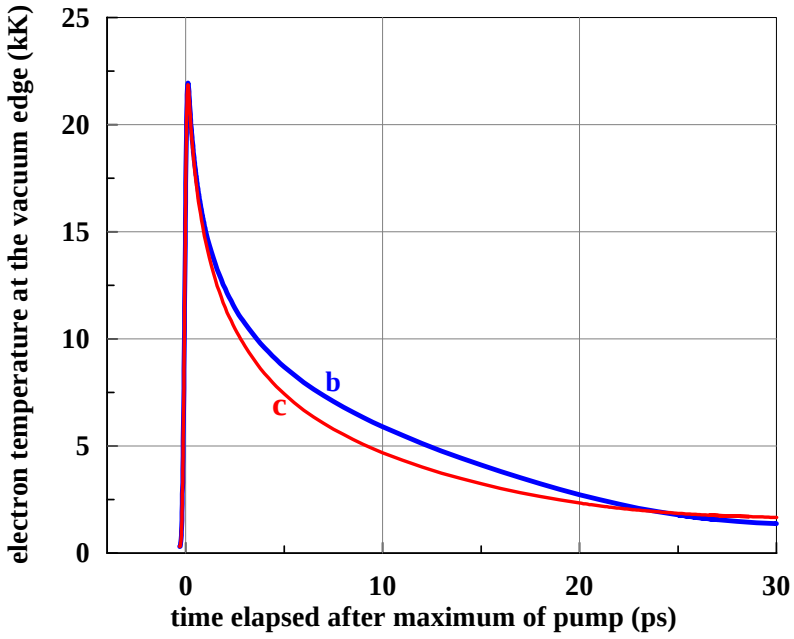

Figure 22. Stronger coupling faster transfers electron energy E_e into ion energy E_i. Thus the conductive time is shorter in the case "c" ($K_\alpha = 1.15$) than in the case "b" ($K_\alpha = 4$), and the heat affected zone d_T is thinner, then final equilibrium temperature $T \approx T_i \approx T_e$ is larger in "c", and ablation threshold is smaller in "c". Maximum T_e in the moment $t \approx 100$ fs is achieved at the end of a pump with duration $\tau_L = 100$ fs for all three case "a", "b", and "c" in figure 21.

figures the vacuum boundary is "V" and "c_s" is sound speed. There is significant negative ion pressure in the point "V". It is created by an inflating action of electron pressure p_e.

At the instant $t = 3.3$ ps the point "V" touches the solidus, the first kink in figures 16 and 17 appears, and the two surfaces "c_s" and "u_{phase}" begin to propagate into the film from the edge "V". The phase transfer runs with supersonic velocity u_{phase}. Therefore in the range between the fronts "c_s" and "u_{phase}" gold hasn't time to expand. In this situation the e-i heating pumping energy into an ion subsystem increases ionic pressure because "normally" the specific volume of liquid is larger, but, as was said, in the range "c_s"–"u_{phase}" gold hasn't time to unload. The unloading begins behind the sonic front "c_s".

The rise of ion pressure thanks to supersonic solid–liquid phase transition is demonstrated in figure 34. The rise is a result of e-i heating of ions. The filled circles shows positions of Lagrangian particle at the time moments $t = 3.2$ and 4 ps. Gold expands to the left side in the lRF wave, see figure 29. Velocity of expansion is ≈ 190 m/s in the time range $3.2 < t < 4$ ps for this Lagrangian particle. Thus the spatial shift is ≈ 0.15 nm.

During this shift the unloading necessary to decrease p_i is absent because the sonic front "c_s" does not yet achieve the marked Lagrangian particle. Therefore rather powerful e-i heating rises pressure p_i because it increases a fraction of liquid in a mixture. Total pressure $p = p_i + p_e$ increases with p_i because electron pressure profile (together with electron temperature) is almost constant across a film. This is a rather surprising way of melting in a 2T target excited fast by a femtosecond pump. The melting causes significant consequences in hydrodynamics of 2T expansion.

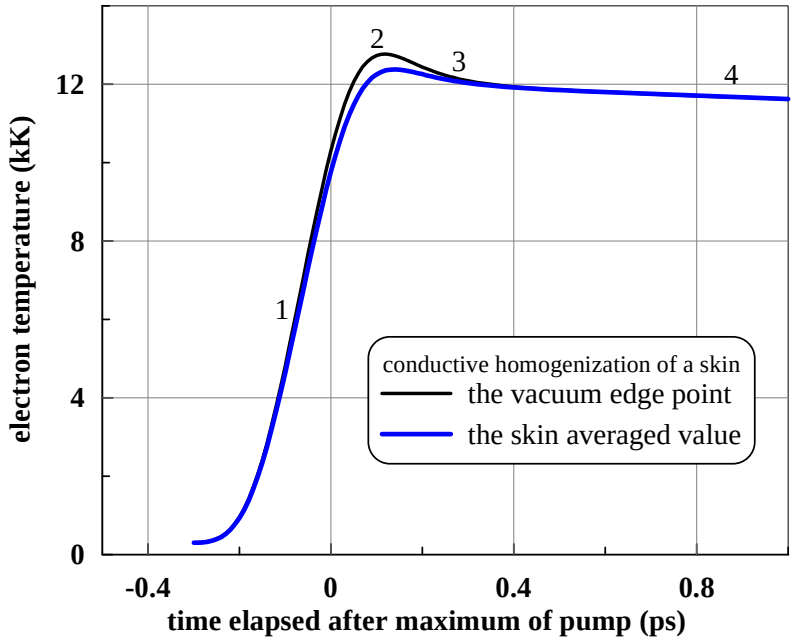

Figure 23. Comparison of the edge electron temperature T_e with the over skin averaged value. Very fast homogenization of T_e across a skin takes place. The case of a film is presented: $d_f = 30$ nm, $F_{\rm abs} = 32$ mJ/cm^2, $K_\alpha = 4$, average energy per unit of mass is 0.55 MJ/kg, the sense of the digits 1, 2, 3, 4 is the same as in figure 20.

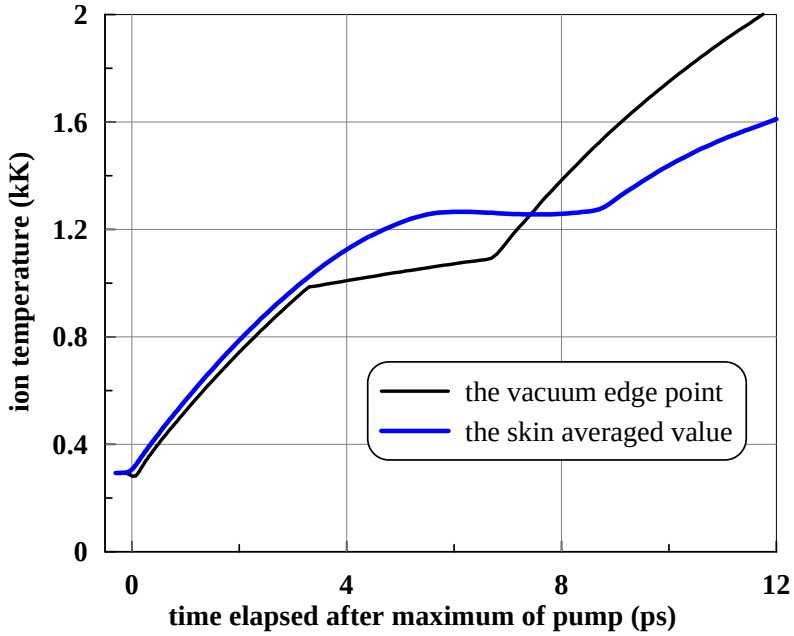

Figure 24. Comparison of the edge ion temperature T_i with the over skin averaged value. Parameters of a film and a pump pulse are the same as in figure 23. The horizontal steps appear thanks to melting transition (see subsection 6.1).

6.3. Electron-ion energy transfer and acceleration of boundary

Above we analyze a 2T rarefaction (RF) wave with a solid–liquid phase transition. A thin film was used because it has been integrated with a very small spatial step. This example is interesting

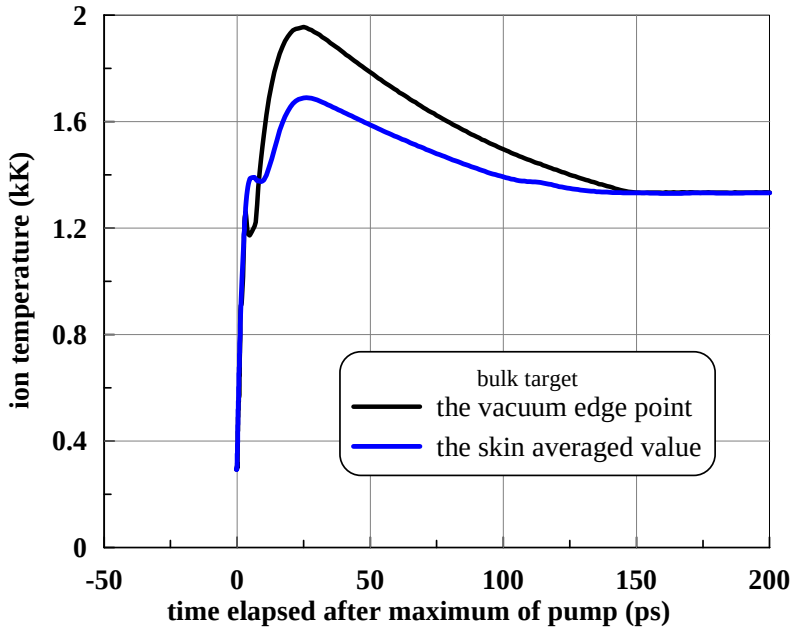

Figure 25. Difference in ion temperatures between the edge value and the skin averaged value. This is a bulk target, $F_{\rm abs} = 100$ mJ/cm^2, $K_\alpha = 4$. After $t \approx 150$ ps the skin returns to the triple point with melting temperature 1.337 kK.

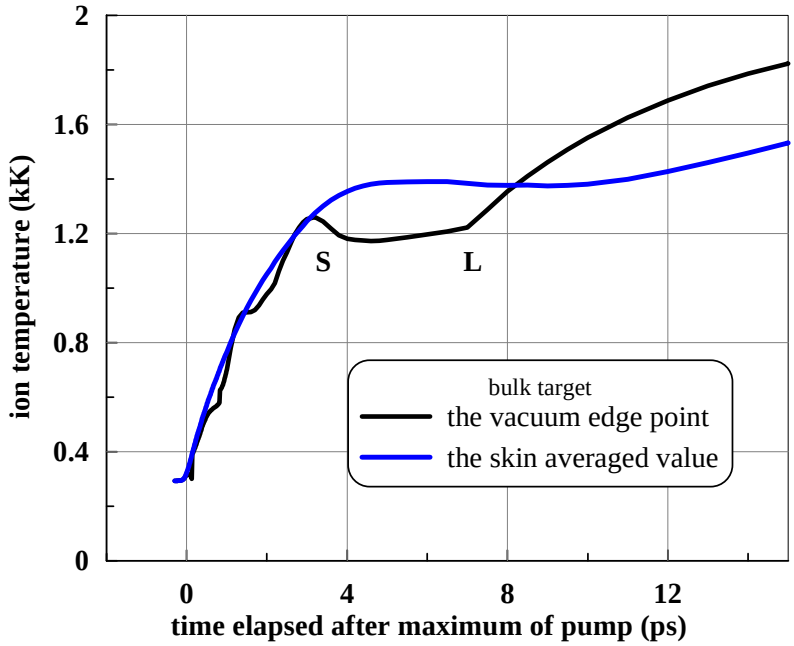

Figure 26. Early stage including melting near vacuum boundary. This is the initial piece of the trajectory $T_i(t)$ shown in figure 25. The points "S" and "L" correspond to intersection of a melting strip, compare with figures 17 and 18. We use much smaller spatial step 0.01 nm in the finite-difference numerical scheme in the case of a thin film $d_f = 30$ nm. In the case of a bulk target the step is 0.5 nm.

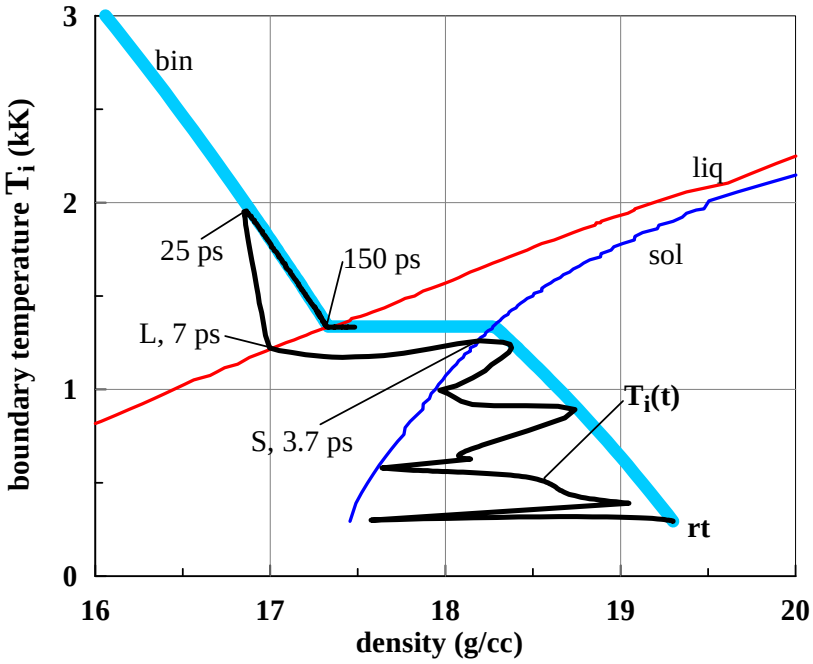

Figure 27. Trajectory of a surface point of a bulk target on phase diagram of EoS of gold [19,20]. The trajectory starts from the room temperature conditions "rt", compare with figure 18. Oscillations between binodal and solidus are caused by rather large spatial step of integration of system of 2T-HD equations. It is useful to match the sequence of time instants 3.7, 7, 25, and 150 ps with figures 26 and 25.

also because it was employed in the experiments [29–31, 33–35]. Above it was emphasized that electron-ion (e-i) coupling and e-i heating of ions do melting non-trivial. Deformation of the RF profile and acceleration of expansion are another aspects linked to the e-i heating.

These aspects are unusual. The 1T rarefaction wave running from the vacuum side into the homogeneously heated semi-space is a simple classical example of decay of a pressure jump into vacuum in dynamics of gas. For $t < 0$ there is a homogeneous semi-space with pressure $p > 0$ separated from another semi-space by a rigid wall. The another semi-space is vacuum with $p = 0$. At the instant $t = 0$ the wall is removed and expansion of gas into vacuum begins.

A continuous density profile appears for $t > 0$ where density changes from 0 at the head of the RF wave to the unperturbed value corresponding to gas at $t < 0$. The profile is covered by a fan of characteristics propagating against an expansion flow. The same RF wave has been analyzed for the case of a pressurized $p > 0$ semi-space but now filled with condensed matter [63–66]. In the condensed case the plateau inside the RF profiles exists. This is opposite to the gas case with expansion in vacuum where the profile is a monotonous function. The plateau is linked to a point at a binodal curve. In the gas case the binodal and the two-phase region encircled by the binodal are absent.

The case with plateau and permanent pressure inside the unperturbed region corresponds to the 1T unloading of condensed matter. This case is shown in inset (a) in figure 29. The plateau is the part A–B of the RF profile A–B–C in inset. Pressure $p = 0$ at the plateau. This corresponds to unloaded in vacuum condensed material. But density is finite at the plateau. The vacuum edge A of the plateau moves with constant velocity, while pressure remains unchanged in the unperturbed region. In figure 29 this is a region to the right side relative to the point C. Namely the unperturbed pressure drives drives expansion motion.

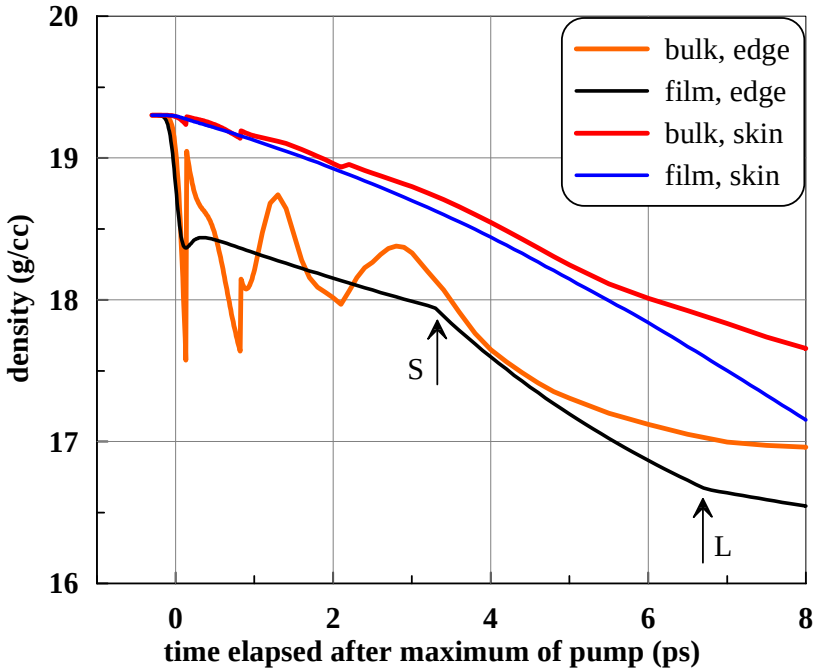

Figure 28. Difference in density between the edge value and the skin averaged value. Here we compare results of the 2T-HD simulations of a film and a bulk target. Parameters of a film are given in figure 23, parameters of a bulk target are in figure 25.

In the 2T RF wave shown in figure 29 the situation changes qualitatively. First of all the driving pressure in the unperturbed region increases in time, see the arrow "increase of p" at the top of the profile in figure 29. The increase is caused by e-i energy transfer from electrons to ions. Larger pressure corresponds to the same amount of energy isochorically transferred from electrons to ions. Indeed, the Gruneisen parameter Γ is higher for ions: $\Gamma_i > \Gamma_e$, $\Gamma_i \approx 2$, while $\Gamma_e \approx 0.7$–1 according to the density functional theory (DFT) calculations [21, 22, 67]. For the ideal Fermi-gas the value Γ_e is equal to $2/3$. Energy per unit of mass 0.55 MJ/kg is equal to 10.6 GPa for energy per unit of volume in the case of normal density gold. This gives ≈ 21 GPa for p_i and ≈ 11 for p_e.

The difference between the p_e and p_i gradually releases during the 2T relaxation. This release deforms the 2T RF plateau from the constant value A–B as in inset (a) in figure 29 to the triangular type in the same figure. The slope 4 of the 2T RF wave in figure 29 corresponds to the plateau of the 1T RF wave.

The release $E_e \to E_i$ increasing p_i and total pressure $p = P_i + p_e$ accelerates expansion. Therefore velocity of the vacuum edge "V" defined in figure 33 increases with time as it is shown in figures 16 and 17. While in the 1T RF wave this velocity is constant.

6.4. Estimate of expansion velocity at early stage

Electron temperature distributions at early stage (beginning of 2T stage) are presented in figure 35. We see that the rate of e-i coupling does not influence profiles of electron temperature T_e. There is moderate difference between a film and a bulk target at this early instant. The right end of a film $d_f = 30$ nm shown in figure 35 is thermally isolated–boundary with vacuum. This boundary stops thermal flux and $\nabla T_e = 0$ at the boundary. While in a bulk target the flux is flowing into depth of a target: $\nabla T_e \neq 0$ at depth 30 nm under vacuum surface. Corresponding electron energy distributions are given in figure 36. Again we see that variation of a coupling

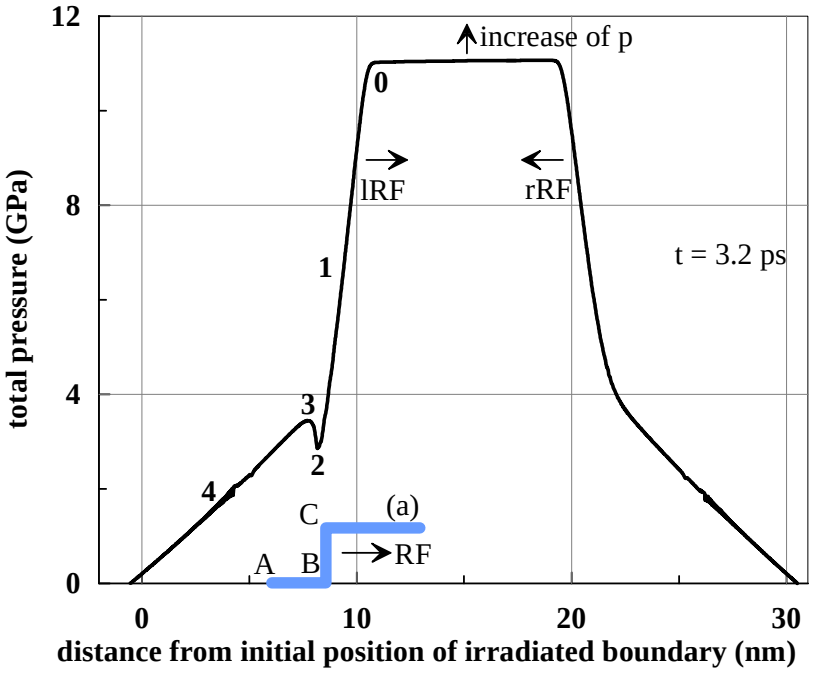

Figure 29. Propagation of the left rarefaction wave (lRF) and the right rarefaction wave (rRF) from the left (irradiated by pump) and the right (rear-side) vacuum sides of a film $d_f = 30$ nm, $F_{\rm abs} = 32$ mJ/cm^2; the instant $t = 3.2$ ps is presented. Very short (for thin film) stage (ii), see beginning of section 6 "Kinematics of a surface layer. Early stages", produces stretching of a very thin sublayer (thinner than skin). The signal about this stretching runs in the head of the lRF. It is absent in the profile of the rRF. The points 1–2–3–4 relate to the same points in figure 20. The inset (a) shows the rarefaction wave running to the right side in the 1T state.

parameter is thermally insignificant at the early stage when heat redistribution processes are dominated by electron conduction. We take the values of electron energy E_e at the depth 2 nm and plot them as a function of absorbed energy $F_{\rm abs}$ in figure 37. There is a small difference between the film and bulk targets. We base our estimate of velocities at very early stage on this fact. Total pressure distributions corresponding to figures 35 and 36 are presented in figure 38. There is splitting of the pairs of the curves 3 and 4 from figures 35 and 36 in the case of the pressure profiles. It is caused by a higher rate of energy transfer from hot electrons to ions thus intensifying the rate of ion pressure increase. There is a significant (few times) difference in coupling parameter between the curves in the pairs therefore the value of splitting gives a measure of ion pressure. This is true everywhere except the very thin unloaded surface layer where ion pressure is attempting to compensate inflating action of large electron pressure.

Pressures are large but still significantly less than a bulk modulus B of gold equal to 180 GPa. Therefore the linear acoustic approximation may be used for estimates. Let us use it for defining of expansion velocities. We know well expansion velocity in the simulation of a thin film $d_f = 30$ nm and $F_{\rm abs} = 32$ mJ/cm^2, see figure 16. It is equal to $u \approx 140$ m/s. According to acoustic theory the velocity is $u = p/Z = (p/B)c_s$, where $Z = \rho\, c_s$ is acoustic impedance. Taking maximum pressure 7.9 GPa for the curve 1 in figure 38 and the unperturbed values for density and speed of sound in gold, we obtain $u = 136$ m/s for plastic speed of sound 3 km/s and $u = 124$ m/s for elastic speed of sound 3.3 km/s. We see that these values are close to the value obtained in simulation and presented in figure 16. Thus the acoustic approximation is valid.

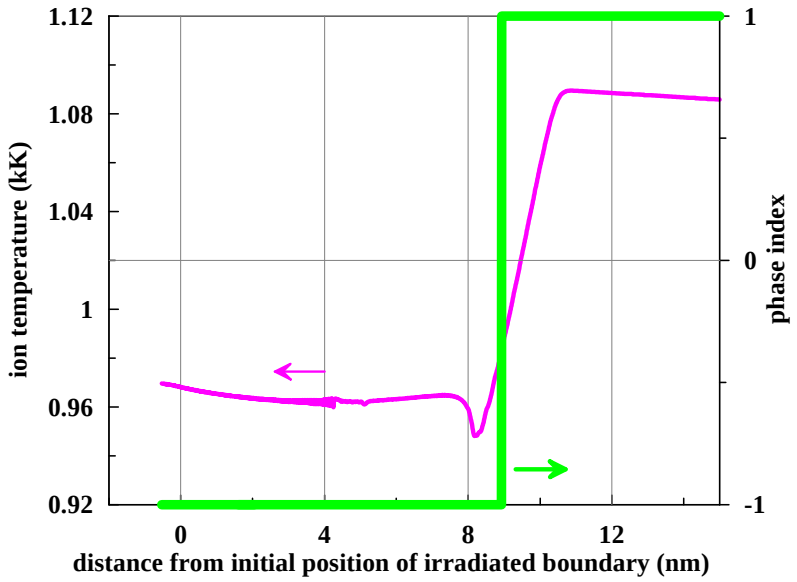

Figure 30. Ion temperature and phase index corresponding to figure 29, $t = 3.2$ ps. The left wing of the whole profile from figure 29 is presented. This wing relates to the lRF wave moving from left to right in figure 29. The phase index shows the state of gold: "1" is stable solid, "−1" is metastable (stretched) solid, see figure 31.

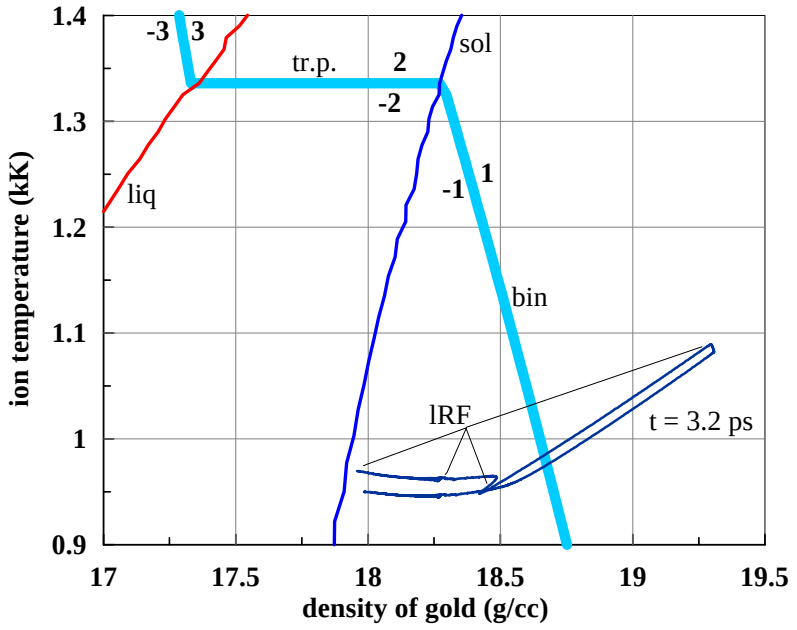

Figure 31. Instant distribution of ion temperature $T_i(\rho; t = 3.2\,\text{ps})$ across a film shown at the phase diagram; $d_f = 30$ nm, $F_{\text{abs}} = 32$ mJ/cm^2, 0.55 MJ/kg. The distribution repeats the profile in figure 29 with its left (lRF) and right (rRF) wings. Even the trace 1–2–3 is seen well in the left wing. The pairs of digits 1––1,2––2 and 3––3 relate to stable and metastable states of solid, solid–liquid mixture, and liquid respectively. The stable and metastable states are separated by the binodal curve "bin". Other designation are the same as in figure 18.

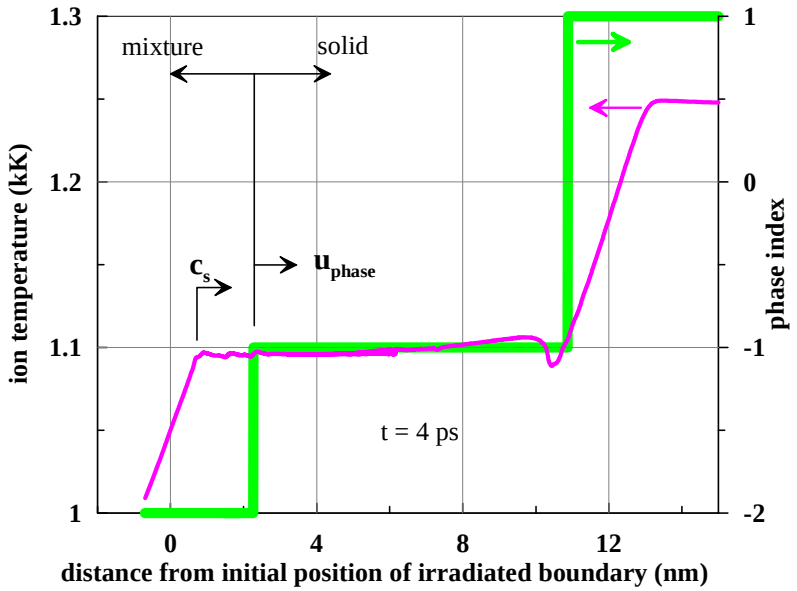

Figure 32. Profiles of T_i and phase index (defined in figure 31) for the instant 4 ps. At the instant 3.3 ps the vacuum edge of the rarefaction wave lRF crosses the solidus. Thus a mixture layer appears inside the lRF wave. At the instant 4 ps the mixture covers the range between the vacuum edge and the front $u_{\rm phase}$. There is the additional sonic wave with the front "c_s" inside the mixture layer. The front "c_s" leaves the vacuum boundary at the instant 3.3 ps together with the front $u_{\rm phase}$. It is behind the melting front $u_{\rm phase}$ because the melting front propagates supersonically.

Our task in this paper is to consider the surface phenomena where thermal effects are dominating. Generation and long distance propagation of elastic-plastic, polymorphic, and melting shocks is not considered here, see [60, 68–74]. Therefore we use a plastic model of solid body in the presented set of 2T-HD simulations. Thus we did not add the term with a shear modulus G into 2T-HD hydrodynamic equations as it was done in papers [75].

The acoustic approximation allows us to estimate early expansion velocities for the cases 2, 3, and 4 shown in figures 35, 36, 37, and 38 with 3–4 times higher absorption energies $F_{\rm abs} \approx 100$ mJ/cm^2. Direct definition of velocities in these cases from simulation profiles is difficult because in the cases with the thick targets where we have to use rather large spatial steps 0.5 nm it is difficult to define where the boundary is. While in the case of a thin film $d_f = 30$ nm and enhanced energy $F_{\rm abs} = 90$ mJ/cm^2 (which we simulate with extremely small step 0.01 nm) the complicated processes take place in a ultrathin surface layer with thickness of the order of few nanometers where something like "cold or electron evaporation" proceeds, see figures 2–5 in [6] and [76]. In the ultrathin layer a group of high velocity Lagrangian particles appears masking the average hydrodynamical expansion velocity. These problems are outside the scope of this paper. It seems that nevertheless the acoustic estimates following from mass and momentum balance are approximately applicable.

Using mass and momentum conservations at a weak rarefaction front, we obtain velocities for the 6 profiles presented in figure 38. They are: the curve 1: $p_{\rm max} = 7.9$ GPa, $u = 136$ m/s; the curve 2: $p_{\rm max} = 24$ GPa, $u = 420$ m/s; the curve 3 blue: $p_{\rm max} = 26$ GPa, $u = 450$ m/s; the curve 3 red: $p_{\rm max} = 27$ GPa, $u = 470$ m/s; the curve 4 blue: $p_{\rm max} = 35$ GPa, $u = 600$ m/s; the curve 4 red: $p_{\rm max} = 36$ GPa, $u = 620$ m/s. The weak rarefaction front propagates into depth of a target after ultrashort pumping. These velocities are shown in figure 39 as the filled circles.

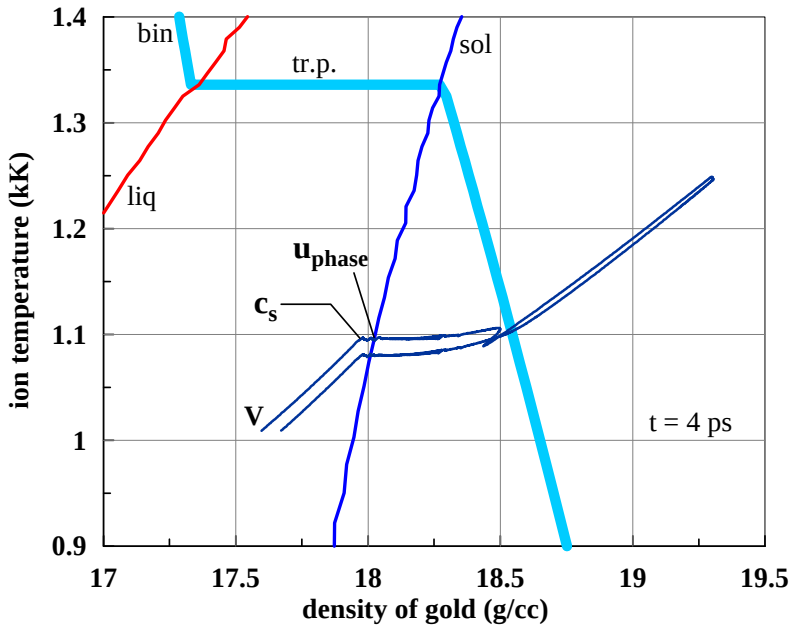

Figure 33. The image of the profile shown in figure 32. This is the image on a thermodynamic map of gold at the instant 4 ps. Compare the profile 4 ps with the profile 3.2 ps at the same map in figure 31. There is a sonic part "V"–"c_s" inside a melting zone. Density and ion temperature are approximately constant at the another part "c_s" and "$u_{\rm phase}$" of the melting zone. Therefore the length of this part is small at the map relative to the part "V"–"c_s" where significant changes in ρ and T_i take place.

In figure 39 the velocity histories for the bulk targets begin from some gap after the pump arrival. We erase the velocity variations in the gap for the bulk targets because they oscillates during the few first picoseconds as it is shown in figure 27. Approximate velocity history in the gaps are shown by the dashed straights connecting the appropriate circle and the smooth part of the corresponding curve. We see that for the bulk targets presented in figure 39 velocities decrease at the early 2T stage. This is the opposite trend relative to the case of thin film shown by the curve 1 in figure 39, see also figure 16.

This difference is consequence of strong conductive cooling. In the bulk targets there is a lot of cold volume outside to the current heated layer. Conductivity transfers electron energy into this volume, thus decreasing amount of energy transited to ion subsystem from electrons in the current hot layer. As was said above, Gruneisen parameter is higher for ions, see subsection 6.3. This fact increases velocity in time in the case of a thin film where the conduction loses are working only during very short time interval.

Below we consider the middle stage when a rarefaction (RF) wave sent from vacuum boundary crosses the depth d_T of a heat affected zone. At this stage (a) and above an ablation threshold (b) the nucleation in stretched liquid gold begins. Initial velocity is necessary for acoustic estimates of strength of liquid. But we see that the initial velocity is rather pure defined. It seems that the maximum velocities at the continuous curves 3 blue, 3 red, and 4 blue in figure 39 should be used for such estimates. Because velocities in the gaps in figure 39 belongs mainly to the small (for the energy range $F_{\rm abs} \sim 100$ mJ/cm^2) amount of the evaporated layer.

From the other hand these maximum velocities, as we see, are more sensitive to e-i coupling than to the value of $F_{\rm abs}$ in the range 100–130 mJ/cm^2. The decrease of velocities in figure 39 after the time range 10–15 ps is due to resistance of 1T gold to stretching.

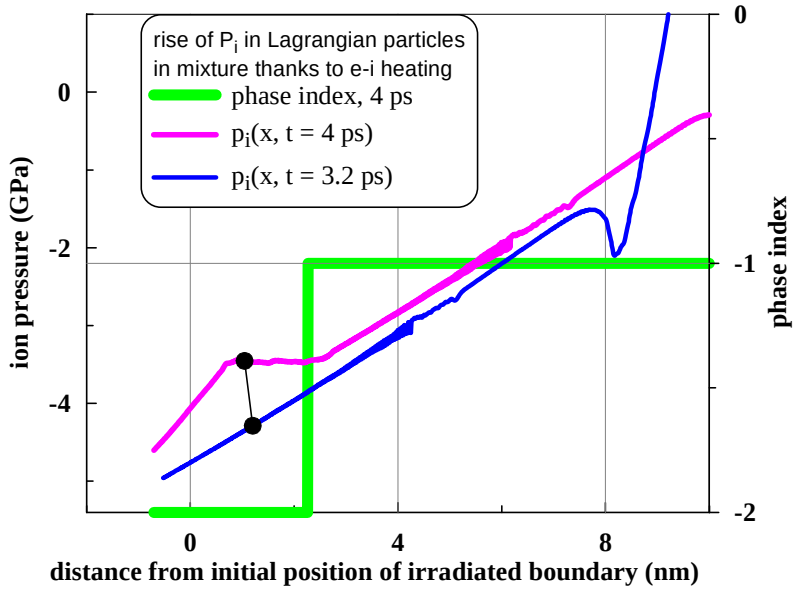

Figure 34. The pressure profiles before and after the instant 3.3 ps when the vacuum edge "V" achieves the solidus. The edge "V" is defined in figure 33. The mixture layer appears and the two fronts "c_s" and "$u_{\rm phase}$" begin to run from the boundary "V" when $t > 3.3$ ps. These fronts are shown in figure 32. Positions of the some particular Lagrangian particle are marked by the filled circles. The particle is chosen arbitrary inside the instant range between the two fronts "c_s" and "$u_{\rm phase}$" for the moment $t = 4$ ps.

6.5. Middle stage

Above we have considered situation around the maximum velocity, see figure 39. The beginning of deceleration of the surface is also seen in figure 39. Let us follow how the surface behaves at a longer time interval. This is shown in figure 40. We see that deceleration continues up to almost total stop of motion of the surface. This is not surprising, indeed, corresponding energy $F_{\rm abs} = 100$ mJ/cm^2 putted into substance is close to the ablation threshold.

The smooth "bridge" (the dashed straight) in figure 39 connecting the estimate of initial velocity 450 m/s and the vicinity of the maximum point "a" in figure 40 is not shown here. The oscillations filling the gap between the point 450 m/s at the instant 0.1 ps and the point "a" in figure 40 are not presented in figure 39. The oscillations appear thanks to rather large spatial step 0.5 nm used in simulations of a bulk target. They are well seen in figure 27. The oscillations last during the first few picoseconds–≈ 4 ps before beginning of melting in figure 27.

Interesting is the situation around the point "b" in figure 40. At first sight this point seems like an instant when the spallation shock arrives from the nucleation layer to the boundary with vacuum. If this indeed is the case then people estimates the strength $p_{\rm st}(T)$ of gold in the nucleation layer under temperature T as $p_{\rm st} \approx \rho\, c_s\, (u_a - u_b) \approx B\, ((u_a - u_b)/c_s)$, where $B = \rho\, c_s^2$ is a bulk modulus, $B = 180$ GPa in solid room temperature gold, and u_a, u_b are surface velocities in the points "a" and "b" in figure 40. We obtain $p_{\rm st} = 7$–11 GPa varying $\rho = 16$–18 g/cm^2, $c_s = 2$–3 km/s in this linear acoustic estimate. But inspection of the spatial profiles of the run $F_{\rm abs} = 100$ mJ/cm^2, $K_\alpha = 4$ given in figure 40 shows that nucleation is absent.

Of course, simulation of nucleation in the 2T-HD code demands special conditions. It is supposed that nucleation begins or when a system arrives to the states where the dependence $p(\rho, s = \text{const})$ (taken from equation of state used in simulation) begins to grow with decrease of density ρ, or when the tensile stress achieves the prescribed limit. The limit may be or some

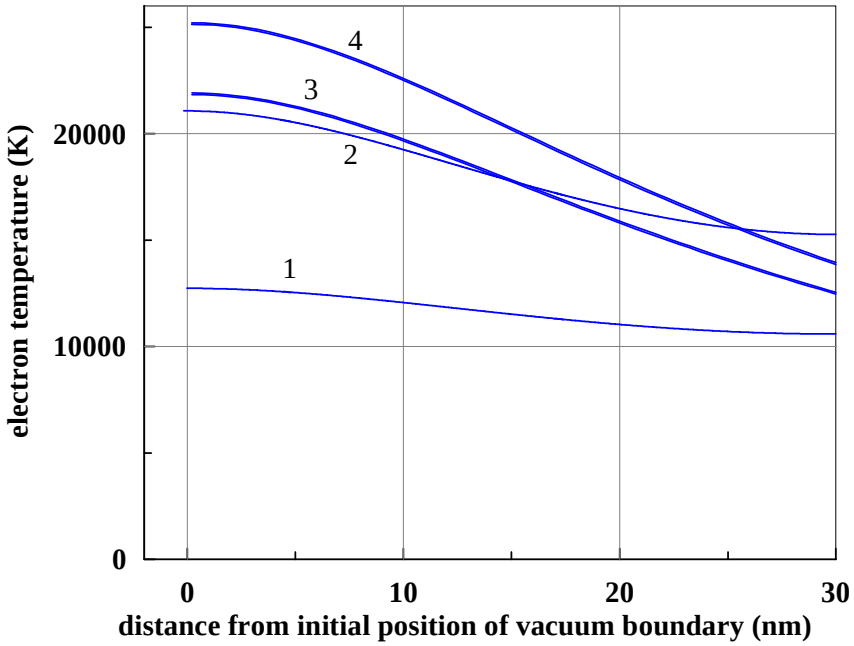

Figure 35. Profiles $T_e(x, t = 0.1\,\text{ps})$ at time moment $t = 0.1$ ps. This is the end of a pump pulse. The curves are: (curve 1) film, $d_f = 30$ nm, $F_{\text{abs}} = 32$ mJ/cm^2, 0.55 MJ/kg, $K_\alpha = 4$; (curve 2) film, $d_f = 30$ nm, $F_{\text{abs}} = 90$ mJ/cm^2, 1.55 MJ/kg, $K_\alpha = 4$; (two curves 3) bulk target, $F_{\text{abs}} = 100$ mJ/cm^2, $K_\alpha = 1.15$ and $K_\alpha = 4$; (two curves 4) bulk target, $F_{\text{abs}} = 130$ mJ/cm^2, $K_\alpha = 1.15$ and $K_\alpha = 4$.

constant value, or depends on local conditions: the values of tensile stress, temperature, and deformation rate. It is difficult to follow the situation after nucleation in hydrodynamics code. In Lagrangian code the nucleation point x_{i^*} breaks the chain x_i of Lagrangian points; here the index i runs the chain. After that it is supposed that pressure is zero $p = 0$ in the points $i^* - 1$ and $i^* + 1$ bounding the empty gap. In the another versions the negative pressure at the boundaries of the gap depends on the current width $|x_{i^*+1} - x_{i^*-1}|$ of the gap.

The minimum in the point "b" in figure 40 is, may be, the trace from the instant when the strongest stretching passes the solidus separating solid–liquid mixture from solid. At least the corresponding characteristics appears somewhere in this spatiotemporal region. It is not easy to say this exactly because near this region the peculiarity connected with the point "b" and corresponding characteristics becomes inconspicuous on profiles. Also near this region the melting changes to recrystallization—the trajectory of a solidus transfers from going into bulk to going to surface. The turn of the solidus trajectory takes place at the instant ≈ 60 ps at the depth ≈ 90 nm. In paper [77] the processes of melting and solidification of Al in hydrodynamic approximation have been considered.

2T-HD overrates velocity of the solidus giving velocities up to few hundreds of m/s at the crystallization branch of the trajectory in the temporal range 70-200 ps. Therefore there is a rather thick mixture layer in 2T-HD. [77] Velocity of the solidus gradually decreases as the solidus tends to the vacuum surface. 2T-HD code describes gold as matter in equilibrium states. In molecular dynamics (MD) the kinetics of melting is naturally included [15]. Then liquid at the crystallization stage is significantly overcooled below equilibrium melting temperature [6]. In MD the crystallization velocity is limited by the value ≈ 100 m/s. In 2T-HD run shown in figure 40 the liquidus arrives at the surface at the instant ≈ 150 ps while the total freezing (arrival of solidus) comes at the instant ≈ 300 ps.

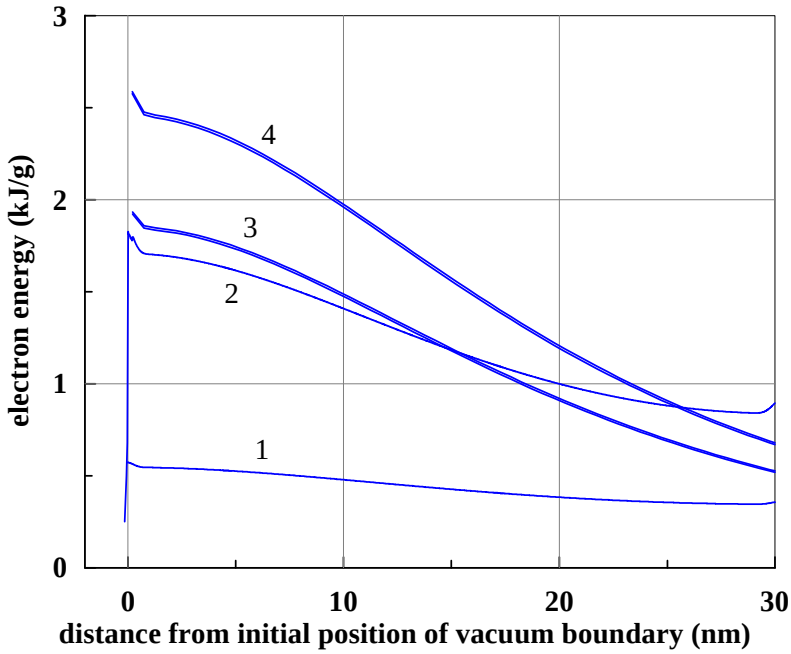

Figure 36. Profiles of electron energy $E_e(x, t = 0.1\,\text{ps})$ at time moment $t = 0.1$ ps. The curves are: (curve 1) film, $d_f = 30$ nm, $F_{\text{abs}} = 32$ mJ/cm^2, 0.55 MJ/kg, $K_\alpha = 4$; (curve 2) film, $d_f = 30$ nm, $F_{\text{abs}} = 90$ mJ/cm^2, 1.55 MJ/kg, $K_\alpha = 4$; (two curves 3) bulk target, $F_{\text{abs}} = 100$ mJ/cm^2, $K_\alpha = 1.15$ and $K_\alpha = 4$; (two curves 4) bulk target, $F_{\text{abs}} = 130$ mJ/cm^2, $K_\alpha = 1.15$ and $K_\alpha = 4$.

Why the 2T-HD run shown in figure 40 demonstrates so long "tail" with small but finite expansion velocity 10–20 m/s after the point "b" which is not the instant of arrival of a shock from nucleation because the nucleation is absent in this run? This is a result of strong heat conduction heating fast a thick layer of a bulk target, see figure 41. Fast (supersonic) heating sharply increases pressure thus creating a profile with a long "nose" going far (hundreds nm) into a bulk region, see figure 42. Namely this pressure profile with a long "nose" supports later in time the expansion velocity with a long "tail" shown in figure 40. Acoustic connection between an instant pressure profile and a velocity history is explained in [32, 78].

Model of electron heat conduction used in our 2T-HD code is presented in appendix C. The highest conduction is in the case with room temperature ions because an electron-ion collision frequency ν_{ei} is small. Coefficient of heat conduction κ quickly rises with electron temperature T_e up to the temperature T_e^* at which electron-electron collision frequency (increasing with T_e) achieves the value ν_{ei}. Ion temperature is small in the bulk of a target as it is shown in figure 41. Thus we are in the range $300 < T_e < T_e^*$ where the coefficient κ sharply rises with T_e due to partial removing of degeneracy and increasing of an electron heat capacity.

The long "tail" shown in figure 40 mimics spallation. But in the case of gold the appearance of the "tail" is a result of high heat conductivity in the low temperature region.

7. Strength of gold

Dependence of material strength to stretching as function of temperature is presented in figure 43. The circles and square are taken from molecular dynamics (MD) simulations similar to that described in paper [15]. The embedded atom method (EAM) potential for gold obtained in [79] was used in these MD simulations.

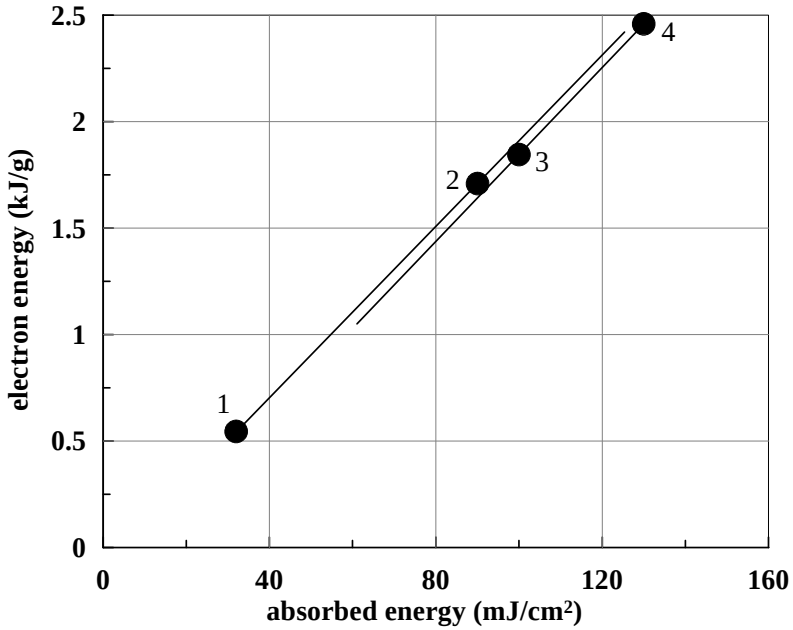

Figure 37. Electron energy $E_e(x = 2\,\mathrm{nm}, t = 0.1\,\mathrm{ps})$ at the depth 2 nm at the instant 0.1 ps taken from the dependencies in figure 36. The digits 1, 2, 3, and 4 relates to the dependencies 1 and 2 for film and 3, 4 for bulk targets from figure 36. There are pairs of very close points under the circles 3 and 4. They differ by the value of the coupling parameter.

Theory of nucleation in liquid gives expression $\tau \approx f\,\exp(A/k_BT)$, where $A = (16\pi/3)\sigma^3/p^2$, f is a pre-exponential factor, σ is surface tension, p is negative pressure, and τ is waiting time for appearance of a nucleus in a given volume. The exponential factor is equal to some value $A/k_BT = a$ at the nucleation threshold in our conditions. Then pressure is

$$p = \sqrt{\frac{16\pi/3}{a}}\,\frac{\sigma^{3/2}}{(k_B\,T)^{1/2}}. \tag{12}$$

Surface tension is $\sigma = \sigma_m\big(1-(T-T_\mathrm{m})/(T_\mathrm{cr}-T_\mathrm{m})\big)^{5/4}$, where T_m and T_cr are melting and critical temperatures, σ_m is a coefficient of surface tension in the melting point, see [80] and references given in this paper. The factor a defines relative depth of a metastable well. Smaller values of a corresponds to a weaker barrier fastening a system from decay into vapor-liquid mixture.

We know [80] that the EAM potential of gold from [79] has $\sigma_m = 540$ dyn/cm. Approximations of the MD data by expression (12) are shown in figure 43. We suppose that the parameter a weakly depends on temperature and neglect this dependence. Value a is defined by the pre-exponential factor which depends on the deformation rate. For small deformation rates the value a is large and nucleation pressures are small. The value a decreases as the deformation rate increases. In our conditions with extremely fast deformations the parameter a decreases down to the values $a \approx 15$, see figure 43.

Real gold has the surface tension coefficient $\sigma_m \approx 1000$ dyn/cm [80]. We suppose that the parameter a depends mainly on the deformation rate which is dictated by the ultrafast experiments. Therefore we use the same value $a = 15$ as was chosen in figure 43 for the description of the MD results for liquid. This means that the parameter a is approximately the same for substances with different values of σ if the deformation rate is the same. Then we obtain the curve $\sigma = 1000$ dyn/cm, $a = 15$ in figure 43 which approximately describes strength of real gold.

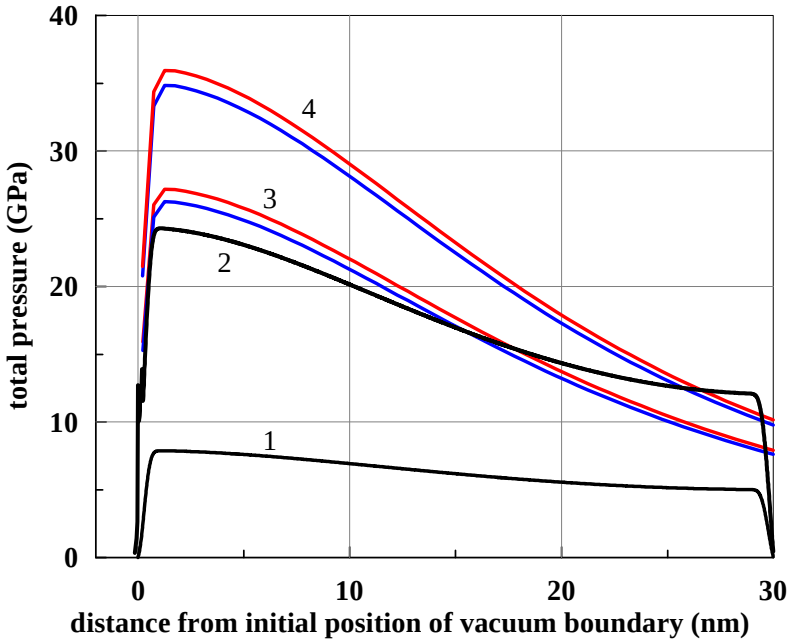

Figure 38. Pressure profiles for the instant 0.1 just after finishing of energy pumping of electron subsystem. The curves are: (curve 1) film, $d_f = 30$ nm, $F_{\rm abs} = 32$ mJ/cm^2, 0.55 MJ/kg, $K_\alpha = 4$; (curve 2) film, $d_f = 30$ nm, $F_{\rm abs} = 90$ mJ/cm^2, 1.55 MJ/kg, $K_\alpha = 4$; (curve 3, red) bulk target, $F_{\rm abs} = 100$ mJ/cm^2, $K_\alpha = 1.15$; (curve 3, blue) bulk target, $F_{\rm abs} = 100$ mJ/cm^2, $K_\alpha = 4$; (curve 4, red) bulk target, $F_{\rm abs} = 130$ mJ/cm^2, $K_\alpha = 1.15$; (curve 4, blue) bulk target, $F_{\rm abs} = 130$ mJ/cm^2, $K_\alpha = 4$. We see that now (comp. with figures 35 and 36) the pairs of the curves 3 and 4 are obviously separated. Indeed, the faster e-i coupling faster increases ion pressure in the sum $p = p_i + p_e$ while electron pressure depending on electron temperature remains approximately the same according to figure 35.

Pressure–temperature profiles for the instants $t = 30$ and 70 ps are imposed onto the phase diagram in figures 44 and 45. We take the pressure profiles from the run with parameters $F_{\rm abs} = 100$ mJ/cm^2, $K_\alpha = 4$. The profiles for this run are shown also in figures 41 and 42.

Let us estimate a "distance" between the stretching achieved in 2T-HD run in figures 44 and 45 and the nucleation thresholds from figure 43. The strengths of solid and liquid states differ very significantly, compare the circles and the square in figure 43. The 2T-HD overestimates thickness of a solid–liquid mixture layer at the stages following the 2T stage [13]. Therefore in figures 44 and 45 the part of the parametric curve $p(x, t = \text{fix})$, $T(x, t = \text{fix})$ (the parameter x runs the curve) follows the melting curve. In MD runs the solid–liquid layer is thick at the 2T stage and after that it sharply becomes thinner [13]. The run shown in figures 44 and 45 passes near the MD thresholds for molten gold. But if we will wait for the crossing of the "real strength" curve then energy pumped by a pump pulse should be significantly higher than that corresponding to the run presented in figures 41, 42 and 44, 45. In figure 43 the "real strength" curve is given by the parameters: surface tension $\sigma = 1000$ dyn/cm and the non-dimensional barrier against thermal fluctuations is $a = 15$.

Again, the strengths of solid and liquid states differ very significantly. In molten gold the strength decreases as temperature increases. Especially appreciable is the change with temperature near the melting curve. Increasing energy $F_{\rm abs}$ (or/and the e-i coupling) we increase an amplitude of tensile stress but also increase temperature of a molten state thus doing matter mechanically weaker. It is significant to go out from the strip near the melting curve. It may

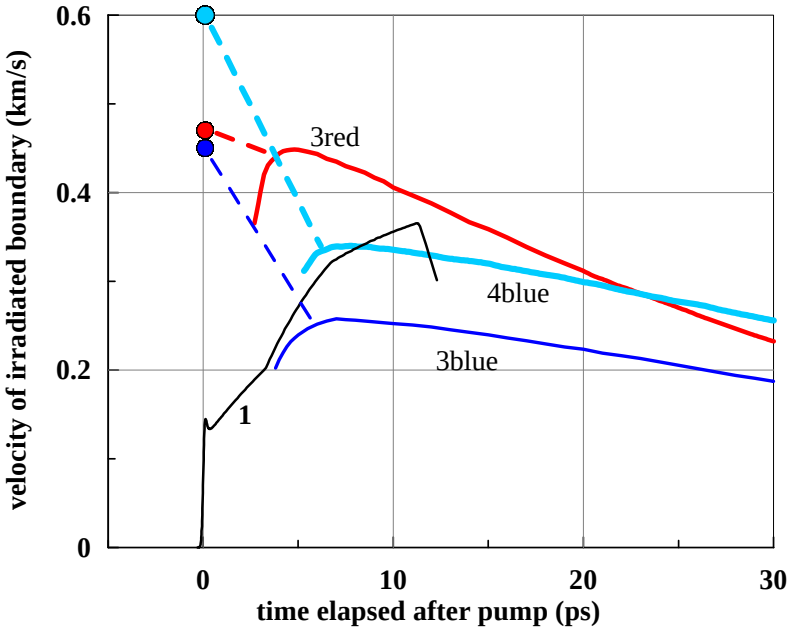

Figure 39. Velocity trajectories for the cases: (curve 1) film, $d_f = 30$ nm, $F_{\text{abs}} = 32$ mJ/cm^2, weak coupling $K_\alpha = 4$; (curve 3red) bulk target, $F_{\text{abs}} = 100$ mJ/cm^2, strong coupling $K_\alpha = 1.15$; (curve 3blue) bulk target, $F_{\text{abs}} = 100$ mJ/cm^2, weak coupling; (curve 4blue) bulk target, $F_{\text{abs}} = 130$ mJ/cm^2, weak coupling.

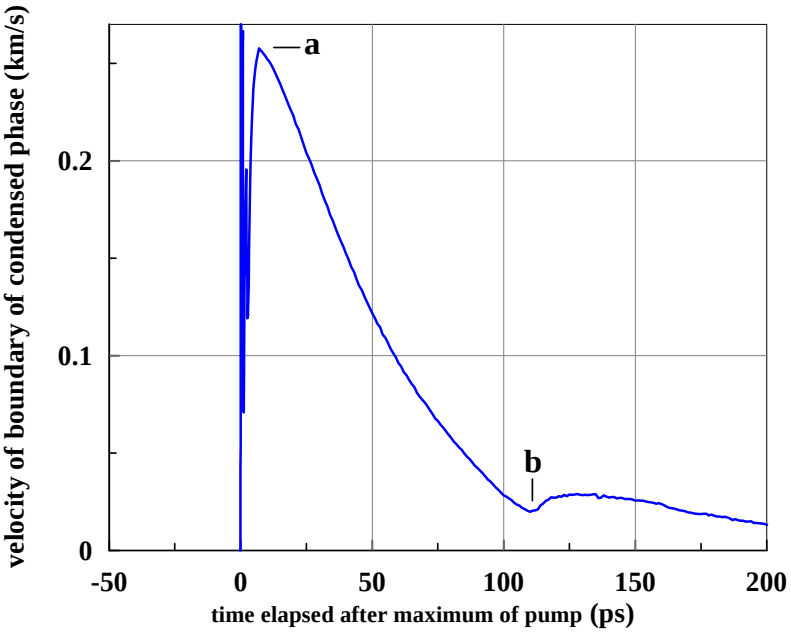

Figure 40. Kinematics of surface at the middle stage. This is the continuation of the curve "3blue" from figure 39. This is the case with $F_{\text{abs}} = 100$ mJ/cm^2 and rather weak coupling $K_\alpha = 4$.

be supposed that at the ablation/nucleation threshold the state where nucleation begins in real conditions has negative pressure approximately -6 GPa and temperature approximately

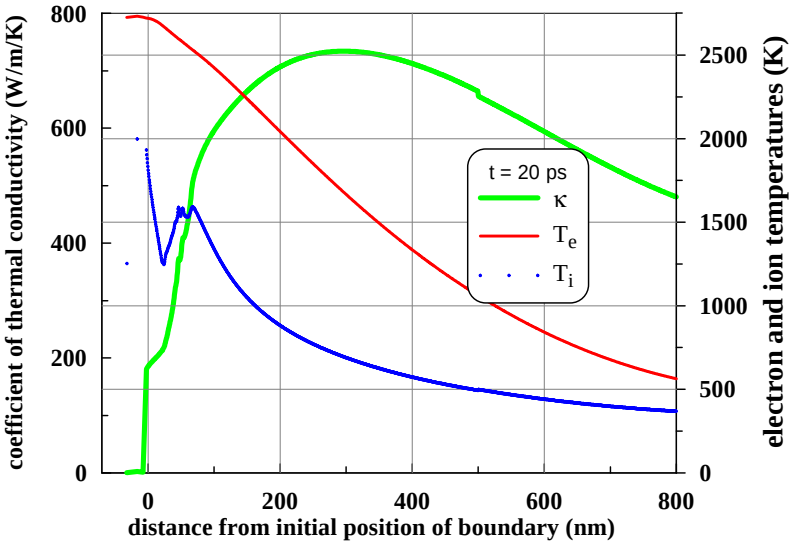

Figure 41. Even rather late in time relative to the 2T stage the electron heat conduction remains high enough to heat many hundreds of nanometers of gold. This is the run $F_{\rm abs} = 100$ mJ/cm^2, $K_\alpha = 4$, see also figure 40. Heat conductivity model is described in appendix C.

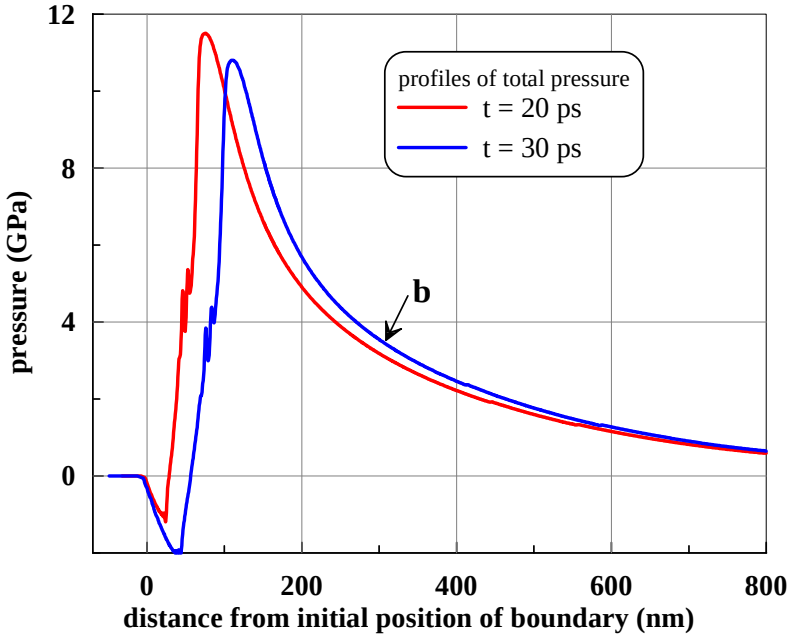

Figure 42. Very long "nose" penetrating deep into target is created thanks to high conductivity. The point marked "b" corresponds to the instant (30 ps) position of the characteristics which runs to the left side (in direction to the vacuum boundary). This characteristics arrives at the vacuum boundary at the instant marked "b" in figure 40.

1700 K (see figure 43); there is $\approx 10\%$ difference between the nucleation and ablation thresholds [6, 81, 82]; the nucleation threshold is lower; there are frozen nanobubbles in the range between the nucleation and ablation thresholds.

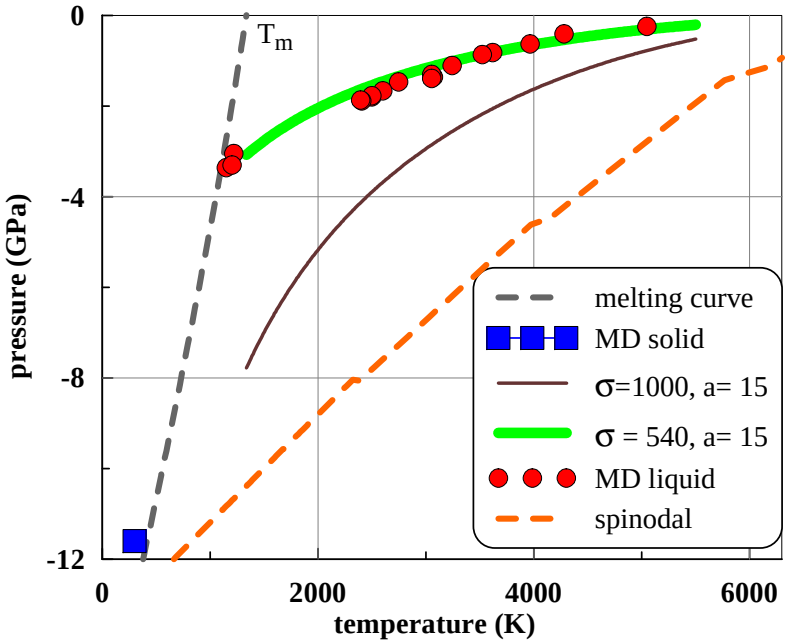

Figure 43. Threshold for nucleation in stretched gold at the deformation rate $\sim 10^9$ s^{-1} corresponding to our conditions of illumination by an ultrashort laser pulse. The circles relate to liquid, while the square–to solid. Values σ are in dyn/cm. Melting curve and spinodal are taken from equation of state [19, 20], see appendix A. Values $p < 0$ give amplitudes of tensile stress in the point of nucleation just before the event of nucleation. The thresholds are extracted from results of many MD simulations. The curves are calculated according to expression (12) with $T_m = 1337$ K and $T_{\rm cr} = 7700$ K.

8. Deceleration at the middle stage

It is remarkable that our pump-probe experiment (section 2) reliably indicates that the reflecting surface decelerates. The reflecting surface is a boundary with vacuum. This follows from density profiles. Thus we see from experiment that indeed the nanoscale thick surface layers of gold strongly resists to the expansion stretching. Corresponding decelerations are of the order of $g \sim 10^{14}$–10^{15} cm/s^2. This is huge value comparable with a free fall acceleration at a surface of a neutron star. Typical pressure differences causing such deceleration are $\rho g h \sim 1$–10 GPa for densities 15–19 g/cc and $h \sim 100$ nm.

Phase differences between the current and initial (prior to pump) phases $\Delta\varphi(t) = \varphi(t) - \varphi(t = -\infty)$ are presented in figure 46. This is the phase φ of the reflected electromagnetic wave used for probing of a surface state. The phase φ may be measured in radians $\varphi_{\rm rad}$ or in nanometers $\varphi_{\rm nm}$ according to expression

$$\varphi_{\rm nm} = \lambda_{\rm probe} \frac{\varphi_{\rm nm}}{4\,\pi},$$

where $\lambda_{\rm probe}$ is wavelength of a probe pulse. In our experiments the probing wavelength is the second harmonics of Cr:forsterite laser with the first harmonics 1240 nm (1 eV) and the second one 620 nm (2 eV).

There are two contributions into the phase shift $\Delta\varphi$. One of them is connected with variation of optical parameters under heating of electron and ion subsystems, while the another one is caused by the geometrical shift of a reflecting surface. It is important that the phase $\varphi_{\rm liq}$ of molten gold not far from melting temperature is approximately the same as the phase $\varphi_{\rm sol}$ of solid gold at room temperature (the difference is few nm).

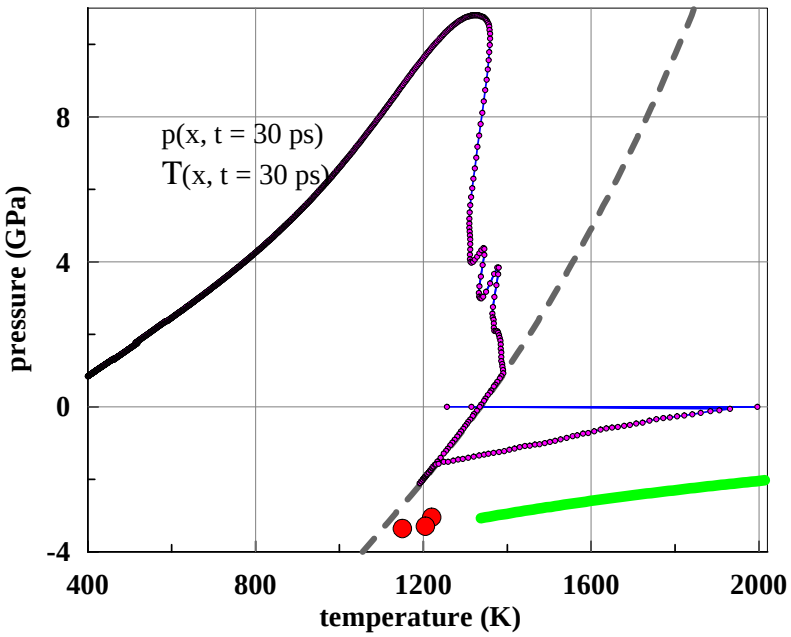

Figure 44. Instant pressure–temperature profile near the moment of time corresponding to the maximum stretching. The red circles, green curve, and melting grey dashed curve are the same as in figure 43. The instant 2T-HD profile is shown by the curve with the small circles on it. This is the run with parameters $F_{\rm abs} = 100$ mJ/cm^2, $K_\alpha = 4$. It is shown in figures 41 and 42. The small circles correspond to the Lagrangian steps (or points) in the finite-difference scheme. There are two evaporated points belonging to the zero pressure level $p = 0$.

Therefore after finishing of the 2T stage the shift $\Delta\varphi$ returns back to the values near the zero value. At the 2T stage with enhanced metallicity and dissipation the shift $\Delta\varphi$ deviates to the side directed along the geometrical shift, see figure 46. This is why the minimums appear on the dependencies $\Delta\varphi(t)$. The amplitudes of the phase "jump" during duration ~ 0.1 ps of an ultrashort pump pulse are 10–15 nm, see figures 47 and 48.

The minimums in the dependencies $\Delta\varphi(t)$ appear as a result of the two circumstance. Firstly, the amplitudes of the jumps (10–15 nm) are larger than the difference in phases (few nm) between solid and liquid gold. Secondly, the geometrical shifts of a boundary during a 2T stage (10–20 ps) are also of the order of few nanometers for our range of fluences. The minimums approximately divide the 2T and 1T stages. The excess of excitation takes off near the minimum when electron temperature T_e decreases from 15–25 kK to 2–5 kK, see figures 21 and 22.

After the minimum the phase shift is approximately equal to the geometrical shift of a boundary, because the phase shift (few nm) between solid and liquid becomes small in comparison with the geometrical shift. Deceleration of a boundary is well seen after the minimum in figure 46. The portions 21–22 and 31–32 of the curves in figure 46 demonstrate clear and significant decelerations. The reflecting surface loses main part of its velocity during the first deceleration stage lasting ≈ 100 ps, see figure 40; we say here about the first deceleration stage because experimental data indicate existence of the second very long lasting stage of deceleration; we will return to this question below, here we have to pay attention to the peculiarity of the function $\Delta\varphi(t)$ at $t \sim 100$ ps.

The peculiarity 32–33 in figure 46 is connected with beginning of freezing of gold near the vacuum boundary. Solid has slightly different reflection phase relative to liquid. Therefore freezing causes changes in the reflection phase. Interesting but the experimental data also have

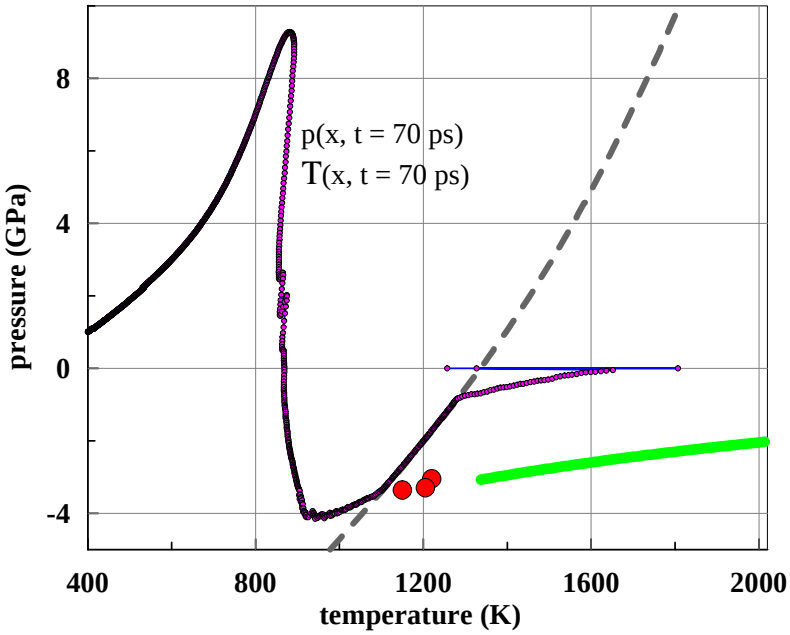

Figure 45. The same profile as in figure 44 but now for the later instant 70 ps. This instant is after the instant when the maximum (in time evolution) tensile stress p_{xt*} is achieved. After that the maximum in space stress p_{x*} at the current instant profile is approximately equal to the value p_{xt*}. The value p_{x*} slowly decreases on a long time interval.

the peculiarity at the same temporal range $t \sim 100$ ps, see figure 49 where these places are emphasized by the pairs of the filled circles.

It is plausible that these experimental peculiarities say about freezing of surface of gold. Indeed, another explanation connects these peculiarities with arrival of spallation shock at the vacuum boundary. But there are the two objections against this explanation. The peculiarity in figure 49 is present also in the case $F/F_a = 0.8$ below the ablation threshold F_a. The another objection is the following. The spallation shock causes a peculiarity in the temporal velocity history $u(t)$ of a surface. It is similar to the point "b" in figure 40. This peculiarity is appreciable only in the high quality velocity trajectory $u(t)$. It is almost invisible at the geometrical shift trajectory.

Indeed, the point "b" from figure 40 corresponds to the instant 110 ps. While the instant of the jump 32–33 in figure 49 is 135 ps, it is later. Inspecting the theoretical trajectory of a geometrical shift in figure 49 at the instants 110 and 135 ps we see how weak is the inflection at the point 110 ps relative to the jump 32–33; passing the minimum of velocity causes the inflection of the geometrical shift.

If we accept that the pairs of circles in figure 49 mark freezing, then question about how the freezing time depends on absorbed energy, heat conduction, and e-i coupling should be additionally investigated because energies changes approximately twice while the position of the "freezing" interval remains unchanged.

Figure 50 demonstrates the important fact. It indicates that the deceleration continues at the rather late subnanosecond stage. The position of the vacuum boundary is 136 nm at the instant 500 ps when the last probe pulse has been sent. Height of cupola is approximately equal to the depth of crater (the crater for smaller fluence is shown in figure 1). Therefore the two-phase medium under cupola is still rather dense. Such medium causes deceleration of a cupola shell [6].

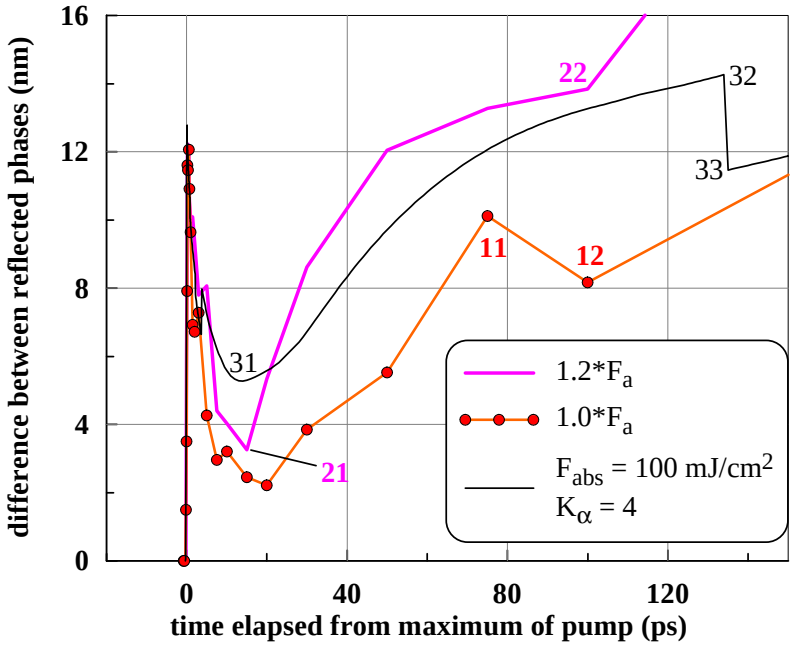

Figure 46. End of the 2T stage and transition to 1T stage at the time range 15–20 ps. The minimums 31, 21 of the curves 11–12, 21–22, and 31–32–33 correspond to transition 2T→1T. There are the portions 21–22, 31–32 of the curves with expressed deceleration. Another important peculiarity 31–32 is connected with beginning of freezing at the theoretical curve 31–32–33. It may well be that the bends 11–12 and 22 at the experimental curves also are connected with freezing. They are located in the time interval where freezing should begins.

9. Comparison with experimental data. Early stages

Let us additionally analyze experimental data described in sections 2 and 8. Comparison of experiment and 2T-HD runs are presented in figures 51 and 52. We are interested in analyzing of the indications of melting during the 2T stage which exist in the pump-probe data. These indications are connected with the kinks in the temporal dependencies of the experimentally measured optical parameters. They are marked by the filled circles in figure 47. The kinks slow down decrease of a phase shift with time.

There are obvious traces of melting in the temporal histories of optical parameters obtained thanks to 2T-HD simulation. They looks like jumps in the temporal dependencies, see figures 51 and 52. This is a consequence of our approximations used in physical model for the 2T-HD code. We write different expressions for the dielectric functions of 2T solid and liquid gold. The transition between these functions is made sharp: as skin averaged ion temperature overcomes the melting temperature, we transit from the dielectric function for solid to the dielectric function for liquid.

Therefore in this model the transition becomes fast. Of course, in reality we have to include description of kinetics of melting and develop a model for optical properties of the 2T solid–liquid mixture. But this is a problem for future hard work. Here we want to attract attention to the experimental and computational results relating to the melting under conditions of electron-ion non-equilibrium. In experiments and simulations the 2T stage is clearly separated from preceding and subsequent 1T stages. There is a jump lasting during the very short pump duration and after that the decay along 10–20 ps. The decay is well seen especially in the phase dependence on time. Experimental dependencies of the phase shift on time are important to find the end of the 2T stage. As was said it is very significant that the phase shift becomes small at the end

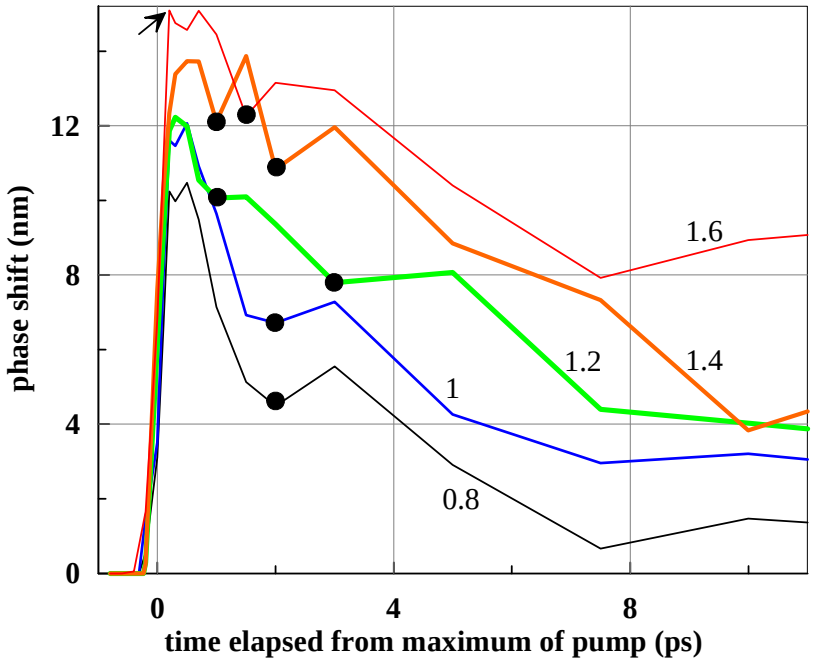

Figure 47. Amplitudes and positions of the "jump" of the phase shifts during excitation of conduction electrons by a femtosecond pump pulse. The arrow marks the amplitude and the temporal position of the "jump" for the highest excitation level $F/F_a = 1.6$, where F_a is an ablation threshold. The digits near the curves give corresponding values of normalized fluence F/F_a. The circles are putted in the peculiar points. Variation of a phase in these points may be caused by 2T melting. In section 9 we compare positions and phases of these points with theoretical data about 2T melting.

of a 2T stage. This is a consequence of the fact that for gold the absolute values of phase of reflected wave are approximately equal for 1T solid and 1T liquid.

While the end of the 2T stage is weakly distinguishable at the temporal dependencies of a reflection coefficient. Let us mention in this connection that there is additional decrease of reflection in the experimental cases with enhanced fluence at the late (subnanosecond) stage, see figure 53. May be this a result of growing of surface perturbations increasing scattering and plasmon absorption.

Comparison of the experimental indications of the 2T melting with theory is continued in figures 54 and 55. Figure 54 is necessary to explain appearance of the computational points in figure 55. In figure 55 the computational instants of the melting jumps in figure 54 are plotted as two separate plots. One of them (the blue curve) corresponds to the case with weak e-i coupling $K_\alpha = 4$ (see appendix B). While the second case (the red curve) is the case of enhanced e-i coupling $K_\alpha = 1.15$.

We see that increase of imputed energy weaker influence decrease of life of solid state after arrival of a pump pulse than the increase of the e-i coupling.

10. Conclusion

Results of very important pump-probe experiments on bulk gold targets and analysis of them are presented. Let us remember that a series of ambitious publication [29–31, 33–37] using the modern experimental techniques were devoted to investigation of the two-temperature state of gold. These works employ a thin (30 nm) film and concentrate attention on the first 5–6 ps.

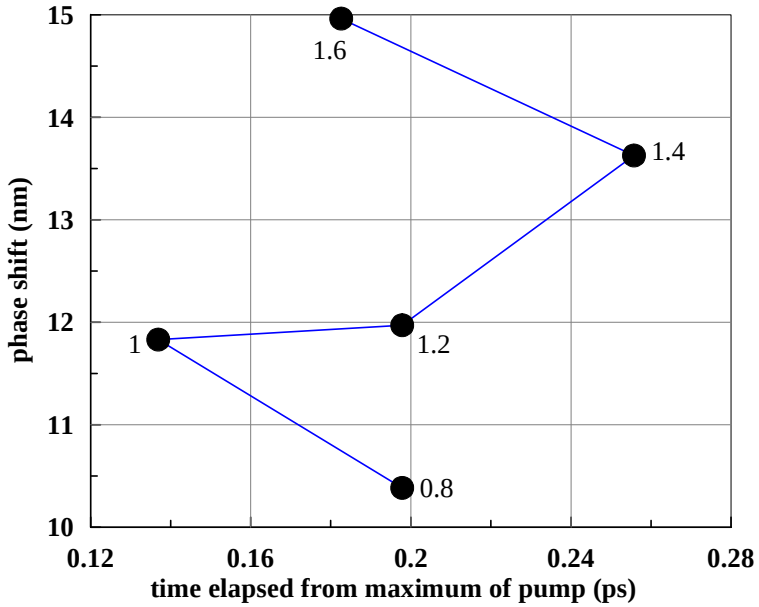

Figure 48. Positions in time and amplitudes of the points in the tips of the jumps connected with ultrafast heating. Example of such point is marked by an arrow in figure 47. The digits near the curves give corresponding values of normalized fluence F/F_a. We see that duration of the jump is of the order of duration of a pump pulse. We see also that the amplitude of the jump is significantly larger than the amplitude difference between the solid and liquid states.

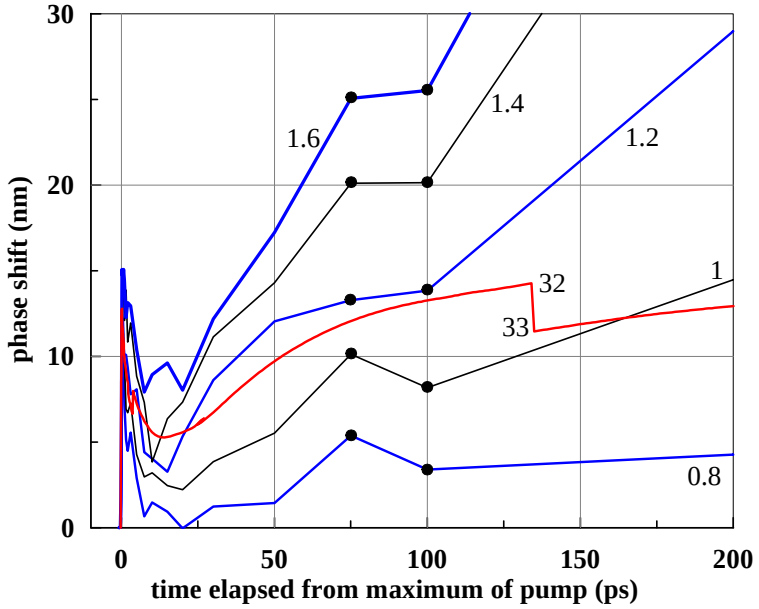

Figure 49. Temporal behavior of the phase shifts in experiments (the curves 0.8, 1, ...) and in 2T-HD simulation (the curve 32–33); the curves 0.8, 1,. are marked by the corresponding values of the normalized fluence F/F_a, the simulation run has been performed with $F_{\rm abs} = 100$ mJ/cm^2, $K_\alpha = 4$. The theoretical peculiarity 32–33 is due to freezing. The experimental peculiarities are marked by the pairs of filled circles. It may be supposed that they also are thanks to freezing.

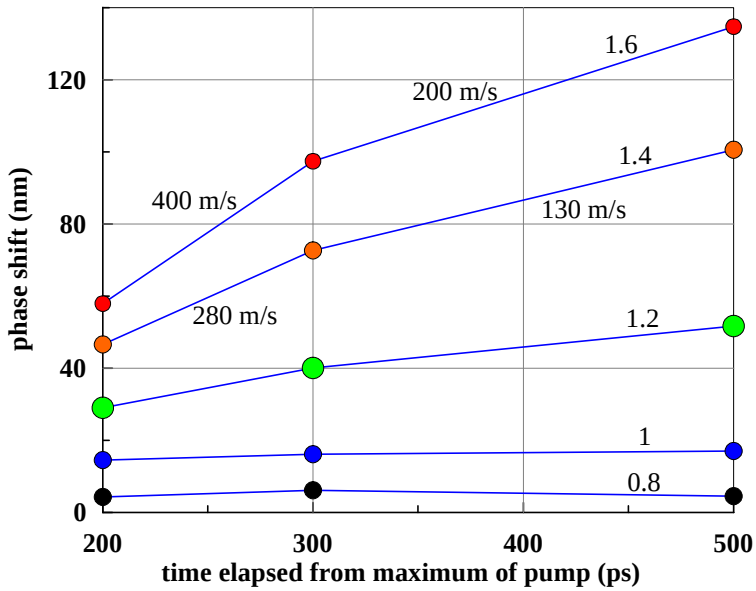

Figure 50. Late stage deceleration according to pump-probe measurements. The digits give normalized fluence F/F_a. There are three experimental points covering the temporal range from 200 to 500 ps. Expansion velocities found from the spatiotemporal positions of the filled circles are given for the upper two curves.

In this work, we have considered the early (few picoseconds) stage, as in the cited above papers, but we add to consideration analysis of a transition stage from two-temperature to one-temperature states. We define the end of the two-temperature stage experimentally and in simulations. We consider the two-temperature melting phenomena during the first few picoseconds. We define influence of electron-ion coupling parameter on the duration of life of solid reflecting skin layer. Data about dielectric permittivity of two-temperature gold are obtained.

The middle stage lasting 50–150 ps has been considered also. New explanation connecting the peculiarities in the phase shift at this stage is presented. May be future work allows to define the freezing stage when surface of a target solidifies, changes its optical parameters, and begins to reflect probing wave with different phase shift.

Long lasting decay of the expansion velocity is noticed. It is explained by high conductivity of gold on the 2T stage and at the stage intermediate between the 2T and 1T stages. Thanks to this conductivity sudden rise of pressure takes place at a large depth (few hundred nm) under illuminated surface. Namely this rise at the initial stages supports low velocity expansion of vacuum boundary at late times (100–200 ps and longer).

Deceleration of vacuum boundary is reliably experimentally detected. During this deceleration a surface illuminated by the near ablation threshold pulse loses almost all its initial velocity.

Acknowledgments

This work was financially supported by grants from the Russian Science Foundation No. 14-50-00124 (S I Ashitkov, P S Komarov, A A Yurkevich and M B Agranat, in part of experiments) and 14-19-01599 (V V Zhakhovsky, Yu V Petrov, V A Khokhlov, D K Ilnitsky and N A Inogamov, in part of theoretical calculations).

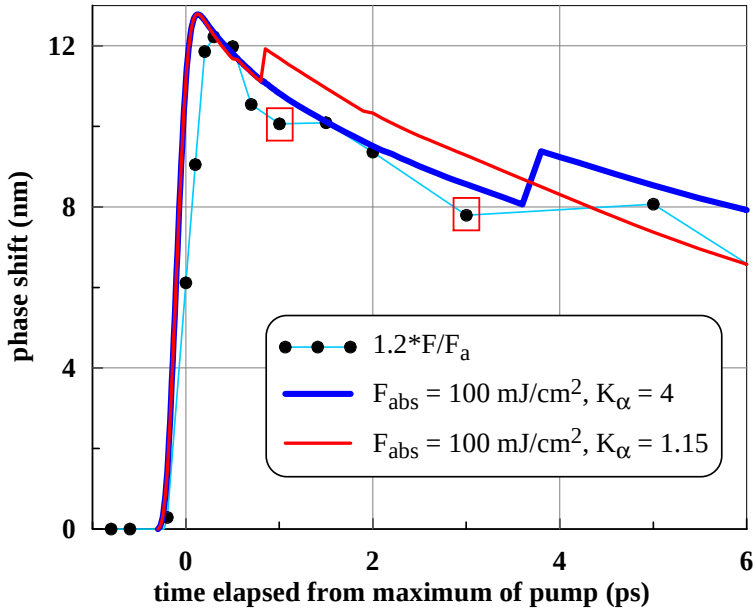

Figure 51. Traces of melting seems are present in the pump-probe early stage data in figure 47. This is unusual melting going in the conditions with excited electrons. Gold melts as a result of energy transfer per unit of volume (not a thermal conduction flux of heat from one place to another) thanks to e-i coupling. The traces of melting in figure 47 are marked by the filled circles. Here we compare the case $1.2F/F_a$ from figure 47 with the 2T-HD runs where we know when liquid appears. Corresponding two traces from figure 47 are taken into squares. Melting leads to the well seen change of phase in 2T-HD runs. In the case with faster e-i coupling (the run $K_\alpha = 1.15$) melting begins earlier.

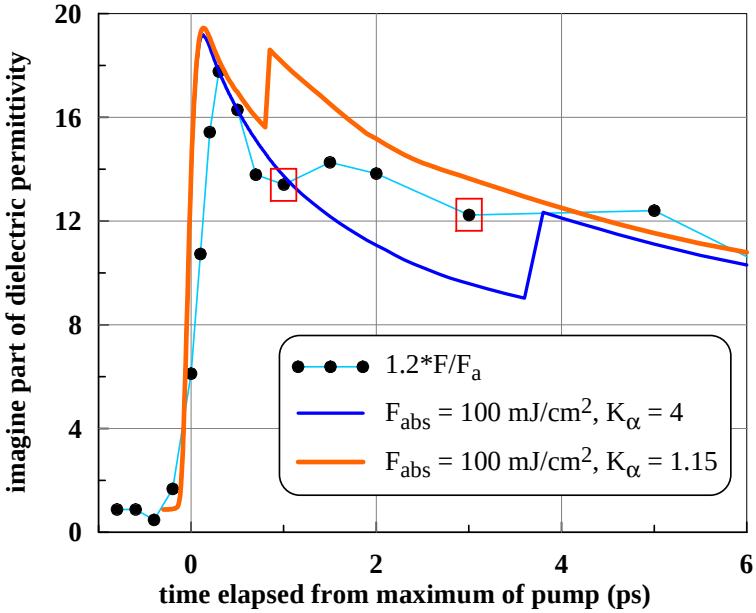

Figure 52. Melting even better is seen in the temporal history $e_2(t)$ of the imagine part of dielectric function.

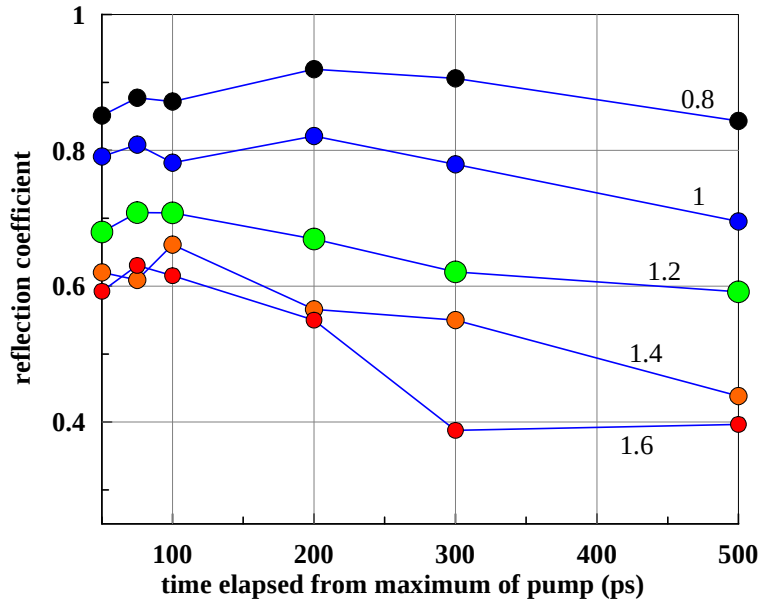

Figure 53. Decrease of reflection at the late stage in the cases 1.4 and 1.6 corresponding to enhanced fluences. This is a result of the pump-probe measurements. The digits give normalized fluence F/F_a, where F_a is an ablation threshold.

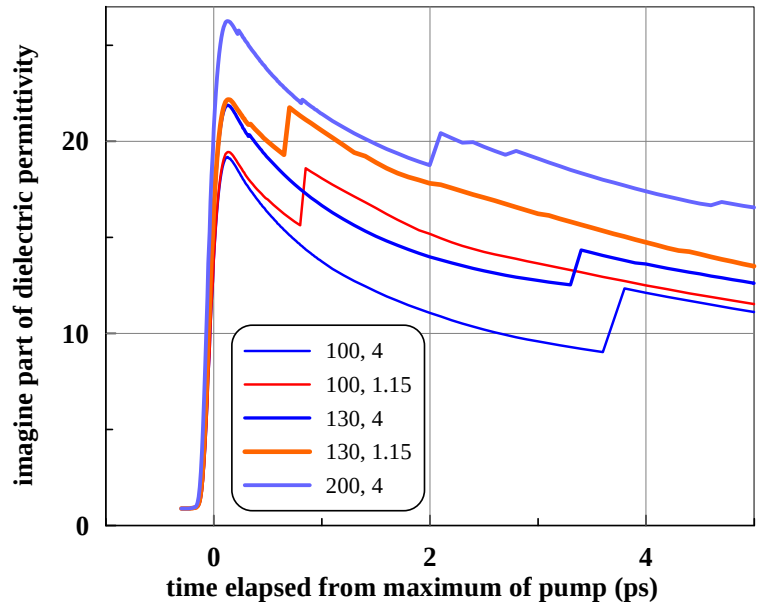

Figure 54. The melting jumps at the computed temporal dependencies of imagine permittivity for the runs with different absorbed energy F_{abs} and different e-i coupling parameter. The curves are marked by the value of F_{abs} (the first digit) and the value of parameter K_α (the second digit). The parameter K_α defines a rate of e-i energy transfer, see appendix B. The larger K_α corresponds to weaker coupling. We see that at the fixed coupling the life time of solid after ultrashort illumination slowly decreases as energy F_{abs} increases.

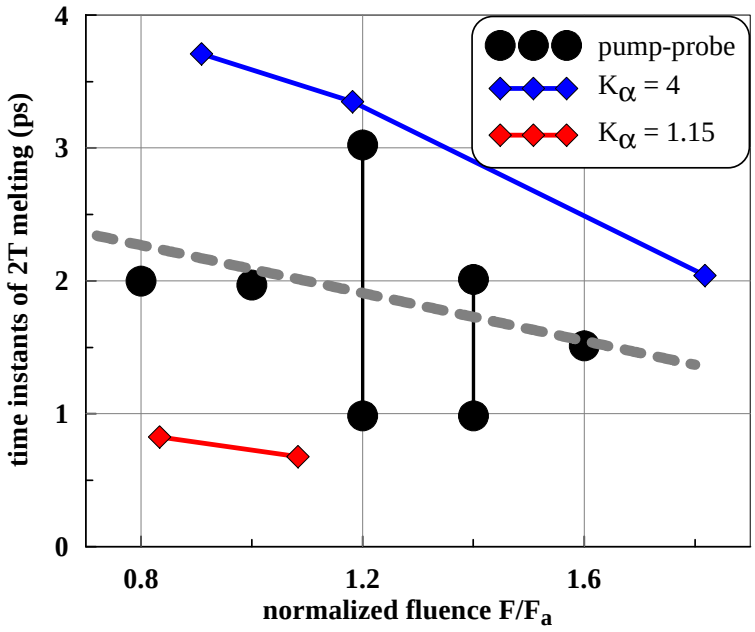

Figure 55. Waiting time t_m for melting of the reflection skin layer as a function of imputed energy. The blue and red dependencies come from figure 54. They give dependencies $t_m(F, K_\alpha)$ on fluence F for $K_\alpha = 4$ (the blue curve) and for $K_\alpha = 1.15$ (the red curve). For the stronger e-i coupling the time t_m is shorter. Therefore the red curve is under the blue curve. Energies $F_{\rm abs}$ were normalized: $F_{\rm abs}/F_{\rm abs}|_{\rm abl}$, where $F_{\rm abs}|_{\rm abl}$ is an ablation threshold taken to be 110 mJ/cm^2. The horizontal axis gives values of the normalized fluences $F_{\rm abs}/F_{\rm abs}|_{\rm abl}$ for the 2T-HD results and values F/F_a for the pump-probe results. The black filled circles of the pump-probe results are taken from figure 47 where they mark the kink-like indications of melting. For the cases $F/F_a = 1.2$ and 1.4 there are two pairs of such indications in figure 47. Here these pairs are connected by the two vertical straight intervals. The grey dashed straight line follows the decrease of t_m according to the experimental black filled circles.

Appendix A. Equation-of-state

2T equation-of-state (EoS) is composed from a sum of ion and electron free energies $F(\rho, T_e, T_i) = F_i(\rho, T_i) + F_e(\rho, T_e)$ as it is explained in [21, 23, 49, 50]. Of course, this is an approximation neglecting influence of T_e on F_i and T_i on F_e. For the F_i we take the wide range EoS of gold [19, 20]. For the F_e we use results from the DFT simulations presented in an analytical form in [23]. Figure A1 demonstrates how electron energy $E_e(\rho, T_e)$ depends on relative density $x = \rho/\rho_0$, $\rho_0 = 19.3$ g/cm^3, and electron temperature. Electron component of pressure is given in figure A2.

Appendix B. Coupling parameter

There are two theoretical approaches to calculations of the electron-ion energy coupling. One of them disregards differences between s,p and d bands of gold, while the another treats these bands separately [22, 83, 84]. The second approach [22, 84] gives smaller values of a coupling parameter $\alpha(T_e)$ at elevated temperatures $T_e > 4$ kK. We approximate these functions as

$$\alpha(\rho, T_e) = \left(0.2 + \frac{4.3}{K_\alpha}\,\frac{T_{\rm eV}^{3.6}}{1 + T_{\rm eV}^{3.5} + 0.9T_{\rm eV}^{4.1}}\right)\left(\frac{\rho}{\rho_0}\right)^{5/3} \times 10^{17}\ {\rm W\,K^{-1}m^{-3}}. \qquad \text{(B.1)}$$

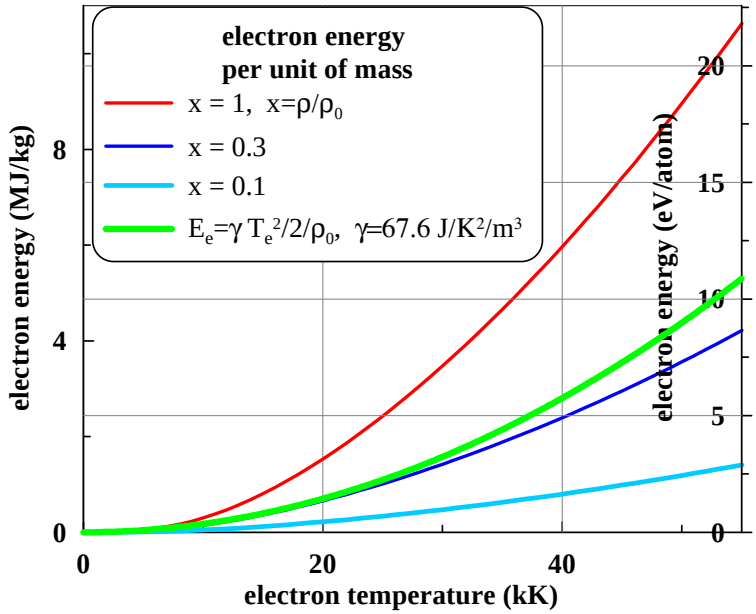

Figure A1. Electron energy dependences on density and T_e. Expression $\gamma T_e^2/2\rho_0$ valid at low temperatures is also shown for comparison.

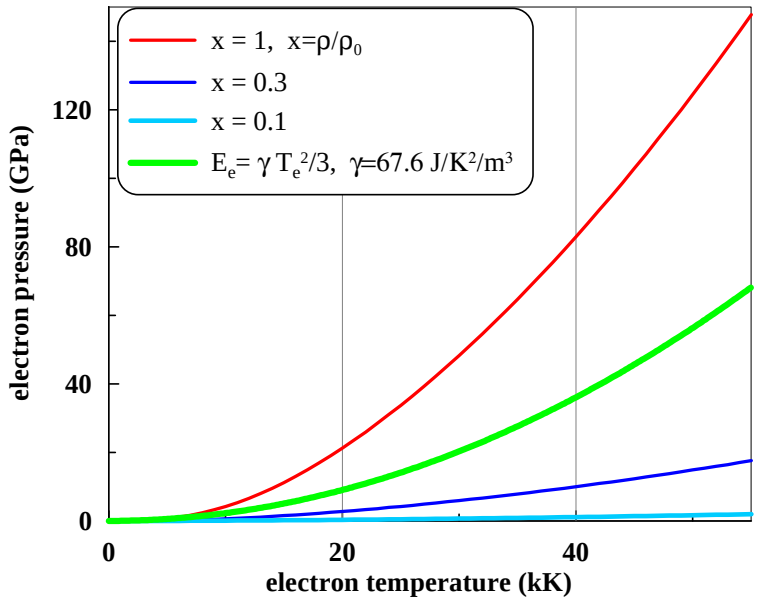

Figure A2. Electron pressure. Expression $\gamma T_e^2/3$ is valid at low temperatures.

Here electron temperature $T_{\rm eV}$ is given in eV, K_α is a parameter defining the "height" of the function (B.1) in its high temperature part. Two cases shown in figure B1 correspond to K_α equal to 4 (the lower curve) and 1.15 (the higher curve). At low temperatures T_e the function (B.1) begins from the experimentally confirmed value 0.2×10^{17} W K^{-1}m^{-3} [27]. Figure B1 presents these dependencies. It is important that at small temperatures T_e our calculations [22] begin from the experimentally measured value [27] without any adjustment.

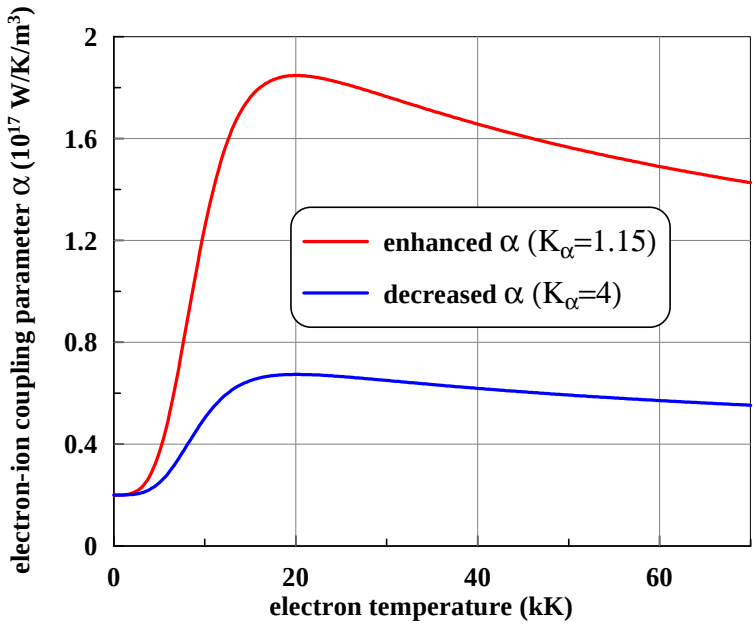

Figure B1. Dependence of coupling parameter α on electron temperature according to approximation (B.1) used in our two type 2T-HD simulations with fast (the upper curve) and slow (the lower curve) electron-ion energy transfer.

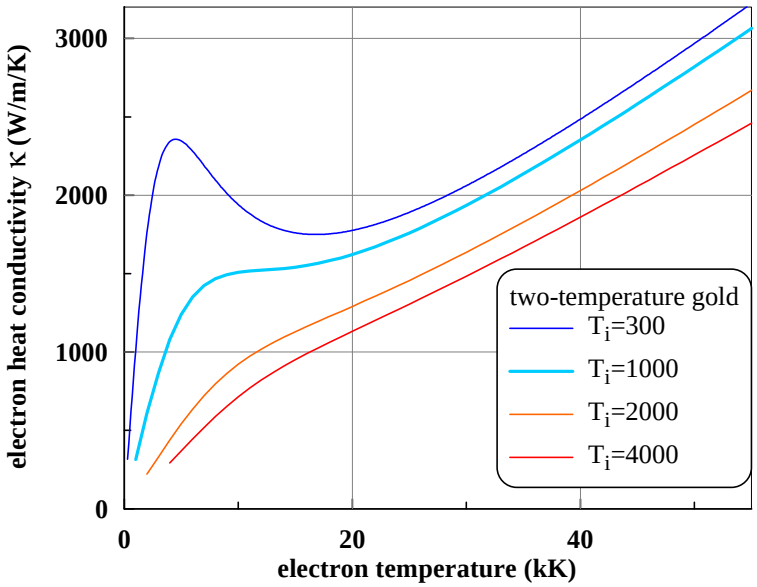

Figure C1. Variation of a 2T heat conduction coefficient $\kappa(\rho, T_e, T_i)$ with temperatures T_e and T_i in isochorically heated solid density ρ_0 gold.

Appendix C. Electron heat conduction

Difficult problems are connected with calculations of a 2T electron heat conduction coefficient $\kappa(\rho, T_e, T_i)$. In 2T-HD simulations presented here, we use data from [22, 84–86]. Corresponding functions $\kappa(\rho, T_e, T_i)$ are shown in figure C1.

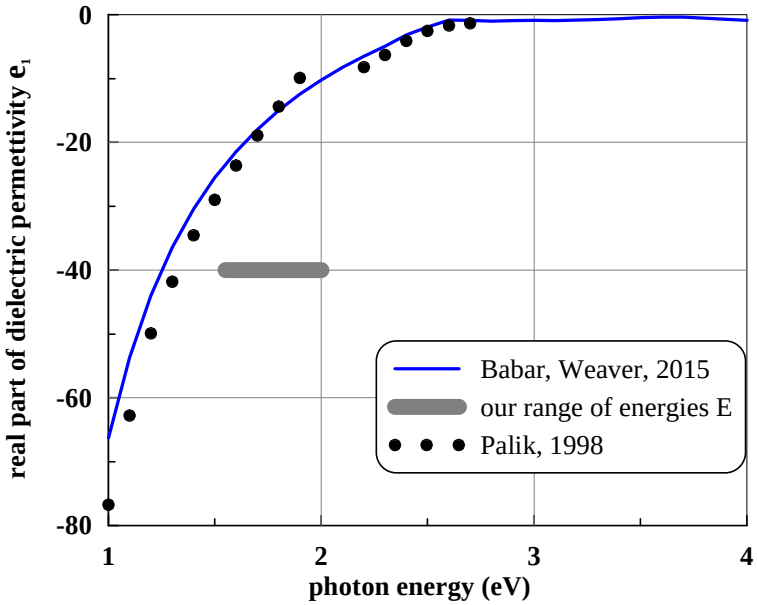

Figure D1. Absolute value of $e_1(E)$ decreases with increase of photon energy E. This is combined effect of approaching to plasma frequency ≈ 9 eV for gold and approaching to the d-band of $5d^{10}\ 6s^1$ Au. Plasma frequency defines behavior of conduction 6s electrons. It influences the function $e_1(E)$ beginning from the small values of photon energies. While the d-band contribution becomes more important when energy E is nearing from the left side to the upper edge $E \approx 2.5$ eV of the d-band. The horizontal straight interval shows the range between the first harmonics of Ti:sapp laser ($\approx$ 800 nm) and the second harmonics of Cr:forsterite laser ($\approx$ 620 nm) both used for probing of 2T gold in the pump-probe experiments.

Appendix D. Dielectric permittivity

Optical characteristics of noble metals such as gold in visible range differ from those of simple metals such as aluminum because of the significant influence not only the conduction electrons as in simple metals but electrons of inner bands onto the optical properties. While in aluminum the inner band is separated from the conduction band by the large energy gap of about 70 eV, in gold a band of inner d-electrons lies inside the conduction band and its top is not so far from the unfilled states in the conduction band. Therefore the dielectric permittivity of gold is due to not only the intraband transitions of conduction electrons but also electron interband transfer. From the classical point of view it means that besides the Drude term, responsible for the polarizability of conduction electrons, polarizability of inner electrons is important in noble metals. This polarizability can be described in a model of Lorentz oscillators for inner electrons [26]. For the d-band metal gold we limit the number of oscillators to only one of them. Theoretical dielectric permittivity is a sum of a Drude term e_D and a Lorentz oscillator e_L:

$$e = e_{\rm D} + e_{\rm L}, \quad e_{\rm D} = e_{1\rm D} + {\rm i}e_{2\rm D}, \quad e_{\rm L} = e_{1\rm L} + {\rm i}e_{2\rm L}. \tag{D.1}$$

Appendix D.1. One-temperature situation

Knowledge about optical characteristics is necessary to understand the reflectivity measurements of pump-probe experiments with an optical probe. Well-known data from the Palik's reference manual [87] are presented in figure D1. Recently these data have been corrected by Babar and Weaver [18]. From figure D1 we see that even in the very well studied case of room temperature gold there are significant modern corrections; e.g., $e_1(E = 1.5\,{\rm eV}) = -25.2$ in [18] and -29

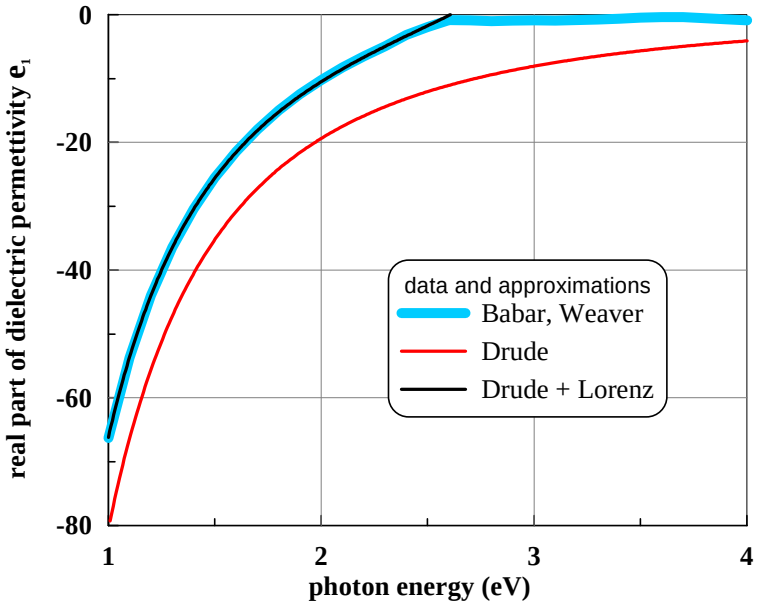

Figure D2. figure 2. Real part of dielectric permittivity with taking into account both Drude and Lorentz contributions (D.2) and (D.3) (the curve "Drude+Lorentz") in comparison with reference data from [18]. The curve "Drude" presents approximation (D.2) without the Lorentz term.

in [87]. Thus we can imagine how difficult the optical problem is in very shortly living poorly known 2T gold undergoing also solid–liquid phase transfer during 2T relaxation.

When interesting in the dielectric permittivity in a one-temperature situation, we can write in the first approximation as real and imaginary parts of the dielectric permittivity both for Drude and Lorenez contributions:

$$e_{1D} = 1 - \frac{\omega_{\rm pl}^2}{\omega^2 + \nu^2}, \quad \omega_{\rm pl}^2 = \frac{4\pi\, n_a e^2}{m_e}\, k_{\rm Zm}\, x\, Z(T_e), \tag{D.2}$$

$$e_{1L} = \frac{\Omega^2}{\omega_d^2 - \omega^2}, \tag{D.3}$$

$$e_{2D} = \frac{\omega_{\rm pl}^2}{\omega^2 + \nu^2}\,\frac{\nu}{\omega}, \quad e_{2L} = 0. \tag{D.4}$$

Here $\omega_{\rm pl}$ is a plasma frequency, e, m_e are electron charge and mass in vacuum. Laser frequency is $\omega = 3.04 \times 10^{15}$ rad/s for the light wavelength 620 nm and photon energy 2 eV. ν is electron collision frequency, $n_a = 5.9{\times}10^{22}$ cm^{-3} is concentration of atoms in normal conditions, $x = \rho/\rho_0$ is a compression factor ($\rho_0 = 19.5$ g/cm^3 is a density at zero temperature and pressure). $k_{\rm Zm}$ is a parameter defining ratio of effective charge Z per atom to effective electron mass. In room temperature gold an influence of collision frequency ν on the value of e_1 is weak because frequency $\nu = (0.04\text{–}0.1) \times 10^{15}$ is small relative to optical frequencies.

We use three points E_1, E_2, E_3 from the reference data [18] for $e_1(E)$ to find the set of the three parameters $k_{\rm Zm}$, Ω, and ω_d defining the curve "Drude+Lorentz" in figure D2, see equations (D.2) and (D.3). The particular curve "Drude+Lorentz" in figure D2 corresponds to the points $E_1 = 1.2$, $E_2 = 1.55$, $E_3 = 2.3$ eV located around the interval in figure D1 between the first and second harmonics. For these points the set is $k_{\rm Zm} = 0.884$, $\Omega = 11.5 \times 10^{15}$ s^{-1} (or 7.5 eV), and $\omega_d = 3.56$ eV. These values are stable. If we vary the energy values E_1, E_2, E_3 around

the horizontal interval in figure D1 then the parameters vary in the ranges $k_{\rm Zm} = 0.88$–0.89, $\Omega = 7$–7.5 eV, and $\omega_d = 3.3$–3.6 eV. Data presented in figure D2 show the adequite desription of permittivity as a sum of Drude and Lorentz contributions.

Appendix D.2. Two-temperature case

We are interesting in dielectic permittivity in two-temperature state. Again presenting permittivity as a sum of Drude and Lorentz parts, we have for the Drude permittivity:

$$e_{\rm 1D} = 1 - \frac{\omega_p^2(x)}{\omega^2 + \nu^2(x, T_e, T_i)}, \quad e_{\rm 2D} = \frac{\omega_p^2(x)}{\omega^2 + \nu^2(x, T_e, T_i)} \frac{\nu(x, T_e, T_i)}{\omega}. \tag{D.5}$$

In (D.5)

$$\omega_p = \sqrt{\frac{4\pi Z n_r e^2}{m_{\rm ef}} \frac{x}{x_r}}$$

is a plasma frequency with n_r to be a concentration of atoms at room conditions with Z conduction electrons per atom, effective mass of conduction electrons $m_{\rm ef} = 0.6 m_e$. In addition $x = \rho/\rho_0$ is the ratio of density to the density at zero temperature and pressure (19.5 g/cm^3), $x_r = 19.3/19.5$. Now electron collision frequency ν is a function of compression x and electron and ion temperatures T_e, T_i. It can be presented as a sum of collision frequencies of conduction electrons with ions $\nu_{\rm si}$ and d-electrons $\nu_{\rm sd}$: $\nu = \nu_{\rm si} + \nu_{\rm sd}$. These frequencies are calculated as in our works [85, 86] In solid state electron mean free path because of the phonon scattering following [85, 86]

$$\lambda_{\rm si} \propto \frac{\theta^2(x)}{n T_i} \propto \frac{\theta^2(x)}{x T_i},$$

where n is the concentration of atoms, $\theta(x)$ is the Debye temperature [85, 86]. To calculate dependence of Debye temperature on the density we approximate a cold pressure curve by the expression

$$p(x) = A n_0 x \left(x^a - x^b\right)$$

with $a = 1.82477$, $b = 1.75469$. Then [85, 86]

$$\theta(x) \propto x^{1/3} \sqrt{y(x)},$$

with a function

$$y(x) = \frac{(a+1) x^{2a+1}}{(b+1) + (a-b) x^{a+1}}.$$

Then we obtan the electron mean free path

$$\lambda_{\rm si} \propto \frac{y(x)}{x^{1/3} T_i}$$

and the electron-phonon collision frequency

$$\nu_{\rm si}(x, T_i) = \frac{v_F}{\lambda_{\rm si}} \propto \frac{x^{2/3} T_i}{y(x)}.$$

Electron-phonon collision frequency at initial room conditions $\nu_{\rm si}(x_r, T_r)$ can be found by using the well known resistivity of gold at room conditions $\rho_r = 22.1$ nOhm m from the Drude expression for the static resistivity

$$\nu_{\rm si}(x_r, T_r) = \frac{n_r e^2 \rho_r}{m_s}.$$

Then the electron-phonon collision frequency in solid state is obtained as

$$\nu_{\rm si}(x,T_i)=\nu_{\rm si}(x_r,T_r)\left(\frac{x}{x_r}\right)^{2/3}\frac{y(x_r)}{y(x)}\frac{T_i}{293}$$

with T_i measured in K. In liquid state with the use of the experimental value of resistivity $r_l(T_i)$ and compression on the binodal $x_l(T_i)$, we write frequency of electron-ion collisions as

$$\nu_{\rm si}(x,T_i)=\sqrt{\frac{2\varepsilon_F}{m_s}}n_a^{1/3}x^{-2/3}r_l(T_i)x_l(T_i).$$

Here $\varepsilon_F=9.2$ eV is the Fermi energy at room conditions. Dimensionless functions $r_l(T)$ and $x_l(T)$ when the temperature T is taken in kK are

$$r_l(T)=\left(119.8+142.8T\frac{15.337}{14+T}\right)/3254,$$

$$x_l(T)=0.937715-0.0378639T+0.00171949T^2-0.000594146T^3.$$

Depending upon the electron temperature and density effective frequency of collisions of s-electron with d-electrons is calculated as in the work [84]. It is obtained as $\nu_{\rm sd}=C_v\bar{v}^2/(3\kappa_s)$, Where C_v is a heat capacity of s-electrons per unit volume and $\bar{v}$ is a mean squared s-electro velocity. In figure D3 this effective frequency is shown for the calculation of the thermal conductivity κ_s with the help of two approaches. In the first one the Onzager coefficients are used to calculate the thermal conductivity as

$$\kappa_s=\frac{1}{T_e}\left(I_2-\frac{I_1^2}{I_0}\right) \tag{D.6}$$

with

$$I_0=\frac{1}{3(\pi m_s)^2\hbar^3}\int_0^\infty p^4\left(-\frac{\partial f}{\partial\varepsilon}\right)\frac{dp}{\nu_s(p)},$$
$$I_1=\frac{1}{3(\pi m_s)^2\hbar^3}\int_0^\infty p^4\left(-\frac{\partial f}{\partial\varepsilon}\right)(\varepsilon-\mu)\frac{dp}{\nu_s(p)},$$
$$I_2=\frac{1}{3(\pi m_s)^2\hbar^3}\int_0^\infty p^4\left(-\frac{\partial f}{\partial\varepsilon}\right)(\varepsilon-\mu)^2\frac{dp}{\nu_s(p)}.$$

In these expressions μ is the electron chemical potential and

$$-\frac{\partial f}{\partial\varepsilon}=\frac{\exp\left(\frac{\varepsilon-\mu}{k_BT_e}\right)}{\left(\exp\left(\frac{\varepsilon-\mu}{k_BT_e}\right)+1\right)^2}\frac{1}{k_BT_e}.$$

In the second approach the thermal conductivity is calculated as

$$\kappa_s=\frac{k_B}{3(\pi m_s)^2\hbar^3}\int_0^\infty p^4\left(\frac{\partial f}{\partial(k_BT_e)}\right)(\varepsilon-\mu)\frac{dp}{\nu_s(p)} \tag{D.7}$$

with

$$\frac{\partial f}{\partial(k_BT_e)}=\left(-\frac{\partial f}{\partial\varepsilon}\right)\left(\frac{{\rm d}\mu}{{\rm d}(k_BT_e)}+\frac{\varepsilon-\mu}{k_BT_e}\right).$$

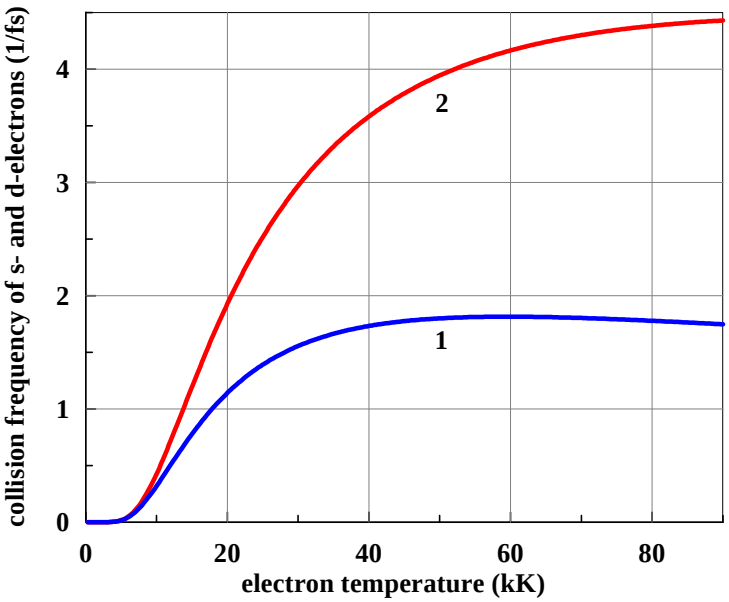

Figure D3. Effective frequency of collisions of s-electrons with d-electrons in dependence on the electron temperature at normal density. 1-approach (D.7) for the thermal conductivity; 2-Onzager coefficients approach (D.6)

In both cases the frequency of collisions of s-electron with a momentum p with d-electrons $\nu_s(p)$ are calculated as in [84].

The number of conduction electrons per atom depends upon the density and electron temperature. At small volume change it can be considered as a function of only T_e. We choose this value to be

$$Z(T_e) = 1 + \frac{3-1}{6 \times 11605 - 293}(T_e - 293). \tag{D.8}$$

Charge $Z(T_e)$ (D.8) increases as electron temperature T_e increases, see references [13] and [36]. This is consequence of a widening of Fermi distribution function and transition of d-electrons into the conductivity sp-band. In our theoretical calculation of dielectric permittivity we must take into account solid–liquid phase transition under the laser action. In the solid state we can find room Lorentz contributions to the permittivity from the known values of permittivities $e^s_{10} = -10.25$ and $e^s_{20} = 0.87$ at room conditions and room Drude permittivities e^0_{D1}, e^0_{D2}: $e^{s0}_{1L} = e^s_{10} - e^0_{1D}$, $e^{s0}_{2L} = e^s_{20} - e^0_{2D}$. We suppose that Lorentz contribution to the permittivity depends only the density: $e^s_{1L} = e^{s0}_{1L}x$, $e^s_{2L} = e^{s0}_{2L}x$. Then real and imaginary parts of dielectric permittivity, depending on the density, electron and ion temperature, can be written as

$$e^s_1(x, T_e, T_i) = e_{1D}(x, T_e, T_i) + e^{s0}_{1L}x,$$
$$e^s_2(x, T_e, T_i) = e_{2D}(x, T_e, T_i) + e^{s0}_{2L}x.$$

Data for the liquid phase are important because they help to understand experiments with ultrashort lasers acting on gold. Indeed, in our range of absorbed fluences gold target melts after laser action. Therefore dielectric function has to change to the liquid case after the stage of a 2T relaxation. Again starting with the known values of real and imaginary parts of permittivity in a liquid state at melting temperature T_m=1337 K, which are equal to $e^l_{10} = -10$ and $e^l_{20} = 0.6$,

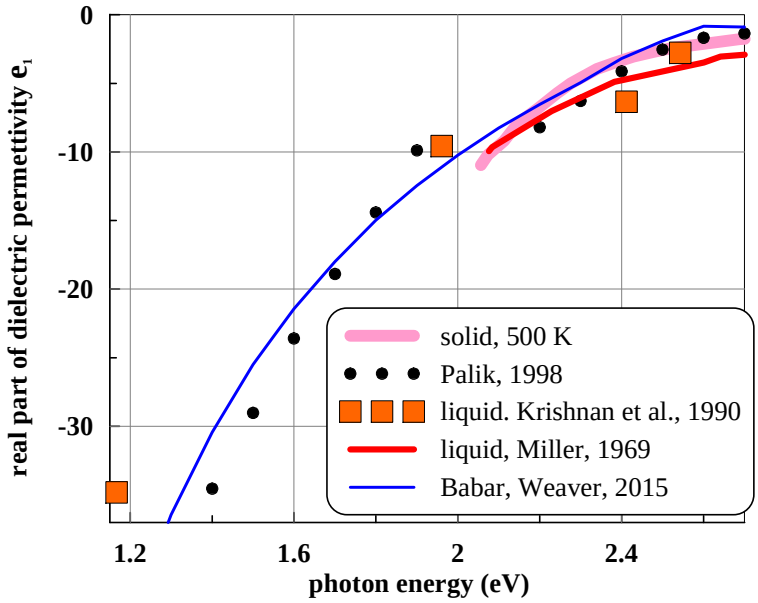

Figure D4. Influence of heating and melting on $e_1(E)$. The curves "Palik" [87] and "Babar, Weaver" [18] relate to room temperature. The curves "Miller" [24] and "Krishnan" [25] correspond to liquid. Solid heated to 500 K is also shown. These data are taken from [24].

we can present dielectric permittivity of a liquid in the form

$$e_1^l(x,T_e,T_i) = e_{1D}(x,T_e,T_i) + e_{1L}^{l0}x,$$
$$e_2^l(x,T_e,T_i) = e_{2D}(x,T_e,T_i) + e_{2L}^{l0}x.$$

Here $e_{1L}^{l0} = e_{10}^l - e_{1D}^0$ and $e_{2L}^{l0} = e_{20}^l - e_{2D}^0$ are Lorentz contributions to real and imaginary parts of permittivity of a liquid at the melting point. Heating and/or melting slightly changes e_1 (the real part of e) and significantly increases e_2 because there is an order of magnitude increase in collision rate $\nu \approx \nu_{ei}$ from $\approx 0.04 \times 10^{15}$ to $\approx 0.5 \times 10^{15}$ s^{-1} thanks to heating from room temperature and melting. In one-temperature (1T) molten gold the electron-electron $\nu_{\rm ss}$ and $\nu_{\rm sd}$ collision frequencies are still (as in 1T solid for T small in comparison with Fermi temperature) small relative to the electron-ion collision frequency $\nu_{\rm ei}$. Literature data about e_1 are collected in figure D4.

Pump-probe measurements done at the probe wavelength 620 nm (second harmonics of Ti:forsterite) are shown in figure D5. Absorbed fluence $F_{\rm abs} \approx 1.2F_a$ is not far from ablation threshold F_a.

Initial values (prior to pump action) of reflectivity and phase are $R(t=-\infty) = 0.953$ and $\varphi(t=-\infty) = 29.8$ nm. They are calculated for the normal incidence wave 620 nm from the reference values $e_1 = -10.25$ and $e_2 = 0.87$ corresponding to room temperature, see figure D1 [18]. Reference values for liquid are $e_1 = -10$ and $e_2 = 6$ [24], see figure D4. Corresponding reflectivity and phase are $R(t=-\infty) = 0.75$ and $\varphi(t=-\infty) = 27.3$ nm. They are shown in figure D6. The wave reflected from room temperature gold is marked by 1. While the wave reflected from liquid gold is 2; its reflection coefficient and phase (if measured from the direction π) are smaller than for wave 1. Probing and 2T hydrodynamic simulation indicate that the enhanced values of phase difference and absorption in figure D5 correspond to 2T stage. During the 2T stage gold transfers from solid to liquid phase. Corresponding trajectory is shown in figure D6. The trajectory starts from the point 1 at $t = -\infty$. During an ultrashort pump the

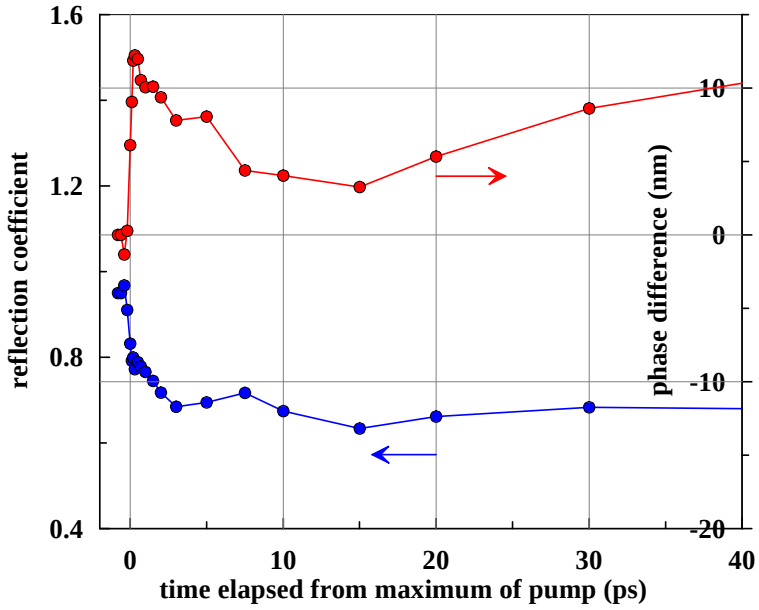

Figure D5. Results of probing at normal incidence by 620 nm probe wave. Phase shift $\Delta\phi(t) = -[\phi(t = -\infty) - \phi(t)]$ (red curve) and reflectivity $R(t)$ (blue curve) are presented. Fluence is $F_{\text{abs}} \approx 1.2F_a$, F_a is ablation threshold.

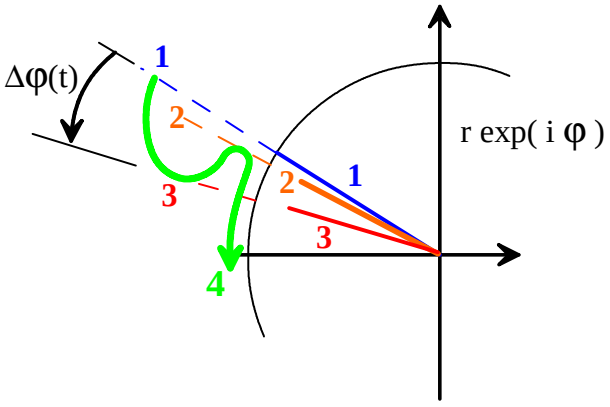

Figure D6. Plane of reflected wave with amplitude r and phase φ. The largest amplitude (line 1) corresponds to reflection from room temperature Au. Amplitudes for reflection from 1T liquid gold (line 2) and 2T gold (line 3) are approximately equal each other- no increase in absorption at the 2T stage relative subsequent 1T stage: see figure D5. But their phases are different—the phase (line 3) is significantly less than phases of the lines 1 and 2 enhanced metalicity of a 2T state.

trajectory passes from the point 1 to the 2T state (point 3). Gold melts during 2T stage. After 2T relaxation a surface of reflection changes its state to 1T liquid (point 2). Therefore the part 1–3–2 of the trajectory covers the 2T stage.

The expansion velocities are rather small ~ 0.1 km/s for moderate values of absorbed energy $F_{\text{abs}} \sim 100$ mJ/cm^2. Thus the spatial shift ~ 1 nm during 2T stage is small relative to amplitude of an angular phase driven by changes in optical properties. But later in time temperature of a reflection surface decreases slowly (on ~ 100 ps time scale for bulk targets) while the surface

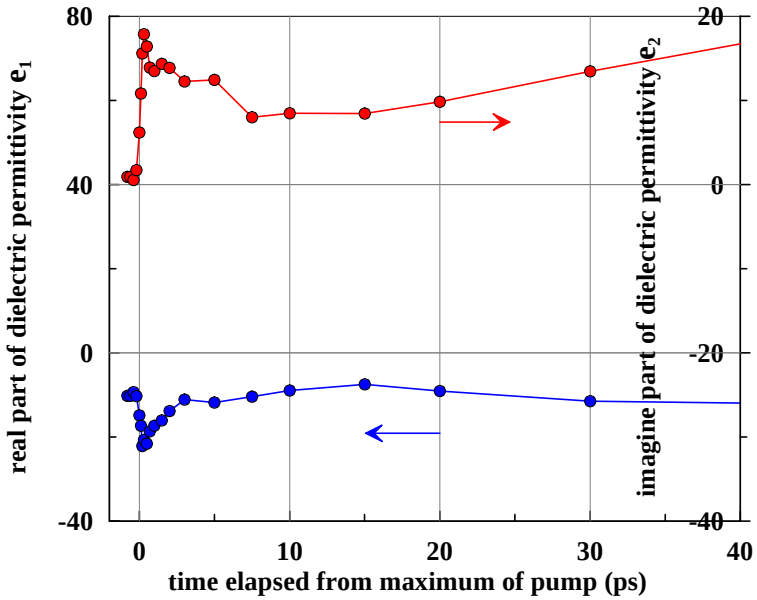

Figure D7. Creation of highly dissipative state (increase of e_2) with enhanced metallicity (increase of $|e_1|$) by sharp femtosecond pump laser action. The temporal interval with increased values of e_2 and $|e_1|$ clearly restricts duration of the 2T stage. Thus opening the way for estimate of electron-ion coupling parameter.

moves out (if $F_{\rm abs}$ is above the ablation threshold) increasing the angle $\Delta\varphi(t)$ in figure D6. The whole trajectory is 1–3–2–4, see figure D6. It is not possible to use the functions $R(t)$, $\Delta\varphi(t)$ to obtain information about dielectric permittivity $e(t)$ at the 2–4 part of the trajectory. But the current position $h(t) \approx \Delta\varphi(t) - \Delta\varphi_{132}$ of the surface of reflection may be found from the angle $\Delta\varphi(t)$, here $\Delta\varphi_{132}$ is the phase difference accumulated to the end of the 2T stage. Let us use values $R(t)$, $\Delta\varphi(t)$ from figure D5 for calculation of dielectric permittivity $e(t) = e_1 + \mathrm{i}e_2$ at the reflection surface. First we have to obtain the full current phase

$$\varphi(t) = \varphi(t = -\infty) - \Delta\varphi(t) = 29.8 - \Delta\varphi(t);$$

here we define phase in nanometers. After that using experimental R, φ we find permittivity e_1, e_2. The first step is: $a = (1 + R)/(1 - R)$, $\tau = \tan(4\pi\varphi/\lambda)$, $\lambda = 620$ nm. At the second step we define refractive index $N = n + \mathrm{i}k$, $n = A/B$,

$$A = a(1 + \tau^2) + \sqrt{(a^2 - 1)(1 + \tau^2)}, \quad B = 1 + a^2\tau^2, \quad k = \tau(a\, n - 1).$$

Then permittivity epsilon is $e = N^2 = e1 + \mathrm{i}e2$, $e1 = n^2 - k^2$, $e2 = 2nk$. Result of this transform $R, \varphi \to e_1, e_2$ from figure D5 is presented in figure D7.

In highly metallic states a dielectric permittivity $e = e_1 + \mathrm{i}e_2$ is $e_1 < 0$, $|e_1| \gg 1$. Then the real and imagine parts of refraction index $N = n + \mathrm{i}k$ are

$$n = 2^{-1/2}\sqrt{\sqrt{e_1^2 + e_2^2} - |e_1|} \approx \frac{e_2}{2\sqrt{|e_1|}} \ll 1,$$

$$k = 2^{-1/2}\sqrt{\sqrt{e_1^2 + e_2^2} + |e_1|} \approx \sqrt{|e_1|} \gg 1 \gg n.$$

The normal incidence reflection and phase are

$$R = \frac{(1-n)^2 + k^2}{(1+n)^2 + k^2} \approx 1 - \frac{4n}{k^2+1} \approx 1 - \frac{2e_2}{|e_1|^{3/2}},$$
$$\varphi = \arctan \frac{2\,k}{n^2 + k^2 - 1} \approx \arctan \frac{2}{k}.$$

Thus for large metallicity we have large $|e_1|$, large k, and small angle φ. Checking figures D5 and D7 we see that, indeed, at the 2T stage there are enhanced $|e_1|$ and smaller φ—the angle elapsed from the left horizontal semiaxis in figure D6 is significantly smaller at the 2T stage (line 3) relative to 1T solid (line 1) or 1T liquid (line 2).

References

[1] Anisimov S I, Kapeliovich B L and Perel'man T L 1974 *Sov. Phys. JETP* **39** 375–377
[2] Agranat M B, Ashitkov S I, Ovchinnikov A V, Sitnikov D S, Yurkevich A A, Chefonov O V, Perel'man L T, Anisimov S I and Fortov V E 2015 *JETP Lett.* **101** 598–602
[3] Zhakhovskii V V, Nishihara K, Anisimov S I and Inogamov N A 2000 *JETP Lett.* **71** 167–172
[4] Ivanov D S and Zhigilei L V 2003 *Phys. Rev.* B **68** 064114
[5] Anisimov S I, Zhakhovskii V V, Inogamov N A, Nishihara K, Oparin A M and Petrov Yu V 2003 *JETP Lett.* **77** 606–610
[6] Inogamov N A, Zhakhovsky V V, Khokhlov V A, Ashitkov S I, Emirov Yu N, Khichshenko K V, Faenov A Ya, Pikuz T A, Ishino M, Kando M, Hasegawa N, Nishikino M, Komarov P S, Demaske B J, Agranat M B, Anisimov S I, Kawachi T and Oleynik I I 2014 *J. Phys.: Conf. Ser.* **510** 012041
[7] Ashitkov S I, Komarov P S, Ovchinnikov A V, Struleva E V, Zhakhovskii V V, Inogamov N A and Agranat M B 2014 *Quantum Electron.* **44** 535–539
[8] Wu C, Christensen M S, Savolainen J M, Balling P and Zhigilei L V 2015 *Phys. Rev.* B **91** 035413
[9] Ashitkov S, Romashevskii S, Komarov P, Burmistrov A, Zhakhovskii V, Inogamov N and Agranat M 2015 *Quantum Electron.* **45** 547–550
[10] Inogamov N A, Zhakhovsky V V, Ashitkov S I, Emirov Yu N, Faenov A Ya, Petrov Yu V, Khokhlov V A, M I, Demaske B J, Tanaka M, Hasegawa N, Nishikino M, Tamotsu S, Pikuz T A, Skobelev I Y, Ohba T, Kaihori T, Ochi Y, Imazono T, Fukuda Y, Kando M, Kato Y, Kawachi T, Anisimov S I, Agranat M B, Oleynik I I and Fortov V 2015 *Eng. Failure Anal.* **47** 328–337
[11] Inogamov N A, Zhakhovsky V V, Hasegawa N, Nishikino M, Yamagiwa M, Ishino M, Agranat M B, Ashitkov S I, Faenov A Ya, Khokhlov V A, Ilnitsky D K, Pikuz T A, Takayoshi S, Tomita T and Kawachi T 2015 *Appl. Phys.* B **119** 413–419
[12] Inogamov N A and Zhakhovsky V V 2016 *J. Phys.: Conf. Ser.* **681** 012001
[13] Inogamov N A, Zhakhovskii V V, Ashitkov S I, Khokhlov V A, Petrov Yu V, Komarov P S, Agranat M B, Anisimov S I and Nishihara K 2009 *Appl. Surf. Sci.* **255** 9712–9716
[14] Ashitkov S I, Komarov P S, Struleva E V, Yurkevich A A and Agranat M B 2015 *High Temp.* **53** 887–890
[15] Demaske B J, Zhakhovsky V V, Inogamov N A and Oleynik I I 2010 *Phys. Rev.* B **82** 064113
[16] Chan W L, Averback R S and Cahill D G 2009 *Appl. Phys.* A **97** 287–294
[17] Bezhanov S G, Kanavin A P and Uryupin S A 2011 *Quantum Electron.* **41** 447–452
[18] Babar S and Weaver J 2015 *Appl. Opt.* **54** 477–481
[19] Khishchenko K V 2008 *J. Phys.: Conf. Ser.* **98** 032023
[20] Khishchenko K V 2008 *J. Phys.: Conf. Ser.* **121** 022025
[21] Inogamov N A, Petrov Yu V, Zhakhovsky V V, Khokhlov V A, Demaske B J, Ashitkov S I, Khishchenko K V, Migdal K P, Agranat M B, Anisimov S I, Fortov V E and Oleynik I I 2012 *AIP Conf. Proc.* **1464** 593–608
[22] Migdal K P, Il'nitsky D K, Petrov Yu V and Inogamov N A 2015 *J. Phys.: Conf. Ser.* **653** 012086
[23] Petrov Yu V, Migdal K P, Inogamov N A and Zhakhovsky V V 2015 *Appl. Phys.* B **119** 401–411
[24] Miller J C 1969 *Philos. Mag.* **20** 1115–1132
[25] Krishnan S, Hansen G, Hauge R and Margrave J 1990 *High Temp. Sci.* **29** 17
[26] Schmid M, Zehnder S, Schwaller P, Neuenschwander B, Held M, Hunziker U and Zuercher J 2012 *Advanced Laser Technologies, ALT-12* **1**
[27] Hohlfeld J, Wellershoff S S, Guedde J, Conrad U, Jaehnke V and Matthias E 2000 *Chem. Phys.* **251** 237–258
[28] Fatti N D, Voisin C, Achermann M, Tzortzakis S, Christofilos D and Vallee F 2000 *Phys. Rev.* B **61** 16956–16966

[29] Widmann K, Ao T, Foord M E, Price D F, Ellis A D, Springer P T and Ng A 2004 *Phys. Rev. Lett.* **92** 125002
[30] Ao T, Ping Y, Widmann K, Price D F, Lee E, Tam H, Springer P T and Ng A 2006 *Phys. Rev. Lett.* **96** 055001
[31] Ping Y, Hanson D, Koslow I, Ogitsu T, Prendergast D, Schwegler E, Collins G and Ng A 2006 *Phys. Rev. Lett.* **96** 255003
[32] Inogamov N A, Zhakhovskii V V, Ashitkov S I, Petrov Yu V, Agranat M B, Anisimov S I, Nishihara K and Fortov V E 2008 *J. Exp. Theor. Phys.* **107** 1–19
[33] Ping Y, Hanson D, Koslow I, Ogitsu T, Prendergast D, Schwegler E, Collins G and Ng A 2008 *Phys. Plasmas* **15** 056303
[34] Chen Z, Sametoglu V, Tsui Y Y, Ao T and Ng A 2012 *Phys. Rev. Lett.* **108** 165001
[35] Chen Z, Holst B, Kirkwood S E, Sametoglu V, Reid M, Tsui Y Y, Recoules V and Ng A 2013 *Phys. Rev. Lett.* **110** 135001
[36] Fourment C, Deneuville F, Descamps D, Dorchies F, Petit S and Peyrusse O 2014 *Phys. Rev.* B **89** 161110(R)
[37] Cho B I, Engelhorn K, Correa A A, Ogitsu T, Weber C P, Lee H J, Feng J, Ni P A, Ping Y, Nelson A J, Prendergast D, Lee R W, Falcone R W and Heimann P A 2011 *Phys. Rev. Lett.* **106** 167601
[38] Migdal K P, Petrov Yu V, Il'nitsky D K, Zhakhovsky V V, Inogamov N A, Khishchenko K V, Knyazev D V and Levashov P R 2016 *Appl. Phys.* A **122** 408
[39] Sokolowski-Tinten K, Blome C, Blums J, Cavalleri A, Dietrich C, Tarasevitch A, Uschmann I, Foerster E, Kammler M, von Hoegen M H and von der Linde D 2003 *Nature* **422** 287–289
[40] Johnson S L, Beaud P, Milne C J, Krasniqi F S, Zijlstra E S, Garcia M E, Kaiser M, Grolimund D, Abela R and Ingold G 2008 *Phys. Rev. Lett.* **100** 155501
[41] Harb M, Ernstorfer R, Hebeisen C T, Sciaini G, Peng W, Dartigalongue T, Eriksson M A, Lagally M G, Kruglik S G and Miller R J D 2008 *Phys. Rev. Lett.* **100** 155504
[42] Agranat M B, Andreev N E, Ashitkov S I, Veisman M E, Levashov P R, Ovchinnikov A V, Sitnikov D S, Fortov V E and Khishchenko K V 2007 *JETP Lett.* **85** 271–276
[43] Agranat M B, Ashitkov S I, Ivanov A A, Konyashchenko A V, Ovchinnikov A V and Fortov V E 2004 *Quantum Electron.* **34** 506–508
[44] Temnov V V, Sokolovski-Tinten K, Zhou P and von der Linde D 2006 *J. Opt. Soc. Am.* B **23** 19554
[45] Liu J 1982 *Opt. Lett.* **7** 196–198
[46] Rakic A D, Djurisic A B, Elazar J M and Majewski M L 1998 *Appl. Opt.* **37** 5271–5283
[47] Kanel G I, Savinykh A S, Garkushin G V and Razorenov S V 2015 *JETP Lett.* **102** 548
[48] Kanel' G I, Fortov V E and Razorenov S V 2007 *Phys. Usp.* **50** 771–791
[49] Povarnitsyn M E, Itina T E, Khishchenko K V and Levashov P R 2007 *Appl. Surf. Sci.* **253** 6343–6346
[50] Povarnitsyn M E, Itina T E, Sentis M, Khishchenko K V and Levashov P R 2007 *Phys. Rev.* B **75** 235414
[51] Colombier J P, Combis P, Audouard E and Stoia R 2008 *Phys. Rev.* E **77** 036409
[52] Povarnitsyn M E, Itina T E, Khishchenko K V and Levashov P R 2009 *Phys. Rev. Lett.* **103** 195002
[53] Inogamov N A, Zhakhovsky V V, Ashitkov S I, Khokhlov V A, Shepelev V V, Komarov P S, Ovchinnikov A V, Sitnikov D S, Petrov Yu V, Agranat M B, Anisimov S I and Fortov V E 2011 *Contrib. Plasma Phys.* **51** 367–374
[54] Loboda P A, Smirnov N A, Shadrin A A and Karlykhanov N G 2011 *High Energy Density Phys.* **7** 361–370
[55] Fisher D, Fraenkel M, Henis Z, Moshe E and Eliezer S 2001 *Phys. Rev.* E **65** 016409
[56] Tkachenko S I, Khishchenko K V, Vorob'ev V S, Levashov P R, Lomonosov I V and Fortov V E 2001 *High. Temp.* **39** 674–687
[57] Khishchenko K V, Tkachenko S I, Levashov P R, Lomonosov I V and Vorob'ev V S 2002 *Int. J. Thermophys.* **23** 1359
[58] Oreshkin V I, Baksht R B, Ratakhin N A, Shishlov A V, Khishchenko K V, Levashov P R and Beilis I I 2004 *Phys. Plasmas* **11** 4771
[59] Levashov P R and Khishchenko K V 2007 *AIP Conf. Proc.* **955** 59–62
[60] Demaske B J, Zhakhovsky V V, Inogamov N and Oleynik I I 2013 *Phys. Rev.* B **87** 054109
[61] Inogamov N A, Zhakhovsky V V, Petrov Yu V, Khokhlov V A, Ashitkov S I, Khishchenko K V, Migdal K P, Initsky D K, Emirov Yu N, Shepelev V V, Oleynik I I, Agranat M B, Andriyash A V, Anisimov S I and Fortov V E 2013 *Contrib. Plasma Phys.* **53** 796–810
[62] Inogamov N A, Khokhlov V A, Petrov Yu V, Anisimov S I, Zhakhovsky V V, Demaske B J, Oleynik I I, White C T, Ashitkov S I, Khishchenko K V, Agranat M B and Fortov V E 2012 *AIP Conf. Proc.* **1426** 909–912
[63] Inogamov N A, Anisimov S I and Retfeld B 1999 *J. Exp. Theor. Phys.* **88** 1143–1150
[64] Inogamov N A, Petrov Yu V, Anisimov S I, Oparin A M, Shaposhnikov N V, von der Linde D and ter Vehn J M 1999 *JETP Lett.* **69** 310–316

[65] Anisimov S I, Inogamov N A, Oparin A M, Rethfeld B, Yabe T, Ogawa M and Fortov V E 1999 *Appl. Phys.* A **69** 617–620
[66] Chimier B and Tikhonchuk V T 2009 *Phys. Rev.* B **79** 184107
[67] Petrov Yu, Migdal K P, Inogamov N A and Zhakhovsky V V 2015 *Appl. Phys.* B **119** 401–411
[68] Agranat M B, Anisimov S I, Ashitkov S I, Zhakhovskii V V, Inogamov N A, Komarov P S, Ovchinnikov A V, Fortov V E, Khokhlov V A and Shepelev V V 2010 *JETP Lett.* **91** 471–477
[69] Ashitkov S I, Agranat M B, Kanel G I, Komarov P S and Fortov V E 2010 *JETP Lett.* **92** 516–520
[70] Zhakhovskii V V and Inogamov N A 2010 *JETP Lett.* **92** 521–526
[71] Inogamov N A, Zhakhovsky V V, Khokhlov V A and Shepelev V V 2011 *JETP Lett.* **93** 226–232
[72] Zhakhovsky V V, Inogamov N A, Demaske B J, Oleynik I I and White C T 2014 *J. Phys.: Conf. Ser.* **500** 172007
[73] Perriot R, Zhakhovsky V V, Inogamov N A and Oleynik I I 2014 *J. Phys. Conf. Ser.* **500** 172008
[74] Ashitkov S I, Komarov P S, Struleva E V, Agranat M B and Kanel G I 2015 *JETP Lett.* **101** 276–281
[75] Ilnitsky D K, Khokhlov V A, Inogamov N A, Zhakhovsky V V, Petrov Yu V, Khishchenko K V, Migdal K P and Anisimov S I 2014 *J. Phys.: Conf. Ser.* **500** 032021
[76] Inogamov N A, Zhakhovsky V V, Khokhlov V A, Demaske B J, Khishchenko K V and Oleynik I I 2014 *J. Phys.: Conf. Ser.* **500** 192023
[77] Volkov A N and Zhigilei L V 2007 *J. Phys.: Conf. Ser.* **59** 640–645
[78] Inogamov N A, Faenov A Ya, Khokhlov V A, Zhakhovskii V V, Petrov Yu V, Skobelev I Yu, Nishihara K, Kato Y, Tanaka M, Pikuz T A, Kishimoto M, Ishino M, Nishikino M, Fukuda Y, Bulanov S V, Kawachi T, Anisimov S I and Fortov V E 2009 *Contrib. Plasma Phys.* **49** 455–466
[79] Zhakhovskii V V, Inogamov N A, Petrov Yu V, Ashitkov S I and Nishihara K *Appl. Surf. Sci.* **255** 9592–9596
[80] Inogamov N A, Zhakhovskii V V and Khokhlov V A 2015 *J. Exp. Theor. Phys.* **120** 1548
[81] Ashitkov S I, Inogamov N A, Zhakhovsky V V, Emirov Yu N, Agranat M B, Oleinik I I, Anisimov S I and Fortov V E 2012 *JETP Lett.* **95** 176–181
[82] Inogamov N, Zhakhovsky V V, Ashitkov S I, Emirov Yu N, Faenov A Ya, Pikuz T A, Ishino M, Kando M, Hasegawa N, Nishikino M, Kawachi T, Agranat M B, Andriash A V, Kuratov S E and Oleynik I I 2014 *J. Phys.: Conf. Ser.* **500** 112070
[83] Lin Z, Zhigilei L V and Celli V 2008 *Phys. Rev.* B **77** 075133
[84] Petrov Yu V, Inogamov N A and Migdal K P 2013 *JETP Lett.* **97** 20–27
[85] Petrov Yu V, Inogamov N A, Anisimov S I, Migdal K P, Khokhlov V A and Khishchenko K V 2015 *J. Phys.: Conf. Ser.* **653** 012087
[86] Petrov Yu V, Inogamov N A and Migdal K P 2015 *Progress In Electromagnetics Research Symposium Proceedings* (PIERS Proceedings) pp 2431–2435
[87] Palik E D (ed) 1998 *Handbook of Optical Constants of Solids* (New York: Academic Press)